Level set methods for multilayer geological folding

Boon, Jonathan Andrew

Award date:
2007

Awarding institution:
University of Bath

Level Set Methods for Multilayer Geological Folding

submitted by

Jonathan Andrew Boon

for the degree of Doctor of Philosophy

of the

University of Bath

Department of Mechanical Engineering

May 2007

ProQuest LLC
789 East Eisenhower Parkway
P.O. Box 1346
Ann Arbor, MI 48106-1346

Abstract

The displacement of layered materials occurs when a compressive load is applied to materials in the layer parallel direction. A prime example is the multilayered folding of rocks, a process that occurs when geological systems are placed under tectonic compression. The geometry of these folds ranges from almost sinusoidal patterns to kinks and chevron folding. By considering fully elastic layers, it is shown that many of the geometrical phenomena are a natural result of the layers fitting together without forming voids.

By assuming that the interfaces between the layers are projected as a wave front from a central interface, the level set method is used to describe the geometry of the multilayer. The level set method encodes the geometrical information in a function $\phi(x, y, t)$, which is able to handle layers with singularities.

The geometrical description of the multilayer is coupled with a nonlinear pseudo-potential energy based model for parallel folding in the non-singular case to which we look for states which are stationary points. The energy function allows for bending energy, foundation energy and work done against friction and by applied load. These energy contributions are all expressed in terms of the level set function that is used to describe the geometry.

To replicate the phenomena of geological folding in order to test the model, a set of experiments were performed on a multilayer comprising sheets of paper embedded between sheets of rubberised foam. When the theoretical wavelengths and minimum axial load values are compared with those measured experimentally there is good agreement provided that the multilayer is sufficiently thick.

Based on the observations of the experiments and the comparisons with the

theory suggestions are made for future research.

Acknowledgements

I would like to begin by thanking my supervisors Professor Chris Budd and Professor Giles Hunt. I have benefited from having two experienced academics to point me in the right direction and to introduce me to the world of interdisciplinary research. Throughout my PhD it has always been a pleasure to work with them both.

I would also like to thank Dr. Ahmer Wadee for inviting me to Imperial College for a week in 2006, enabling me to conduct the experiments that are of great importance to my thesis, and appear in chapter 5.

Special thanks go to my fiancée Sarah Zohhadi for her encouragement throughout my PhD, and to all my family and friends for their continued support.

Finally, a big thanks to all those who I shared an office with during my PhD. In particular to Dr. Jenny Wright, Caroline Edwards, Philip Williams, Nikolaos Kontis and Dr. Wenli Liu.

This research was funded by the Engineering and Physical Sciences Research Council (EPSRC) and their support is gratefully acknowledged.

Contents

List of Figures

List of Tables

Nomenclature

Geometry

θ	Angle of layer with horizontal
κ	Layer curvature
R	Radius of curvature of a curve
R_i	Radius of layer i
w	Mode shape
$\mathcal{T}$	Radius of curvature when singularity first appears
a	Layer length
b	Breadth of layers
d	Layer depth (or thickness Δt)
L	Half wavelength
l	Arc length coordinate
s	Arc length parameter
Q	Amplitude of central interface
T	Total multilayer thickness

Level set notation

ϕ	Level set function
Δt	Time step (equal to layer thickness)
$\Gamma_{i\Delta t}$	Zero level set of layer i
Γ_0	Zero level set of layer 0 - the reference layer
$\mathbf{n}$	Normal to the interface
t	Normal distance from a reference layer
$\mathbf{v}$	Interface velocity
h	Spatial step
x	Horizontal coordinate
y	Vertical coordinate

Loads and Energies

P	Axial load
P^C	Critical (axial) load
P_{min}	Minimum axial load value
$\mathcal{E}$	Axial end shortening
P_L	Lateral load
q	Lateral load per unit length
Δ_L	Lateral displacement
V	Total potential energy
U_B	Bending energy
U_F	Foundation energy
U_μ	Work done against friction

Material Properties

E	Young's modulus of the layers

I	Second moment for area of an individual layer
μ	Coefficient of friction
k	Effective foundation stiffness
k_{fit}	Foundation stiffness
k_{layers}	In-line layer stiffness

Additional literature review notation

ϵ	Strain
σ	Stress
H	Hamiltonian
F	Flux function
M	Bending moment
$\mathcal{F}$	Numerical flux function
G	Shear modulus
τ	Shear stress
γ	Shear strain
η	Viscosity
Q_i	Set of generalised coordinates
Λ_j	Control parameters
χ	Friction indicator
g	Acceleration due to gravity
ν	Layer viscosity
ν_1	Matrix viscosity

Chapter 1

Introduction

1.1 Geological folding

Geological folding is a process that occurs in the upper regions of the Earth's crust. Fold formation in layers of rock is often accompanied by a drop in pressure in the surrounding medium, which can draw in large quantities of natural resources, such as minerals and hydrocarbons (Hunt et al., 1997). Understanding geological folds is important to mining companies to ease the extraction of these resources. Developing mathematical models of geological scenarios can assist with this understanding.

The formation of geological folds occurs over long time scales (typically in excess of 46,000 years (Budd and Peletier, 2000)) and at depths that are unobservable to humans. There are, therefore, many unknowns when formulating mathematical models and, as a result, a number of different approaches and assumptions have been used by geologists. Furthermore, with the continued development of new technologies, many of the older models are reviewed and updated with more modern techniques. It is not surprising then that structural geology and in particular geological folding have been active research areas for over a century and are still going strong in the present day.

In this thesis a mathematical model is developed, using modern numerical

methods, for the parallel folding of layered materials (see figure 1-1). The primary application of this work is to sedimentary rocks; however, there are also non-geological applications. The model could also be used to understand the mechanisms that govern the buckling of other layered materials. An example of this is the deformation of carbon fibre composites in aircraft wings.

We finish this short introduction with a figure that motivates much of the following work. Figure 1-1 shows an example of geological folding with a layer thickness of around $10 - 25\,\text{cm}$. We shall see from the definitions given in section 2.2 that this is an example of a parallel fold. It is interesting to see how the geometry can change from one layer to another and the possible effect that this had on the mechanics when the multilayer buckled.

Figure 1-1: Parallel folding of rocks near Bude, Cornwall, showing a singularity forming as we move from bottom to top in the figure.

1.2 Thesis outline

1.2.1 Brief overview of work

It is well known that the geometry of parallel folds changes from layer to layer. However, this fact has tended to be overlooked in previous models. The approach

taken in this thesis has been to use the level set method to describe the geometry of every individual layer of a multilayer. An accurate description of the geometry has led to a greater understanding of the mechanics of the system and the role that the bending energy has in restabilising a fold. The model is compared to a set of experiments and they are shown to be in good agreement. What is more, the observations of these experiments have resulted in new findings and understanding of multilayer folding.

We now give the layout of what is to appear in the remaining chapters.

1.2.2 Technical background

After the thesis outline, the remainder of the present chapter will introduce a number of geological, engineering and mathematical ideas that provide the necessary background in the context of the main body of work.

1.2.3 Literature review

Chapter 2 provides a critical survey of the literature that is relevant to the current work. The chapter can be split naturally into two sections, reflecting the previously separate subject areas of structural geology and front propagation methods. The history of the study of geological folding begins with experiments based on field observations of geological outcrops. In the early days, modelling was limited to simple elastic beam theory. In the 1960's and 1970's Biot wrote a series of prominent papers arguing that rock deformation is governed by viscosity, a belief that is still held by some researchers to the present day. However, others chose to stick with the elastic assumptions and evidence is provided for this assertion. Having accepted the value of elastic models, structural engineers then applied their advanced, energy based, buckling techniques to model rock deformation.

There are two main techniques that are used to model a moving front. The standard approach is the Lagrangian method, whereby the front is discretised

into a set of marker particles. By moving each of these particles by a prescribed amount the new position of the front is calculated. These seemingly simple and accurate methods can become extremely complex if the topology of the front changes or if the path of one particle crosses the path of another. The second class of methods are the Eulerian techniques. In these methods, rather than moving particles with the front, the front passes through a fixed computational domain. Typically, the advantage of these methods is the natural way the difficulties associated with the Lagrangian approach are overcome, so that changes in topology and self-intersecting fronts are not a problem. A challenge with the Eulerian approach is to locate the front accurately, which is often only defined implicitly.

1.2.4 Model development

Chapters 3 and 4 are where much of the fundamental theory for the level set based multilayer folding model is developed. We begin by showing that singular behaviour arises naturally in the folding of multilayered materials. In parallel folds, singularities can form as the curvature increases in the regions on the inside of a fold. The increase in curvature results in a local increase in bending energy that is large enough to lock the fold up and to initiate so called *serial folding*. As a consequence extra care needs to be taken when modelling the geometry, including features such as singularities. For this reason, the level set method is used to propagate a reference layer in its normal direction, picking out the position of all the other layers together with any singularities that may appear as a result of the advection. Our geometrical model then provides all the information required to calculate the total potential energy of the system in terms of the single reference layer. The work presented in chapters 3 and 4 has been published in the paper Boon et al. (2007a).

1.2.5 Experiments

Chapter 5 provides the details of a series of 20 experiments that were conducted on layers of paper. These experiments were designed to model the geological process of rock folding, so that comparisons can be made with the numerical model of chapters 3 and 4. Details of the experimental procedure are given, followed by observations of the resulting output. As a consequence of the observations, we classify the experiments into three different folding categories. The differing behaviour of the multilayer in the three cases has implications as to how we understand geological serial folding.

1.2.6 Comparison of model with experiments

In chapter 6 the model developed in chapters 3 and 4 is compared with the experiments of chapter 5. First experimental parameters are estimated, as inputs for the model. Fold wavelengths are found using small deflection theory and are compared to wavelengths measured from photographs of the experiments, and in the majority of cases there is good agreement. The fully nonlinear level set based model is then used to find load against end shortening plots, which, given a certain amount of uncertainty in the model parameters are shown to have good agreement with experiment. The work presented in chapters 5 and 6 is being prepared for publication (Boon et al., 2007b).

1.2.7 Conclusion

Finally, chapter 7 concludes the thesis and the key findings, their implications and the limitations of the research are presented. In light of this information, recommendations are made for possible future work that could answer some of the questions that have arisen during the completion of this thesis.

1.3 Geological background

The aim of this section is to provide the geological background and terminology required to understand the remainder of this work. The history of how geological folding models have developed and their relative merits follows in chapter 2. Further explanations for much of the geological terminology can be found in Price and Cosgrove (1990).

1.3.1 Fold classification

The need to classify folds arose when it was noticed that some types of folds occurred more frequently in nature than others. The majority of these classifications are based on the fold in *profile section.*

Definition 1. *Fold profile*

The intersection of the folded surface on a plane normal to the fold axis is known as the fold profile. The geometrical features of a fold profile are shown in figure 1-2.

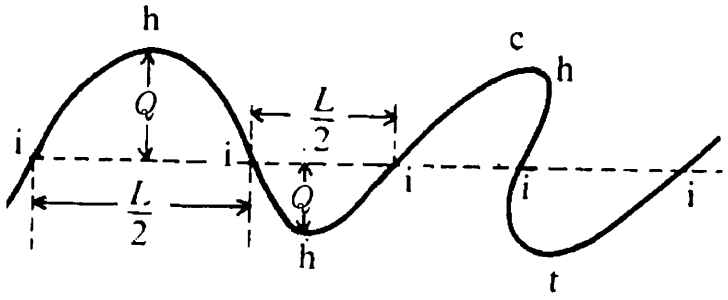

Figure 1-2: Terms used to describe the geometry of the profile of a fold: h and i are hinge and inflection points; c and t denote the crests and troughs of a fold and Q and L are the amplitude and wavelength of the fold. The dashed line is called the median surface. (After Price and Cosgrove (1990))

These features include *hinge* and *inflection* points, points of maximum and zero curvature respectively. Also shown are the *crests* and *troughs* which are the highest/lowest points of the fold. It is generally considered that two adjacent

inflection points mark the limits of the fold and because neighbouring folds often vary in length it is convenient to measure the *wavelength* as twice the distance between these points. However, as we shall see when we formulate the model in chapter 3, it is sometimes more convenient for us to define the wavelength simply as the arc length of a fold. The *amplitude* is the perpendicular distance between the median surface and fold hinge.

The most natural way of classifying the fold geometry is with the method of *dip isogens.* To construct the dip isogens a series of tangents are drawn on each folded surface and points of equal dip are connected on adjacent surfaces. This process is shown in figure 1-3 where the line abc is the 0° dip isogen and the line def is the θ° dip isogen.

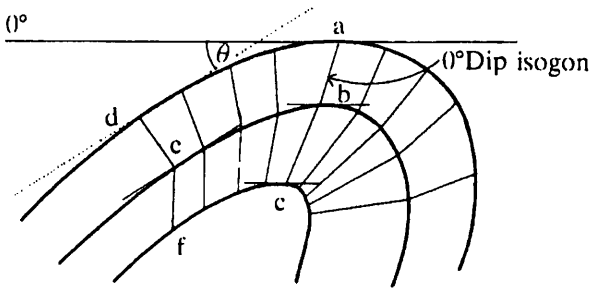

Figure 1-3: The construction of dip isogens. (After Price and Cosgrove (1990))

Ramsey (1967) used the convergence of dip isogens to classify folds into five classes (shown in figure 1-4). Class 1 folds have dip isogens that converge going from the outer to the inner surface. Classes 1(a) & 1(c) are strongly and weakly convergent. Class 1(b) is a parallel fold where the dip isogens are normal to the surface. Class 2 folds are called *similar folds* where the dip isogens are parallel to each other. Finally, class 3 folds are divergent.

One of the benefits of this classification is that it can be applied to individual *layers* of a *multilayer*, as the type of folding can change, where a layer is the material between two adjacent surfaces. The name multilayer is given to a set of sedimentary layers that buckle with the same wavelength and amplitude (termed *harmonic folding*).

Unfortunately this classification scheme does not include folds whose profiles

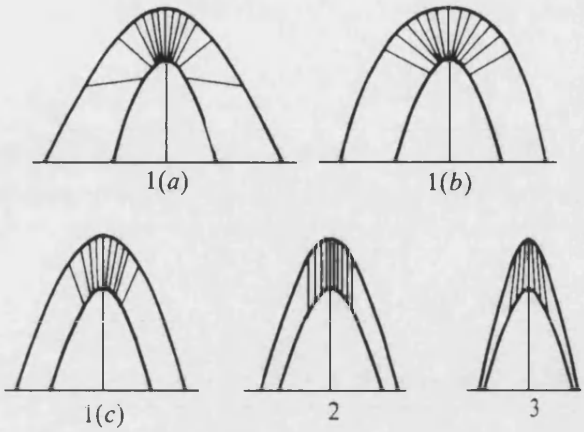

Figure 1-4: Classification based on dip isogen patterns. 1(a) Strongly convergent, 1(b) Parallel, 1(c) Weakly convergent, 2 Similar and 3 Divergent. (After Ramsey (1967))

contain straight limbs and sharp corners. These include kink bands (kink folds), chevron folds and box folds (see figure 1-5).

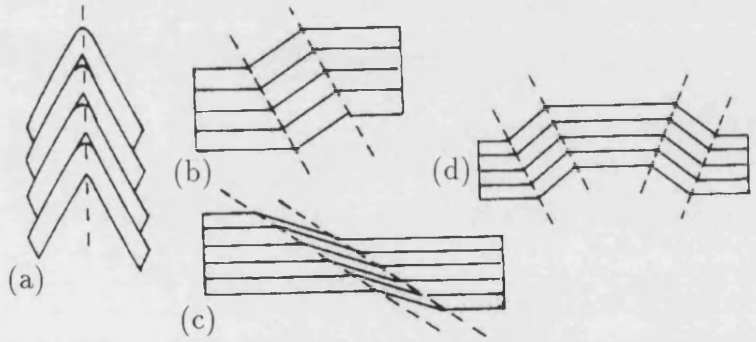

Figure 1-5: Geometry of (a) chevron fold, (b) reverse kink band, (c) kink band and (d) box fold. (After Price and Cosgrove (1990))

1.3.2 Strain distribution

According to Ramsey (1967) there are two typical strain states that can be encountered within a fold. Folds with these states are known as *flexural flow folds* (figure 1-6(a)) and *tangential longitudinal strain folds* (figure 1-6(b)).

Flexural flow folds are found in layers with a high anisotropy. As the layers

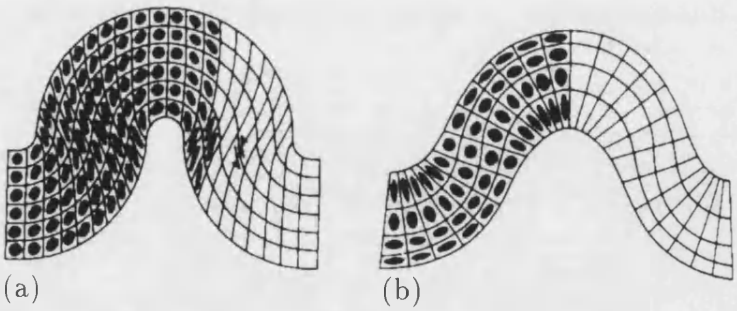

(a) (b)

Figure 1-6: The strain of a deformed layer (a) by flexural flow and (b) by tangential longitudinal strain. (After Ramsey (1967))

buckle the outermost layers slip over the inner layers toward the fold hinge zones. They have maximum strain at the inflection points and zero strain on the hinges. Conversely, tangential longitudinal flow folds are formed in isotropic materials and maximum strain is found at the hinges and none at the inflection points. The difference between these two strain states appears to be the same as the difference between Euler–Bernoulli beam theory (see section 1.4.1), where plane sections remain normal to the neutral axis, and Timoshenko beam theory (Timoshenko and Gere, 1963), where shearing is included so that although plane sections remain plane, they are not necessarily normal to the neutral axis. Here the term *neutral axis* refers to a line (on the fold profile) of zero strain.

1.3.3 Elasticity and viscosity

A body is said to be perfectly *elastic* if its stretching/compression obeys Hooke's law: the strain ϵ is directly proportional to the stress σ producing it or,

$$E = \frac{\sigma}{\epsilon} \tag{1.1}$$

where E is *Young's modulus* (or *elastic modulus*), which is a measure of the material stiffness. There is a limit to which a body can be distorted and returned to its original form called the *elastic limit.*

A similar property to the Young's modulus exists for an elastic material in shear or twisting called the *shear modulus* (or *rigidity modulus*) G. The shear

modulus relates the shear stress τ and the shear strain γ

$$G = \frac{\tau}{\gamma}. \tag{1.2}$$

Obviously a material can change state with a change in temperature or pressure. If folding takes place high in the Earth's crust where temperatures and pressures are relatively low then rocks are likely to be solid and elastic bending theory can be used to model their deformation. Typically rocks undergo an approximately linear deformation (Edmunds, 2005) and Young's moduli are reported in the range from 0.24 to 0.62 GPa for granite and from 1.02 to 1.07 GPa for diabase when measured with an overburden of 0.1 GPa (the *effective stiffness* tends to increase with pressure) (de Sitter, 1964). However, if folds form at great depths with high temperatures and pressures then the likelihood is that rocks are liquid and therefore must be modelled as such. In such circumstances the *viscosity* plays an important role.

Rather like an elastic solid obeying Hooke's law, a *Newtonian fluid* has a linear relationship between shear stress and shear strain rate

$$\eta = \frac{\tau}{\mathrm{d}\gamma/\,\mathrm{d}t}. \tag{1.3}$$

If the relationship is nonlinear, the liquid is called *non-Newtonian.* The *viscosity* η is analogous to the elastic shear modulus G.

1.4 Modelling with potential energy

In chapter 2 we provide some reasoning and justification for using elastic models for the buckling of layered rocks. The fundamental ideas for the buckling of elastic materials are developed by finding stationary solutions to energy based models describing a simply supported strut. These solutions help us to determine the *critical load*, the *post-buckling response* and the corresponding deflections. Under controlled end-shortening the critical load P^C is the load at which the strut starts to deflect and with continued end-shortening the behaviour of the

system is known as the post-buckling response.

We begin by developing Euler–Bernoulli bending theory and show how to solve the differential equation using the calculus of variations. The model is adapted to more geologically relevant applications by first adding a foundation and then considering the effect of having multiple layers, that are free to slide over one another, resulting in inter-layer friction.

1.4.1 The Euler strut

As the name suggests, the solution of the Euler strut was first derived by Euler (1744) using the *calculus of variations.* The geometry of a pin-ended strut is found in figure 1-7. Here the strut is simply supported and is of length L,

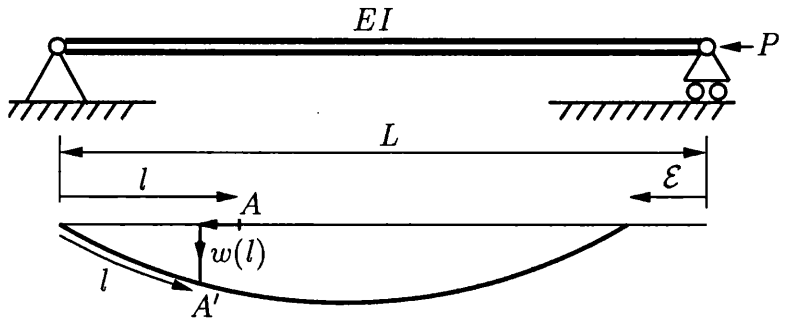

Figure 1-7: The pin-ended Euler strut. (After Thompson and Hunt (1973))

bending stiffness EI and is subjected to an axial load P. The strut is assumed to be axially inextensional (pure squash is neglected). Point A of the strut originally distance l from the left-hand support is displaced to A' with a vertical component $w(l)$. Since the arc-length of the centerline is inextensible, the displacement of the entire strut is determined by $w(l)$, $0 \leq l \leq L$. The function $w(l)$ is often called the *mode-shape.*

It is important for us to specify the boundary conditions as a clamped strut will behave differently to the pinned one. In the case of a pinned strut the

vertical displacement of the ends is zero so that

$$w(0) = w(L) = 0. \tag{1.4}$$

The second boundary condition is that the bending moment at the ends is zero which implies zero curvature at both ends of the strut

$$\ddot{w}(0) = \ddot{w}(L) = 0, \tag{1.5}$$

where dots denote differentiation with respect to l

Simple bending theory

Consider the strut shown in figure 1-7 and assume that under bending: shearing can be ignored (*pure bending*), longitudinal fibres remain parallel, the Young's modulus is the same in tension as in compression and the cross-section is symmetrical with respect to a vertical axis. Under these assumptions, the *bending equation* relates material and geometric properties as follows:

$$M = \frac{EI}{R} \tag{1.6}$$

where M is the bending moment, I is the second moment of area and R is the radius of curvature. The term EI is known as the *bending stiffness.* The following standard analysis shows this to be true. Consider a longitudinal fibre, depth y from the neutral axis (see figure 1-8). The unstressed line is known as the *Neutral Axis*, on one side of the line the material is in compression and on the other it is in tension.

Definition 2. *Curvature*

For a curve Γ the curvature κ is defined as

$$\kappa := \frac{\mathrm{d}\theta}{\mathrm{d}l} \tag{1.7}$$

where $\theta(l)$ is the angle Γ makes with the horizontal as a function of the arc-length l.

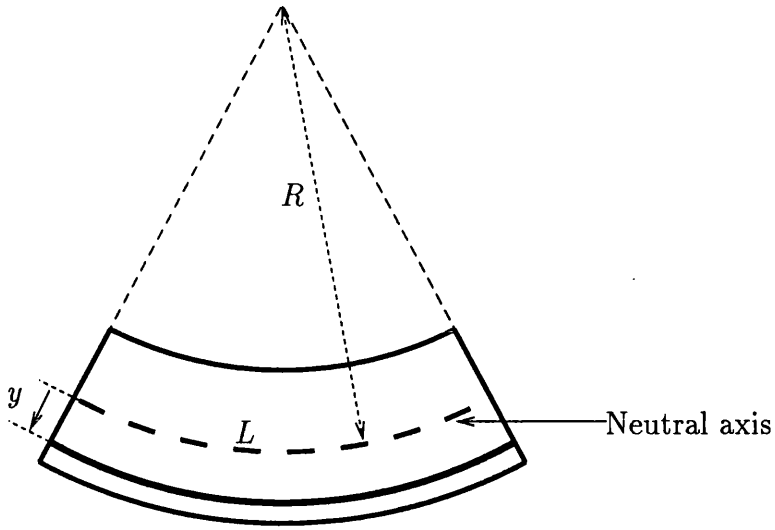

Figure 1-8: Pure bending of a rectangular strut

The extension is $L\epsilon$ where ϵ is the strain and it follows that

$$\frac{R}{R+y} = \frac{L}{L+L\epsilon} \tag{1.8}$$

Hence,

$$\epsilon = \frac{y}{R} \quad \text{or} \quad \frac{\sigma}{E} = \frac{y}{R}, \tag{1.9}$$

where σ is the stress. By integrating a strut along its depth d, the bending moment is

$$M = \int_{-\frac{d}{2}}^{+\frac{d}{2}} b\sigma y \, \mathrm{d}y \tag{1.10}$$

which leads to

$$M = \frac{EI}{R} = EI\kappa \tag{1.11}$$

where κ is the curvature and I is $bd^3/12$ for a strut of breadth b.

We consider small deflections first. By referring to the coordinate system of

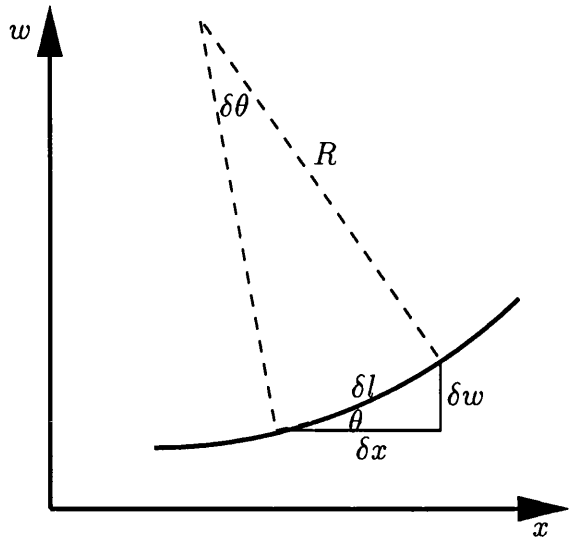

Figure 1-9: Curvature of a curve Γ

figure 1-9, for small values of θ,

$$\theta \approx \tan\theta = \frac{\mathrm{d}w}{\mathrm{d}x}, \quad \delta l \approx \delta x. \tag{1.12}$$

Differentiation gives

$$\kappa = \frac{\mathrm{d}\theta}{\mathrm{d}l} \approx \frac{\mathrm{d}\theta}{\mathrm{d}x} = \frac{\mathrm{d}^2 w}{\mathrm{d}x^2} \tag{1.13}$$

Substituting equation (1.11) gives

$$\kappa \approx \frac{\mathrm{d}^2 w}{\mathrm{d}x^2} = \frac{M}{EI} \tag{1.14}$$

the differential equation that governs the bending of a strut. This equation is valid for small values of θ, when shear is neglected and for perfectly elastic materials.

Next we derive a similar equation without making assumptions on the size of θ. Figure 1-9 shows that

$$\sin\theta = \frac{\mathrm{d}w}{\mathrm{d}l} \quad \text{and} \quad \frac{1}{R} = \frac{\mathrm{d}\theta}{\mathrm{d}l} \tag{1.15}$$

Differentiation and some manipulation gives the equation for the curvature for

large values of θ

$$\frac{\mathrm{d}\theta}{\mathrm{d}l} = \kappa = \frac{\ddot{w}}{[1-(\dot{w})^2]^{1/2}} \tag{1.16}$$

where dots denote differentiation with respect to l. Note that this formula reduces to the small deflection expression for the curvature if $|\dot{w}| \ll 1$.

Total potential energy function

The potential energy V of the Euler strut can be written as: Total potential energy = Strain energy stored - Work done by load,

or

$$V = U - P\mathcal{E} \tag{1.17}$$

where $\mathcal{E}$ is the end shortening. The *strain energy* (or *bending energy*) of a strut is defined as

$$U = \frac{1}{2}\int_V \sigma\epsilon \,\mathrm{d}V, \tag{1.18}$$

where V is the internal shear force. Let the area of the cross-section of the strut be A. Then by substituting equations (1.9), (1.11) and taking $\mathrm{d}V = \mathrm{d}A\,\mathrm{d}l$,

$$U = \frac{1}{2}\int_0^L \int_A E(l)\kappa(l)^2 y^2 \,\mathrm{d}A\,\mathrm{d}l \tag{1.19}$$

and $\int_A y^2\,\mathrm{d}A = I$, so

$$\begin{aligned} U &= \frac{EI}{2}\int_0^L \kappa^2\,\mathrm{d}l \\ &= \frac{EI}{2}\int_0^L (\ddot{w}^2 + \ddot{w}^2\dot{w}^2 + \ddot{w}^2\dot{w}^4 + \cdots)\,\mathrm{d}l \end{aligned} \tag{1.20}$$

The corresponding deflection of P is

$$\begin{aligned}\mathcal{E} &= L - \int_0^L (1-\dot{w}^2)^{1/2}\,\mathrm{d}l \\ &= \int_0^L (\frac{1}{2}\dot{w}^2 + \frac{1}{8}\dot{w}^4 + \frac{1}{16}\dot{w}^6 + \cdots)\,\mathrm{d}l \end{aligned} \tag{1.21}$$

(Thompson and Hunt, 1973). In this analysis it is assumed that $|\dot{w}| < 1$ and the expanded form of the integrals (1.20) and (1.21) are derived by considering the Taylor series. For a linear buckling analysis we need only consider the leading terms.

The calculus of variations

The idea behind the variational approach is that for a given load P the beam will naturally deflect to a state which is a stationary point of the potential energy. To find stationary solutions of the potential energy the calculus of variations is used. The total potential energy has the form $V = \int_0^L F(\ddot{w}, \dot{w})\,\mathrm{d}l$, where

$$F = \frac{EI}{2}\frac{\ddot{w}^2}{1-\dot{w}^2} - P(1-(1-\dot{w}^2)^{1/2})$$

. We now apply the calculus of variations by taking a small increment $\delta\ddot{w}$ of $\ddot{w}$ and $\delta\dot{w}$ of $\dot{w}$ to give

$$\delta V = \int_0^L \left(\frac{\partial F}{\partial \ddot{w}}\delta\ddot{w} + \frac{\partial F}{\partial \dot{w}}\delta\dot{w}\right)\,\mathrm{d}l \tag{1.22}$$

Integration by parts followed by some rearranging yields,

$$\delta V = \left[\frac{\partial F}{\partial \dot{w}}\delta w\right]_0^L + \left[\frac{\partial F}{\partial \ddot{w}}\delta\dot{w}\right]_0^L - \left[\frac{\mathrm{d}}{\mathrm{d}l}\frac{\partial F}{\partial \ddot{w}}\delta w\right]_0^L + \int_0^L \left(\frac{\mathrm{d}^2}{\mathrm{d}l^2}\frac{\partial F}{\partial \ddot{w}} - \frac{\mathrm{d}}{\mathrm{d}l}\frac{\partial F}{\partial \dot{w}}\right)\delta w\,\mathrm{d}l. \tag{1.23}$$

The condition for a stationary point is that $\delta V = 0$. To meet this condition for all possible deflections δw the last term must be zero and the terms in square brackets are then eliminated. The first and third square brackets are immediately

eliminated by the condition (1.4) and the second bracket by noticing that

$$\frac{\partial F}{\partial \ddot{w}} = EI\ddot{w}(1-\dot{w}^2)^{-1}$$

and applying the boundary condition (1.5).

By substituting in the expression for F and performing the differentiations with respect to l, $\dot{w}$ and $\ddot{w}$ we arrive at the *Euler equation* for a pin-ended strut

$$\dddot{w}(1-\dot{w}^2)^{-1} + 4\ddot{w}\dddot{w}\dot{w}(1-\dot{w}^2)^{-2} + \ddot{w}^3(1+3\dot{w}^2)(1-\dot{w}^2)^{-3} + \frac{P}{EI}\ddot{w}(1-\dot{w}^2)^{-\frac{3}{2}} = 0. \tag{1.24}$$

The Euler equation is solved by the zero solution and at a critical load $P = P^C$ the solution bifurcates to a buckled solution. At this load the zero solution changes stability (Thompson and Hunt, 1973). We see other solutions if an eigenvalue of the linearisation is zero.

1.4.2 Stability

Equilibrium solutions occur at all stationary points of the potential energy function with respect to the generalised coordinates, $\frac{\partial V}{\partial Q_i} = 0, \quad \forall Q_i \quad 1 < i < \infty$.

We may write the potential energy in a general form

$$V = V(Q_i; \Lambda^j) \tag{1.25}$$

where $\Lambda^j \quad 1 < j < J$ are a set of control parameters, such as the axial load or the magnitude of imperfections. *Equilibrium paths* are traced by distinguishing a parameter Λ^1 as a special bifurcation parameter and varying this whilst holding the other Λ^j constant then solving the resultant equilibrium equations for the Q_i (Thompson and Hunt, 1984).

As a strut buckles there is a loss in stability in the undeformed state and the equilibrium solution bifurcates to a buckled solution. The formal definition of stability is due to Liapunov and can be stated informally as (Thompson and

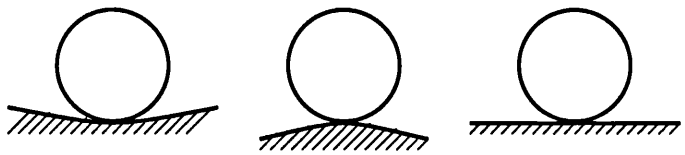

Figure 1-10: A ball on three surfaces to demonstrate the different states of equilibrium (a) stable equilibrium (b) unstable equilibrium (c) indifferent or neutral equilibrium. (After Timoshenko and Gere (1963))

Hunt, 1984):

Definition 3. *Stable equilibrium*

If all dynamical motions in phase-space in the vicinity of a statical equilibrium state remain in the vicinity for all time, then the state is termed *stable.* Conversely, if any one dynamical motion in phase-space starting in the vicinity of a statical equilibrium state carries the system away from the vicinity, then the state is termed *unstable.*

A simple analogy of stability is a ball in a potential well as shown in figure 1-10, (Timoshenko and Gere, 1963). In this figure there are three equilibrium states which we now describe. For case (a), any displacement of the ball on a concave surface will raise the centre of gravity and therefore its potential energy will increase and it will naturally return to its original position (stable equilibrium). In the second case (b), the opposite is true, on a convex surface a displacement will cause the potential energy to decrease and the ball will move further away from the original position (unstable equilibrium). Finally (c), on a flat surface it will remain wherever it is displaced to (neutral equilibrium).

This analogy follows directly from the axioms of stability (Thompson and Hunt, 1984) which state that a relative minimum of the total potential energy is a necessary and sufficient condition for stability.

1.4.3 Fourier analysis

We can represent the buckling mode shapes of the strut with $w(0) = w(L) = 0$ by considering a Fourier expansion

$$w(l) = \sum_{i=1}^{\infty} Q_i \sin \frac{i\pi l}{L} \tag{1.26}$$

where the Q_i are a set of generalised coordinates.

We define $V_{ij} = V_{ji} = \frac{\partial^2 V}{\partial Q_i \partial Q_j}$. These represent eigenvalues of the linearised solution about the unbuckled state, and since

$$\int_0^L \sin^2 \frac{i\pi l}{L} \, \mathrm{d}l = \int_0^L \cos^2 \frac{i\pi l}{L} \, \mathrm{d}l = \frac{1}{2}L \tag{1.27}$$

the diagonal energy coefficients of the linearised potential are

$$V_{ii} = \left[EI \left(\frac{i\pi}{L} \right)^4 - P \left(\frac{i\pi}{L} \right)^2 \right] \frac{1}{2}L \tag{1.28}$$

where $V_{ij} = 0$ for $i \neq j$. The critical buckling load may be found by setting $V_{ii} = 0$ (the stability changes) and solving for P as this is the point at which the system has a zero eigenvalue.

The critical buckling loads P_i^C are then given by

$$P_i^C = \frac{EI \left(\frac{i\pi}{L} \right)^4}{\left(\frac{i\pi}{L} \right)^2} = EI \left(\frac{i\pi}{L} \right)^2 . \tag{1.29}$$

Clearly, the lowest critical load is

$$P_1^C = EI \left(\frac{\pi}{L} \right)^2 \tag{1.30}$$

known as the *Euler buckling load.*

In this case the critical load depends on the length of the strut.

1.5 Foundations

The Euler strut model can be improved upon, to give a more accurate description of geological folding, by adding the behaviour of the material surrounding the layer into the model. This material is called a *foundation* and is often referred to as a *matrix* by geologists.

In chapter 5 we present the results of a set of experiments performed on layers of paper, to which we compare our mathematical model in chapter 6. In these experiments, the paper layers are placed between sheets of rubberised foam, and it is therefore the behaviour of this foam material that we are attempting to model. The most simple model for an elastic material such as the foam is the *Winkler* foundation, which is made up of independent closely spaced linear springs (see figure 1-11).

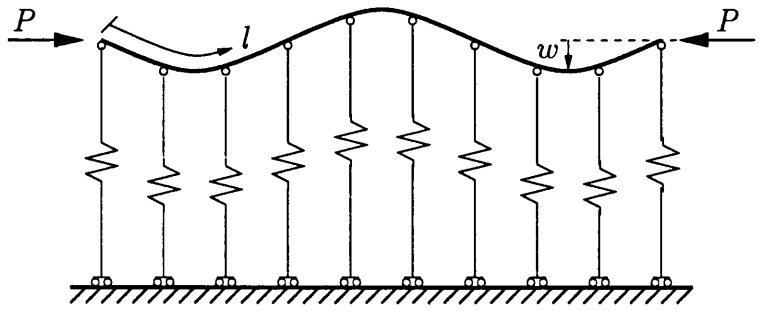

Figure 1-11: The strut on a Winkler foundation under loading

The Winkler model can easily be extended to approximate nonlinear behaviour by adding first destiffening and then restiffening components to the model so that the restoring force of $f(w)$ of each spring is a nonlinear function of w. This behaviour can be justified by considering the deformation of the foundation at a cellular level (Hunt and Wadee, 1998), (see figure 1-12).

For completeness, we make a remark about the behaviour of geological foundations. When geological folds are formed the layers of rock may be surrounded in a matrix of a less competent (less stiff) material. As we shall see in the literature review (chapter 2), Winkler models have also been suggested as models for geological foundations mainly owing to the ease of analysis. However, it

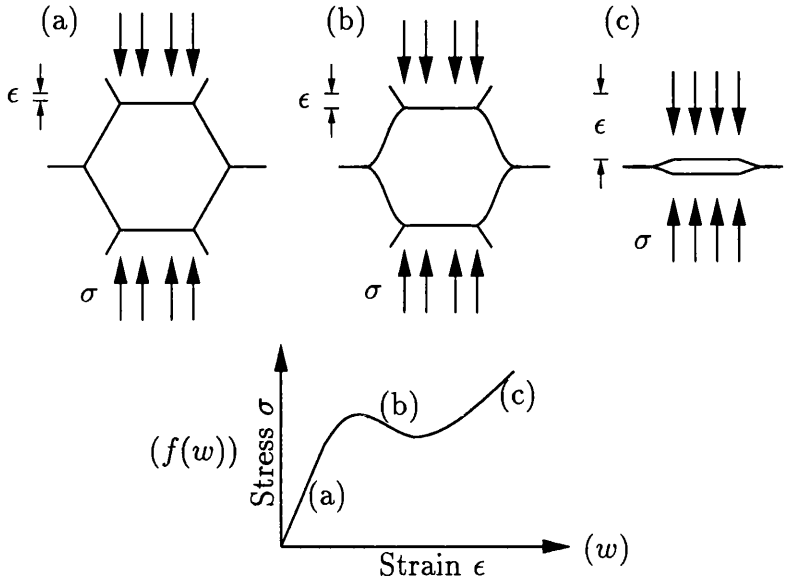

Figure 1-12: The compression of a foam at a cellular level. (a) Linearly elastic (b) Cell buckles: global softening (c) Opposite sides of cell in contact: global restiffening. (After Hunt and Wadee (1998))

is sometimes thought that either elastic or viscous half-space models are more appropriate (Hunt et al., 1997). Another alternative is the so called *Pasternak* foundation that assumes shear interactions between the springs, by connecting the ends of the springs to an incompressible beam.

1.5.1 Strut on a linear elastic Winkler foundation

Consider the pin-ended Euler strut (section 1.4.1) resting on an elastic (Winkler) foundation of stiffness k per unit length. We assume the springs are tied to the strut and anchored at infinity so that they remain normal to the original position of the centerline as the strut deflects. The strain energy stored by the foundation is (Thompson and Hunt, 1973)

$$U_F = \frac{k}{2}\int_0^L w^2 \,\mathrm{d}l. \tag{1.31}$$

In this model there are no boundary conditions. Instead we seek bifurcations of periodic form from the trivial solution. A repeat of the Fourier analysis

performed in section 1.4.3, with the additional term for the foundation gives

$$V_{ii} = \left[EI\left(\frac{i\pi}{L}\right)^4 - P\left(\frac{i\pi}{L}\right)^2 + \frac{k}{2}\right]\frac{1}{2}L \tag{1.32}$$

Setting V_{ii} equal to zero gives the critical buckling loads

$$P_i^C = \frac{\pi^2 EI}{L^2}\left(i^2 + \frac{1}{i^2}\gamma\right) \tag{1.33}$$

where

$$\gamma = \frac{k}{EI}\left(\frac{L}{\pi}\right)^4$$

(Thompson and Hunt, 1973). In this case the first mode does not necessarily produce the lowest critical load and is dependent on the material properties of the strut and the foundation.

By substituting in the value of $i = 1$ (one half wave)

$$P^C = \frac{EI\pi^2}{L^2} + \frac{kL^2}{\pi^2} \tag{1.34}$$

where we clarify that whereas in section 1.4.1 the length of the strut coincided with the wavelength, here L is a general wavelength (Timoshenko and Gere, 1963). The value of the critical load is independent of the number of waves.

The strut will buckle to the wavelength that gives the lowest critical load. Therefore we minimise with respect to the wavelength L to give

$$L = \pi\sqrt[4]{\frac{EI}{k}} \tag{1.35}$$

We observe that the addition of the foundation means that the wavelength is dependent on the foundation stiffness.

1.6 Multilayers and friction

The transition from modelling single layer folds to multilayer folds must account for two important effects. The first is the friction that occurs between the layers, which is related to the *overburden pressure*. The second relates to how the layers pack together, to avoid the formation of voids. This effect forms much of the novel work in this thesis and is the basis of chapter 3.

1.6.1 Friction

We know that bending a single layer compresses the inside of a fold and stretches the outside. If layers are stacked into a multilayer then for any pair of adjacent surfaces one is stretched and the other compressed. It follows that there must be slip between the layers working against friction. We model this effect with simple Coulomb friction and find that its inclusion replicates important nonlinear phenomena (Edmunds, 2005).

Coulomb Friction

The two basic laws of friction (*Amonton's laws*) are as follows:

1. The frictional force F is proportional to the normal load W;
2. The friction force between two solids is independent of the apparent area of contact.

The first law says that $F = \mu W$, where μ is known as the *coefficient of friction.* However, this law is contradicted by the static frictional force F_s that occurs at zero velocity. This load is dependent on the tangential load and to overcome this anomaly a friction indicator is introduced so that

$$\frac{F}{W} = \chi \mu_s \quad \chi \in [-1, 1], \tag{1.36}$$

where μ_s is the static coefficient of friction and χ is used to describe the direction of the friction. Adopting the terminology of Budd et al. (2003) we say that a system is *jammed* when a static body is sitting in equilibrium and χ is between -1 and 1.

A common addition to the two basic laws is a third law, due to Coulomb, which states that if the velocity is non-zero, the friction force is independent of the sliding velocity. Typically the static friction force is found to be greater than the kinetic force and we therefore introduce a second, kinetic, coefficient of friction μ_k, where $\mu_s > \mu_k$.

The laws are summarised in figure 1-13 which shows how the frictional force changes with velocity. Finally, we remark that this situation can create a stick slip mechanism whereby the two sliding solids move with a discontinuous velocity (Wensrich, 2005).

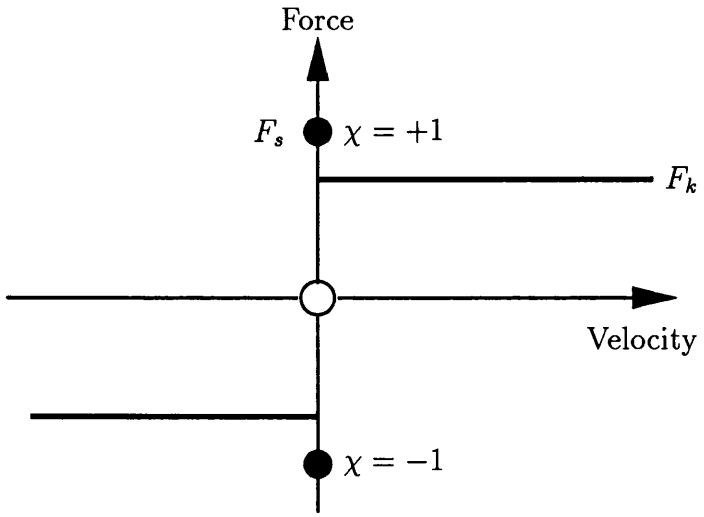

Figure 1-13: The frictional force changes with velocity. The static friction force F_s is the force required to start a body moving. The kinetic force F_k is the force required to keep the body moving.

1.6.2 Two layer parallel folding model with friction

Budd et al. (2003) considered a simplified two layer model with friction. Whereby two struts are stacked one on top of the other, embedded in a foundation of

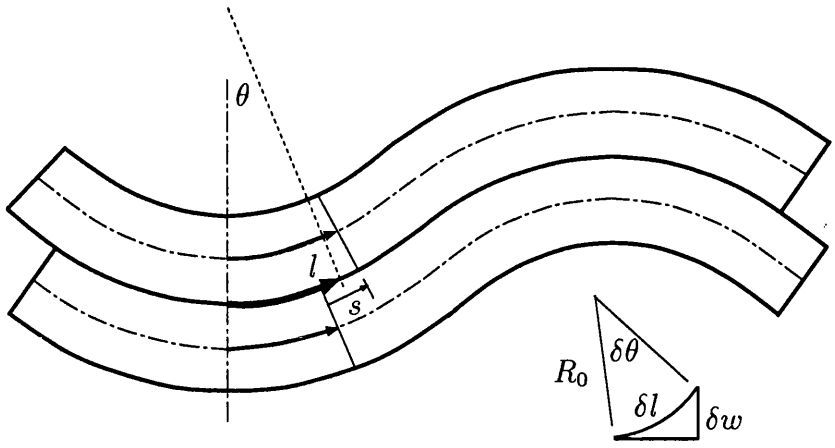

Figure 1-14: Slip between incompressible layers constrained to remain in contact. (After Edmunds (2005))

stiffness k per unit length. To bend without the formation of voids the layers must bend about the same centre of curvature. As we mentioned earlier, this creates a difference in length between the adjacent surfaces, resulting in slip between the layers (see figure 1-14).

We begin by accounting for bending two layers rather than one. Let the interface between the two layers bend with a radius of curvature R_0 and let the thickness of an individual layer be Δt. Then the centerline of the inner layer will have a radius of curvature $R_0 - \Delta t/2$ and the outer layer $R_0 + \Delta t/2$. The bending energy from both layers δU_B over an incremental length δl is then (Budd et al., 2003),

$$\delta U_B = \frac{1}{2} EI \left(\frac{1}{(R_0 - \Delta t/2)^2} + \frac{1}{(R_0 + \Delta t/2)^2} \right) \delta l. \tag{1.37}$$

If $\Delta t^2 \ll 4R_0^2$ then $\delta U_B = EI/R_0^2\, \delta l$ and substituting the equation for the curvature (1.16) the bending energy becomes

$$U_B = EI \int_0^L \left(\frac{\ddot{w}^2}{1 - \dot{w}^2} \right) \mathrm{d}l. \tag{1.38}$$

The condition on the layer thickness being much smaller than the radius of curvature can be seen physically in figure 1-15. In this figure, two thin layers are

given a large displacement and yet $\Delta t^2 \ll 4R_0^2$ still holds. Obviously, increasing either the layer thickness or the deflection makes the condition hold less strongly, or not at all.

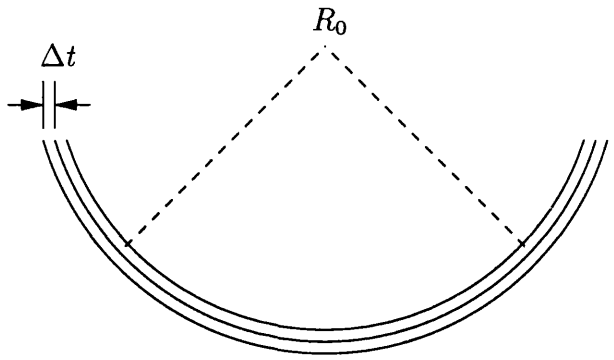

Figure 1-15: A thin layer implies the condition $\Delta t^2 \ll 4R_0^2$ is likely to hold for large deflections.

Now consider the friction. Let the amount of slip between two surfaces be s as shown in figure 1-14. To quantify the amount that the layers slip over one another we can again make use of bending theory. Over a small change in angle $\delta\theta$,

$$\delta s = \left(\frac{R_0}{R_0 - \Delta t/2} - \frac{R_0}{R_0 + \Delta t/2}\right)\delta l = \frac{R_0 \Delta t}{R_0^2 - (\Delta t/2)^2}\delta l. \tag{1.39}$$

We again make use of the simplification $\Delta t^2 \ll 4R_0^2$ so that

$$\delta s \approx \frac{\Delta t}{R_0}\delta l = \Delta t\, \delta\theta. \tag{1.40}$$

Since the slip is cumulative, the total slip s at l is

$$s = \int_0^l \mathrm{d}s = \int_0^\theta \Delta t |\,\mathrm{d}\theta| = \Delta t|\theta|. \tag{1.41}$$

where the modulus ensures that positive work is done regardless of the sign of θ. Integrating over $0 < l < L$ the work done against friction is (Budd et al., 2003)

$$U_\mu = \mu q \Delta t \int_0^L |\theta|\,\mathrm{d}l = \mu q \Delta t \int_0^L |\sin^{-1}\dot{w}|\,\mathrm{d}l, \tag{1.42}$$

where μ is the coefficient of friction and q is the overburden pressure per unit

length.

If both layers are subjected to the same end-shortening then the total potential energy is

$$\begin{aligned} V &= U_B + U_F - P\mathcal{E} + \chi U_\mu \\ &\equiv EI\int_0^L \left(\frac{\ddot{w}^2}{1-\dot{w}^2}\right) \mathrm{d}l + \frac{1}{2}k\int_0^L w^2\,\mathrm{d}l - P\int_0^L \left(1-\sqrt{1-\dot{w}^2}\right)\mathrm{d}l \\ &+ \chi\mu q\Delta t\int_0^L |\sin^{-1}\dot{w}|\,\mathrm{d}l. \end{aligned} \tag{1.43}$$

Here $\chi = \pm 1$ is a friction indicator that ensures that the friction acts in the right direction: $\chi = +1$ implies that the friction opposes the external force and therefore gives a positive energy contribution and $\chi = -1$ implies that friction acts in the same sense as the external force (Edmunds, 2005).

To find stationary points of V we restrict ourselves to the class of sinusoidal functions and assume a deflected shape

$$w(l) = Q\cos\left(\frac{\pi l}{L}\right). \tag{1.44}$$

In this case a cosine is chosen for the deflected shape because it gives the same solution as a sine function, but computation is simplified because friction is acting in the same direction along the length.

When substituted into the linearised potential the energy becomes

$$V = \frac{1}{2}EIL\left(\frac{\pi}{L}\right)^4 Q^2 - \frac{1}{4}PL\left(\frac{\pi}{L}\right)^2 Q^2 + \frac{1}{4}kLQ^2 + 2\chi\mu q\Delta t|Q|. \tag{1.45}$$

Setting $\partial V/\partial Q = 0$ we find the critical load (when $|Q| = \infty$) is given by

$$P^C = \frac{2EI\pi^2}{L^2} + \frac{kL^2}{\pi^2} \tag{1.46}$$

and minimizing with respect to L gives the wavelength

$$L = \pi\sqrt[4]{\frac{2EI}{k}}. \tag{1.47}$$

The friction has no role in the wavelength selection as it is assumed that there is no friction acting in the unbuckled state. However, as soon as the layers buckle, the friction significantly changes the stability of the system. This can be seen in the bifurcation diagram (figure 1-16). At constant load P, points between the two curves defined by $\chi = \pm 1$ are stationary positions where the system is jammed between two critical slip conditions (figure 1-16).

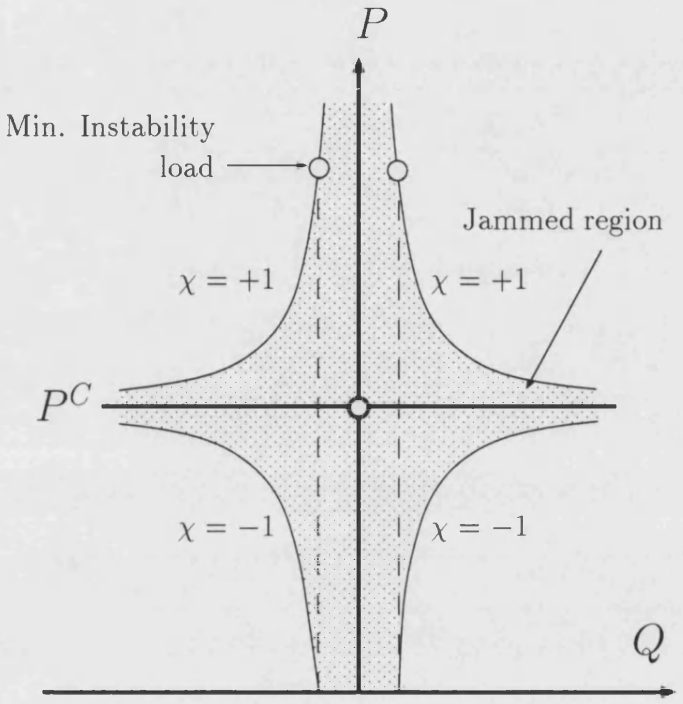

Figure 1-16: Bifurcation diagram indicating the jammed region for a constant coefficient of friction. (After Budd et al. (2003))

1.6.3 Geological measurements

The coefficient of friction in rocks will vary according to the type of rock and the pressure of the surrounding fluid (rocks are porous). Typical values for the coefficient of friction of dry rocks range between $0.4 < \mu < 1$ and the effect of fluid pressure is to lower these values slightly (the effect is not thought to be profound due to the extremely high pressure and the slow speed of sliding) (Edmunds, 2005).

An approximation of the overburden pressure is given by the *lithostatic pressure*, which is due to the weight of the material above the fold (Price, 1970). A reasonable value for this is $\approx$ 0.25 GPa (Price and Cosgrove, 1990; Price, 1970; McClintock and Walsh, 1962; Rudnicki and Rice, 1975) (cited by Edmunds (2005)).

1.7 Front propagation background

The level set method is a front propagation method that can be used to implicitly describe a curve (or surface) as it moves in its normal direction. In chapter 3 the level set method is used to describe the geometry of multilayered parallel folding. The theory behind the method appears in the second part of chapter 2. We will now define some of the terms that are used when describing front propagation methods.

Definition 4. *Interface*

The interface refers to the curve or surface that separates two distinct regions. In the current geological example an interface separates two adjacent layers of a multilayer.

Definition 5. *Lagrangian method*

The Lagrangian approach to interface evolution involves tracking the interface as it is advected. Typically, the interface is discretised into a set of marker particles that are then propagated to give the updated position of the interface.

Definition 6. *Eulerian method*

Eulerian methods employ a fixed grid approach. In these methods the interface is *captured* as it passes through the grid. We shall see in chapter 2 that this approach can have computational advantages over Lagrangian methods.

The level set method belongs to the class of Eulerian methods. Level set methods describe the interface via the solution of a partial differential equation. The interface is always given by the zero level set of a function $\phi(x, y, t)$.

Definition 7. *Courant–Friedreichs–Lewy (CFL) Condition*

The CFL condition is a stability condition that places a limitation on allowable time-steps Δt. The concept is that the distance a travelling wave passes in one step should not exceed the spatial step h such that (Courant et al., 1928; Morton and Mayers, 1994)

$$\Delta t < \frac{h}{\max |v|}, \tag{1.48}$$

where v is the velocity function.

1.8 Summary

This chapter has set the scene for the rest of the thesis. The first model presented for the folding of rock layers was the pin-ended Euler strut and it is found that the length of the strut determines the critical load at which the strut buckles. A more realistic model is the strut on a linear elastic foundation, which buckles to a periodic wave with the wavelength dependent on the stiffness of the foundation. Finally, multilayered systems are considered and the effect that friction has when two elastic layers buckle, but remain in contact as they do so.

Chapter 2

Literature review: The theories of geological folding and of front propagation methods

2.1 Introduction

Owing to the interdisciplinary nature of the present work, this chapter is broken into two parts. The first part concerns the geological folding literature, in particular references to parallel folding. Much of this information is covered by Edmunds in his thesis (Edmunds, 2005) and we provide a summary of his main arguments. Other major reference sources include the following: "*Analysis of geological structures*" (Price and Cosgrove, 1990), "*Styles of folding*" (Johnson, 1977) and "*An Outline of Structural Geology*" (Hobbs et al., 1976). The second part of the chapter looks at the suitability of different front tracking methods, when used in the geological application of describing the geometry of rock layers. We conclude that the level set method is well suited for this purpose, and proceed to provide details of the theory behind the method and its treatment of singularities.

2.2 Parallel folding

The study of multilayered folding began at the end of the nineteenth century with observations of rock formations and the subsequent classification of folds. Two of the most common types of folding in geology are the *parallel fold* (figure 2-1(a)) and the *similar fold* (figure 2-1(b)) which were first described by Van Hise (1894). The distinguishing property of the parallel fold is that thickness remains constant in each layer, so that each layer remains strictly parallel to a central layer (the orthogonal distance between any two layers is constant). In his description of parallel folding, Van Hise (1894) noted that the geometry of each layer is then usually different from its neighbouring layers. The similar fold is defined as having layers with identical geometries to each other.

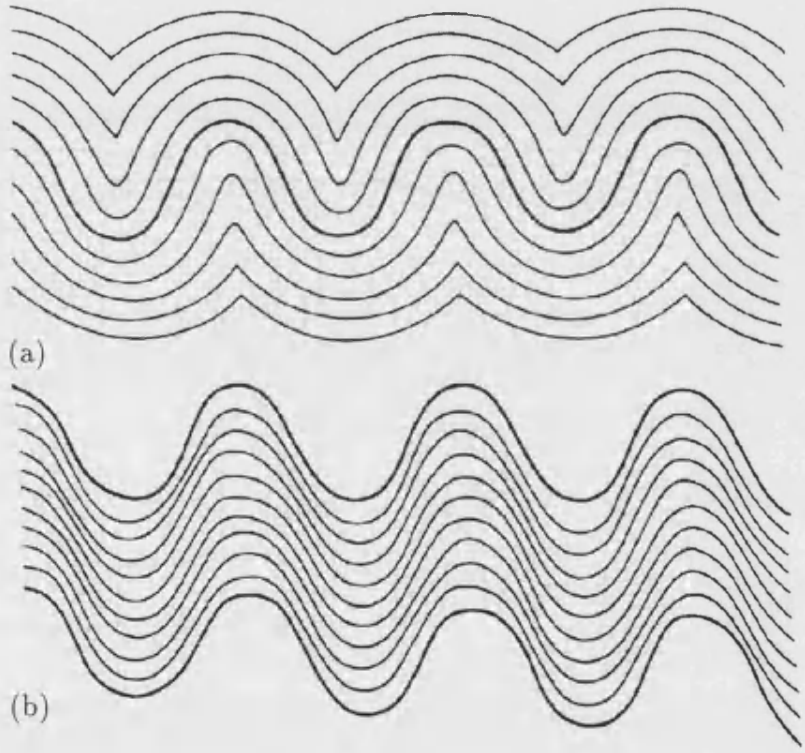

Figure 2-1: (a) Parallel folds and (b) Similar folds. (After Van Hise (1894)).

2.2.1 Elastic single layer solutions

The early attempts to model geological folds concentrated on a single layer using Euler–Bernoulli beam theory (Euler, 1744) discussed in chapter 1 and therefore neglected the effects of friction between the layers. The first person to apply the theory to rock layers was Smoluchowski (1909) who considered a simply supported elastic layer, which is resisted by the weight of the layer (the lithostatic pressure)

$$EI\dddot{w} + P\ddot{w} + \rho g = 0 \tag{2.1}$$

where as in chapter 1, dots denote differentiation with respect to l. A Fourier analysis of the type presented in chapter 1 yields a critical load of

$$P^C = EI\left(\frac{\pi}{L}\right)^2 + \rho g\left(\frac{L}{\pi}\right)^2 \tag{2.2}$$

and a corresponding wavelength

$$L = \pi\sqrt[4]{\frac{4EI}{\rho g}}. \tag{2.3}$$

Goldstein (1926) replaced the gravitational term with a resistive force to give the strut on a linear elastic foundation model seen earlier in section 1.5.1. A fourth order ordinary differential equation is derived by taking moments about a point along a strut that is supposed just buckled

$$EI\dddot{w} + P\ddot{w} + kw = 0. \tag{2.4}$$

A detailed analysis of equation (2.4) is provided by Wadee (1999b). We assume a solution of the form $w = a\sin(\omega l)$ where $\omega = (2\pi/L)$ and substitute into equation 2.4 to derive the characteristic equation

$$EI\omega^4 - P\omega^2 + k = 0. \tag{2.5}$$

There is a critical value of P, which we call $P^C = 2\sqrt{kEI}$ (note that this can be found by differentiation of equation 1.33 with respect to the wavenumber i in chapter 1). We are interested in compressive loading (positive P) and three cases arise. For $P > P^C$ the eigenvalues are imaginary and occur as two pairs about the real axis. In this case the form of the solution is sinusoidal. When $P = P^C$ the eigenvalues either side of the real axis take the same value. Finally, for $0 < P < P^C$ the unbuckled state is stable. Goldstein (1926) also considered clamped struts without finding any significant differences in the generic behaviour to that just described.

Early experimental work on folding was conducted by Kuenen and de Sitter (1938) (cited by Price and Cosgrove (1990)) who were attempting to understand the mechanism of parallel folding. In these experiments the effects of layer parallel compression were explored and compared when applied to a slab of unstratified clay, a paraffin wax layer, a pack of paper sheets and a rubber plate (shown in figure 2-2(a) to (d)).

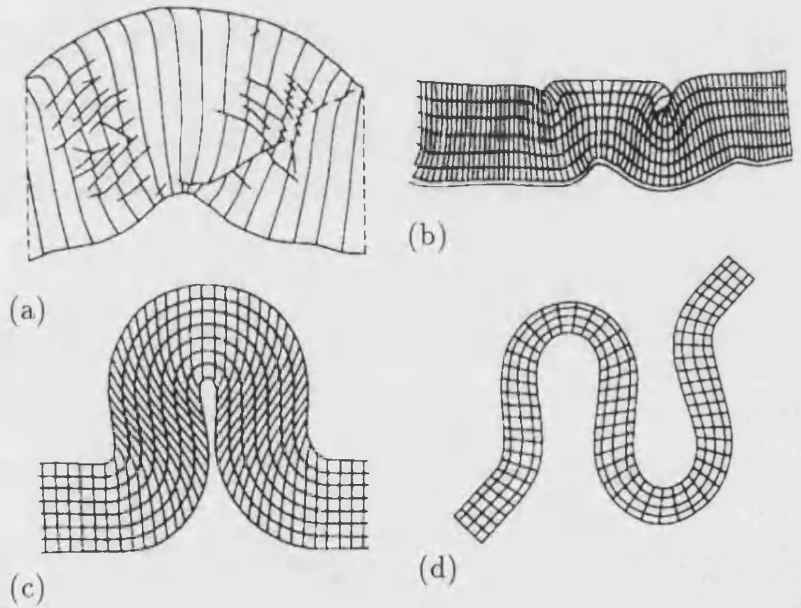

Figure 2-2: Sketches showing the effect of layer parallel compression on (a) a slab of unstratified clay, (b) a paraffin wax layer, (c) a pack of paper sheets and (d) a rubber plate. (After Kuenen and de Sitter (1938) cited by Price and Cosgrove (1990)).

These experiments demonstrate that folds can be formed with two different mechanisms, namely *flexural flow folds* (slip and flow) (figure 2-2(d)) and *tangential longitudinal strain folds* (figure 2-2(a)-(c)). Kuenen & de Sitter were surprised to find that in the experiments producing tangential longitudinal strain folds, the friction usually governed the deformation. As a final comment on these experiments, Edmunds (2005) notes that in the experiment on the paraffin wax layer it looks as though the fold formed in a serial manner.

2.2.2 Viscous layers

An alternative to the elastic foundation models presented in chapter 1 are viscous foundations surrounding either elastic or viscous layers.

Biot (1961) had a huge impact on the geological community which, to some extent, still exists to the present day (for example see Schmid and Podladchikov (2006)). In his 1961 paper, Biot (1961) consolidates his earlier work in the subject to produce a theory of the folding of stratified rocks. Previously, Biot (1937) had stated that bending an infinite beam on an elastic continuum (half-space) under lateral load was more realistic than on a Winkler foundation (see section 1.5). He applied a sinusoidal load to the continuum and showed this causes a sinusoidal deflection with the load dependent on the amplitude and wavelength. However, for a sine-like concentrated load, the bending moment close to the load were found to agree well with a Winkler foundation having the same maximum bending moment. Of great relevance to the 1961 paper was the 'general theory of the folding of a compressed plate embedded in an infinite medium' developed in an earlier paper (Biot, 1957). Fundamental to this paper was the introduction of the notion of a *dominant wavelength.*

Biot (1961) considered elastic and viscous (single) layers in an infinite viscous medium with initial imperfections. His theory is applicable in both cases through the *correspondence principle*, whereby the viscosity coefficient is replaced by the rigidity modulus. In the case of an elastic rod on a viscous Winkler foundation,

the familiar fourth order equation is derived (see equation (2.1))

$$q = EI\ddddot{w} + P\ddot{w} \tag{2.6}$$

where in this case q is the lateral restraining force per unit length.

The rod is assumed to deflect into a sinusoidal shape given by $w = w_0 \cos \omega x$, where the wavelength of the deformation is $L = 2\pi/\omega$. To support this shape the transverse load is also distributed sinusoidally so that $q = q_0 \cos \omega x$. Substituting the deflected shape into equation (2.6) yields

$$-q = P\omega^2 w - EI\omega^4 w \tag{2.7}$$

where the zeros have been dropped. Biot assumes that the lateral force is made up of viscous dashpots, such that

$$-q = \eta \frac{\mathrm{d}w}{\mathrm{d}t} \tag{2.8}$$

where η is the viscosity. We may then write

$$\eta \frac{\mathrm{d}w}{\mathrm{d}t} = w(P\omega^2 - EI\omega^4). \tag{2.9}$$

The general solution to equation (2.9) is given by $w = Ce^{pt}$ with

$$p = \frac{1}{\eta}(P\omega^2 - EI\omega^4). \tag{2.10}$$

When p is negative the deflection will die out and for positive p the amplitude will grow exponentially. The idea is that the ω that gives the maximum value of p will grow the fastest and will dominate the others. This value of ω is given by

$$\omega_d = \sqrt{\frac{P}{2EI}}, \tag{2.11}$$

corresponding to a wavelength of

$$L_d = 2\pi\sqrt{\frac{2EI}{P}} \tag{2.12}$$

called the *dominant wavelength.* This is the wavelength for which the rate of increase of the amplitude is maximum. It is interesting that this wavelength is independent of the viscosity; a finding that is also true in the case of an elastic plate embedded in a viscous continuum.

The theory was then developed to the case of a viscous layer with viscosity η embedded in a viscous continuum of viscosity η_1 with $\eta_1 \ll \eta$. The dominant wavelength in this case is independent of the axial load, but depends instead on the viscosity coefficients so that

$$L_d = 2\pi\Delta t \sqrt[3]{\frac{\eta}{6\eta_1}}, \tag{2.13}$$

where Δt is the thickness of the layer.

The expression for the dominant wavelength can also be calculated for a multilayer containing n viscous layers with perfect lubrication given by (Biot, 1957; Ramberg, 1961)

$$L_d = \pi\Delta t \sqrt[3]{\frac{n\eta}{6\eta_1}}, \tag{2.14}$$

We note that Biot and Ramburg both arrive at the same equation, although they derived it using different techniques and assumptions (Biot (1961) rederives his earlier result and assumes perfect slip whereas Ramberg (1961) assumes perfect cohesion between the layers). Biot revisits these ideas in his book "Mechanics of Incremental Deformation" (Biot, 1965).

By considering a viscous layer resting on a viscous continuum, the analysis was extended to study the effect of gravity on the dominant wavelength. In this case the dominant wavelength L_d again becomes dependent on the compressive load P

$$L_d = \pi\Delta t \sqrt{\frac{2P}{\rho_1 g \Delta t}}, \tag{2.15}$$

where g is the acceleration due to gravity and ρ_1 is the density of the matrix.

To test the viscous arguments and to show the possibility of more than one dominant wavelength Ramberg and Strömgård (1971) produced a set of multi-layer experiments. These were conducted on rubber layers (elastic) of different thicknesses embedded in gelatine. For small deflections, the experiments and theory had wavelengths and amplitudes in agreement with each other, although the same could not be said for larger deflections.

Biot's model is a linear model and therefore is only valid for the initial stages of buckling and is not accurate for large amplitude deflections. Edmunds (2005) questions the validity of Biot's analysis and makes four main points:

1. For permanent deformation of rocks it is more likely that rocks behave elastically (or elastoplastically) than as viscous fluids. (Biot assumes that any elastic behaviour can be ignored.)
2. The model is only relevant for infinitesimal amplitudes.
3. The model is restricted to periodic wavetrains (as opposed to serial folding).
4. The notion of a dominant wavelength is not correct over all times.

Proponents of the viscosity model include Chapple (1968) who modified the infinitesimal theory of Biot to include finite amplitude folds, with limb dips of up to 15°. Smith (1975) also considered the initial stages of buckling of a single Newtonian viscous layer embedded in a matrix with a different viscosity. He found that a layer of material of infinite length will deform homogeneously, no matter how big the contrast in viscosity is with the matrix. However, this process is unstable and the layer will either fold or pinch and swell with respect to its original thickness. In a second paper, Smith (1977) introduced non-Newtonian flow to model the deformation and found that in the case of folding it did not improve the comparison between the model and observation.

As a final remark we note that the viscous view of the buckling of layered structures is similar in spirit to a continuum-mechanics view of the buckling of elastic fibre structures. Although not applied to rock layers, Fu and Zhang (2006) present a continuum-mechanics model for kinkband formation in fibre-reinforced composites, which was able to predict the kink angle.

2.2.3 Elastic multilayers

Most of Biot's contemporaries were convinced by the viscosity approach to modelling and as we saw in the previous section, the majority of researchers neglected any elasticity in their models. Indeed, in 1990, on the issue of geologists neglecting elasticity in their models, Price and Cosgrove stated:

> 'Geologists for the last two decades, have been misleading themselves by ignoring this situation.'
>
> (Price and Cosgrove, 1990, p. 302)

However, there were some researchers who continued to develop the earlier, single layer elastic models. Currie et al. (1962) presented an elastic model concerning the mechanics of rock folding; in particular, looking at the folding of sedimentary rocks under tangential loads. The resulting energy-based model is developed using small deflection assumptions and is based upon Euler–Bernoulli beam theory. Unlike most other elastic models, Currie et al. (1962) introduce the *critical wavelength-thickness ratio*

$$\frac{L}{\Delta t} = \sqrt{\frac{\pi^2 E}{12\sigma_p}}, \tag{2.16}$$

where E is the Young's modulus of the beam and σ_p is the proportional limit of compressive stress. For values of the ratio greater than this value the beam will deflect sinusoidally and below it the beam will either buckle non-elastically or crush. Note that in contrast to chapter 1 the behaviour of the system is independent of the load.

A lateral restraint is added to the model as an elastic continuum (Biot, 1937) which, via the *correspondence principle*, leads to the same critical load and wavelength as Biot (1961). Currie et al. (1962) extended their model to a multilayer formulation by considering n layers of equal thickness Δt. Any friction between the layers was neglected, which was acknowledged by the authors to be unrealistic in geological situations. Also assumed was that the bending energy

of each layer would be the same as its neighbour's, so the total bending energy could be found by multiplying the bending energy of one layer by n. We shall see in the analysis of chapter 3 that this assertion is not valid for relatively thick samples undergoing moderate deflections. Assuming a sinusoidal deflection leads to

$$P^C = \frac{n\pi^2 E\Delta t^3}{3L^2} + \frac{E_0 L}{2\pi}; \quad L = 2\pi\Delta t\sqrt[3]{\frac{nE}{6E_0}} \tag{2.17}$$

where E_0 is the elastic modulus of the foundation (compare with the two layer expressions (1.46) & (1.47) given in section 1.6.2).

In order to test their model, the researchers looked at examples of geological folding and also performed a set of experiments. From their field observations they plotted a log–log graph of the wave length to dominant layer thickness, which agreed well with the theory. In the experiments, gum rubber strips are embedded in gelatine (the Young's modulus of the gelatine could be varied in each experiment) to create a multilayer with competent layers surrounded by incompetent material. The results of these experiments exposed problems with the model. The main issue was that after limb-dips of just 5°, the outside competent layers could not be considered sinusoidal (see figure 2-3). We will see that this becomes highly significant in the later chapters of the current thesis.

Figure 2-3: Gum rubber strips with equal thickness and layering sequence embedded in gelatine. (After Currie et al. (1962))

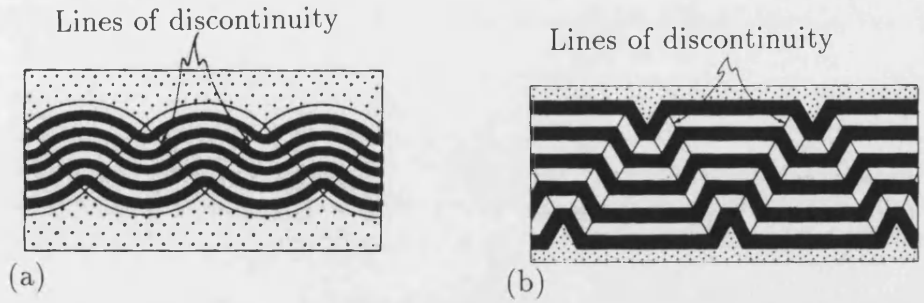

Figure 2-4: Lines of discontinuity in (a) concentric folds (b) kink bands. (After Johnson (1977))

Another geologist who continued to use elastic models was Johnson, whose work is summarised in his book, "Styles of folding" (Johnson, 1977). Here he points out that no-one truly knows how rocks behave at times of folding and therefore elastic models of folding may be equally valid (as viscous models). Furthermore, for rocks high in the Earth's crust he believed that elastic-plastic models were more appropriate. There are a number of points of interest for us to note in the book, which starts with some historical background. The first is Johnson's observation of *lines of discontinuity* in ideal folds. Lines of discontinuity arise when there is a discontinuity in either the curvature or the radius of curvature when the line is crossed. We can see in figure 2-4 that the lines of discontinuity are lines of zero curvature and hence have infinite radius of curvature. These lines are apparent in parallel folding (figure 2-4(a)) and kink banding (figure 2-4(b)), but do not exist in similar folds (as the *characteristic directions* are parallel). Obviously these lines also exist in geological examples and experimental folds as well as the idealised folds. Johnson was not able to formulate these ideas into a model, which he claimed was interesting but not particularly useful.

The underlying model first appears in a paper, co-authored with Honea, where a set of linearised equilibrium equations for compressible elastic materials are developed (Johnson and Honea, 1975). The wavelengths predicted by this model are then compared with "elementary folding theory" and shown to be in excellent agreement, which by their own admission reduces the importance of the model (Johnson, 1977).

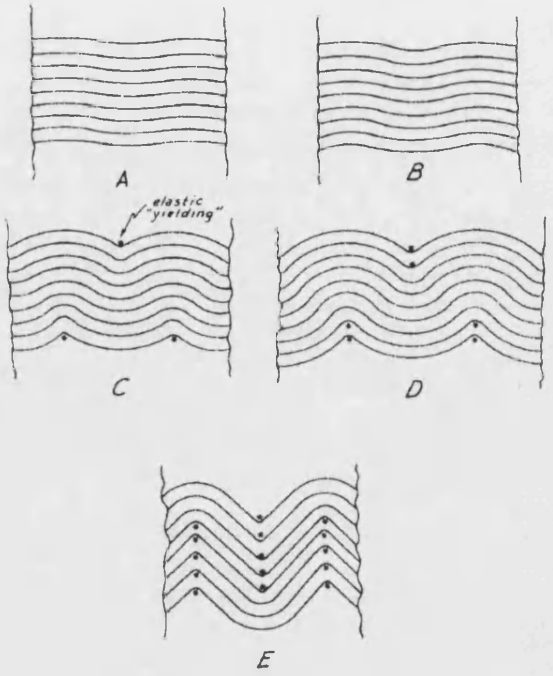

Figure 2-5: The transition from Similar-to-parallel-to-chevron folding. (After Johnson (1977))

Also of interest is the theory regarding the evolution of different folding scenarios. Here it is expected that after a period of pure squash, sinusoidal (similar) folds are the initial formation (formed as a wavetrain of Biot wavelength) after the critical load has been reached. This formation is unstable in multilayers, so as it grows, parallel folds form which are stable. With further end shortening, the yield point is passed at certain points along the layer and parallel folds are replaced by plastically formed chevron folds (figure 2-5).

Edmunds (2005) is quick to point out the deficiencies of this approach, the main one being that there was no explanation for parallel folding which occurs as a "higher order effect". Edmunds (2005) also questions the mechanism of the layers going from straight to buckled, which is deemed to be unrealistic.

At a similar time to Johnson, Hobbs et al. (1976) summarised the work on modelling the development of folds that had been done to date. The unanswered questions of the day are still largely unanswered today, including the fundamental

question, 'When a fold forms will it be rounded or sharp in profile?' On the subject of viscosity, they question the justifications that had been put forward to demonstrate that rocks should behave as ideally viscous fluids under geological conditions and conclude:

> 'What is needed most of all are better mathematical tools for handling the problems involved.'
>
> Hobbs et al. (1976, p. 201)

2.2.4 Multilayer folding models with friction

During the late 1970's there was an increasing body of evidence to suggest that rock folds form in a sequential manner (*serial folding*) rather than as a wavetrain (Price, 1970, 1975). Experimental evidence revealed that, in the majority of cases, parallel folds formed either sequentially (see figure 2-6), or as a stochastic localisation (where points along the multilayer amplify by random amounts at different times) (Blay et al., 1977).

The sequential view of folding added weight to the elastic argument and opened up new avenues of research, in particular the application of localisation theory. However, at the time localisation theory was in its infancy and these techniques were not used in a geological setting until the late 1990's, with one of the first papers being Hunt et al. (1997). The paper was exploratory in nature and as a consequence considered the buckling of a single layer confined by a foundation. Half-space foundation models are considered to be more realistic but had not been rigorously formulated in the nonlinear range. However, if a Winkler foundation is used a fourth-order partial differential equation is derived to which solutions can be found.

In a pair of complementary papers Budd et al. (1999) and Budd and Peletier (2000) develop a prescribed end-shortening model of a single elastic layer in a viscous matrix. Two foundations are considered: the half-space foundation and the Winkler foundation. An energy functional is derived and subsequently

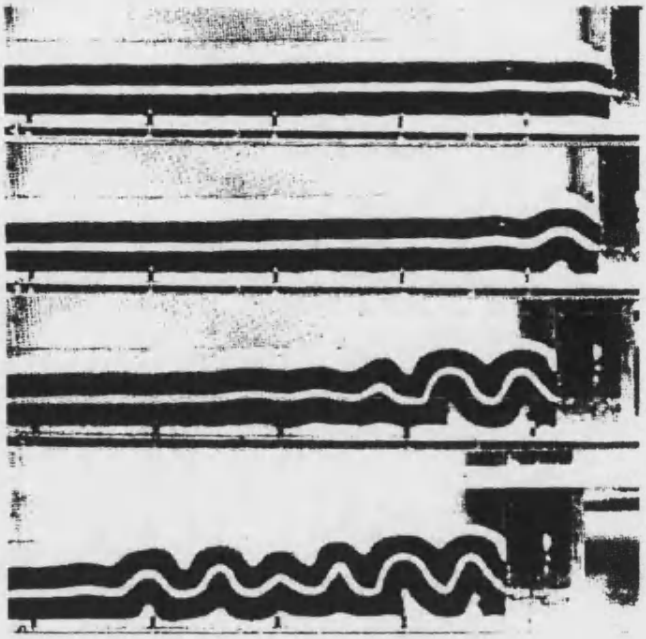

Figure 2-6: Serial folding of a gelatine multilayer, which can be seen being loaded from the right. (After Blay et al. (1977))

linearised; hence the model is valid for small deflections. In the case of the viscous Winkler foundation the governing differential equation becomes

$$EI\ddot{w}'' + P\ddot{w} + \eta w_t = 0 \tag{2.18}$$

Their findings were as follows:

1. An initial perturbation gives rise to a localised subsequent fold evolution.
2. The wavelength and the axial load change with time. An implication of this is that there is no dominant wavelength valid over all times, which contradicts Biot's analysis.
3. The long-term behaviour is approximately self-similar. A consequence of this is that the long-term behaviour is independent of the initial perturbation.

It is noted that geometric nonlinearities are not considered and that the

modelling of multilayers would produce different results. In fact, these ideas were soon applied to multilayered structures in a set of three papers on the formation of kink bands (Hunt et al., 2000, 2001; Wadee et al., 2004). The prototype model of the first paper was developed into a model that was capable of providing a good comparison to experiments performed on layers of paper in Wadee et al. (2004). Hunt et al. (2000) introduce a total potential energy formulation that contains friction between the layers. This formulation is advantageous because the *Maxwell stability criterion* can be used to find a lower bound to the critical displacement for kink banding. The major development of this model came in the third paper and was to allow transverse compressibility of the layers (Wadee et al., 2004). This meant that the orientation angle of the band could be determined, which in turn led to the lockup angle of the kink band.

More recently, parallel folds have been the subject of localisation techniques. Budd et al. (2003) developed a two layer parallel folding model with friction, as described in section 1.6.2.

The model is extended to explore the formation of serial folds in Hunt et al. (2006). To enable the formation of a second fold, the first fold must *restabilise* and *lockup*. The term restabilisation refers to the axial load going from decreasing with end shortening to increasing. At some point the amplitude of the first fold will stop increasing with continued end shortening, this can happen when opposing limbs come into self-contact, and in such circumstances we refer to the fold as being locked-up. To provide a restabilisation effect in the model a nonlinearity is added to the foundation via an extra term:

$$\frac{1}{4}C\int_0^L w^4\,\mathrm{d}l \tag{2.19}$$

where the coordinates are vertical displacement w and arc length l. Here $C > 0$ is a restiffening coefficient.

The first scenario considered in the paper was the formation of a single hump. Rather than assuming a sinusoid for the deflected shape, cubic B-splines were used as these are a better representation of a localisation than that of a Galerkin approximation which admits a periodic response. However, when compared, the

B-spline and the sinusoidal shapes lead to very similar results. The second situation involved two B-splines with independent maxima/minima, giving the model more freedom to select a waveshape. The main finding is that serial folding is the preferred solution when compared with spontaneous buckling.

In another development of the two-layer model it is extended to an n layer model (Edmunds et al., 2006). The multilayer model is compared with a set of parallel folding experiments performed on sheets of paper. The multilayer is given total thickness T and the central layer buckles to a radius of curvature R_0 as shown in figure 2-7. The model is valid whilst $T^2 << 4R_0^2$, which lim-

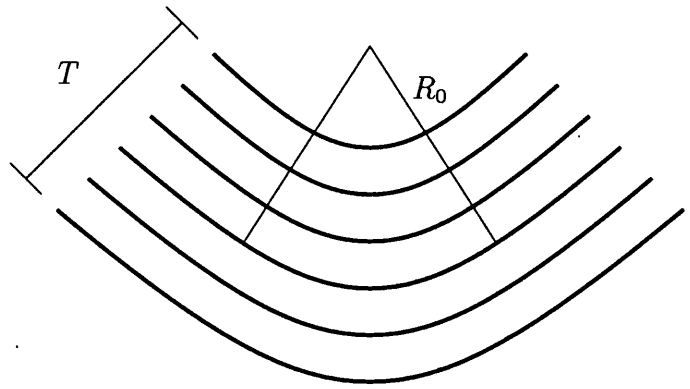

Figure 2-7: The total multilayer thickness T and the radius of curvature of the central layer R_0

its the amplitudes of the buckle when T is large. Implicit in this restriction is the assumption that the deflected shape of all the layers are approximately sinusoidal. Nevertheless, the model agrees well with the experiments, especially when a single localisation occurs.

However, the agreement relies heavily on the restiffening coefficient C which is found by curve fitting to a plot of a compression test performed on the foundation. In section 6.2.3 we outline why we think a linear model is more appropriate for the foundation as it is subjected to lateral loading. If this is the case, it means that a hardening effect of the foundation might not be the reason why a fold will restabilise and lockup.

In the first half of this literature review an argument has been put forward advocating the use of elastic layers to model geological folding. Furthermore,

when modelling a multilayer, it is vital to describe the layers separately so that effects such as friction between the layers can be included. There are also many instances in the literature where the geometry of a parallel fold is described and it is well known that the layers are only sinusoidal towards the centre of the multilayer (Van Hise, 1894; Currie et al., 1962; Johnson, 1977; Edmunds et al., 2006). However, this is something that has tended to be neglected in the mathematical models and is a situation that we intend to rectify. Our aim is to take a reference layer and to propagate it in its normal direction to find the deformation of all layers in a multilayer. Before we formulate the model we first give the literature surrounding front propagation methods to explore which is the most suitable for our purpose.

2.3 Front propagation methods

2.3.1 Introduction

Figure 2-8: The level set method applied to folding rock. The thick dashed line is a cubic spline fitted to the shape of the rock layer.

We motivate the use of front propagation methods by means of a figure.

By fitting a spline to a chosen reference layer from figure 1-1 (shown as a thick dashed line in figure 2-8) and propagating the resulting curve in both the forward and backward normal directions we see that the curve picks out the geometry of all the other rock layers as shown in figure 2-8. This observation leads us to believe that many of the geometrical features are imposed by the layers folding without forming voids. So with the simple assumption that the layers have an equal thickness and that no voids form between the layers, we get a good approximation for the multilayer geometry given the shape of one reference layer. We now give a review of some of the methods that are available to perform the normal propagation.

There are two main classes of method for tracking arbitrarily shaped interfaces: *Lagrangain methods* and *Eulerian methods* (Shyy et al., 1996). The Lagrangian representation involves tracking the interface with a series of marker particles, which explicitly give its position. The Eulerian methods usually employ a fixed grid formulation and the position of the front is not explicitly tracked but must be reconstructed from information stored at various grid points. Accordingly, Lagrangian and Eulerian techniques have their own strengths and weaknesses and the choice of method is often problem dependent.

2.3.2 Lagrangian versus Eulerian

The relative strengths of the two formulations are given as follows:

1. Interface definition

   The Lagrangian methods explicitly define the position of the front and therefore finding the accurate location of the interface is trivial. Eulerian methods require extra modelling to locate the interface, for example, based on cell fractions (volume-of-fluid techniques) or the distance away from the interface (level set methods).

2. Topological changes to the interface

   Eulerian methods automatically handle both mergers of separate interfaces and splitting of a single interface into multiple interfaces. On the other

hand, Lagrangian methods experience difficulty in handling topological change.

3. Discontinuous solutions and shocks

   Lagrangian methods have difficulties handling singularities as the interface can become multivalued. Eulerian methods employ a more global view and such problems are negated with the application of an appropriate *weak solution.*

In some applications, there also exist hybrid methods such as the Particle Level Set Method that attempt to combine the strengths of the Lagrangian and Eulerian techniques (Enright et al., 2002). This method is used when volume conservation is important.

2.3.3 Eulerian methods

In chapter 3 we show that singularities are a natural consequence of rock folding and we therefore choose to model the geometry of the layers with an Eulerian method. Two of the basic Eulerian methods are the *Level Set Method* and the *Volume-of-Fluid Method.* As their name suggests, volume-of-fluid techniques are designed to maintain constant volume (or area in 2D) and they have the benefits associated with other Eulerian methods (Noh and Woodward, 1976).

Volume-of-fluid methods break the computational domain into a number of cells that are given a value depending on the fraction of the cell that contains material inside the front. It is these cell values that are used to move the interface. With volume-of-fluid techniques it can be difficult to accurately relocate the front or to calculate its geometric properties, such as its normal or curvature. For our geological application, it is precisely the geometry of the interface that we are interested in and we therefore deem the volume-of-fluid methods as unsuitable for our purpose.

Shortly after the arrival of volume-of-fluid methods came the invention of another Eulerian based method (Dervieux and Thomasset, 1979, 1981), which

is now called the level set method. However, it was not until its reinvention in 1988 that it became well known to the research community (Osher and Sethian, 1988). We saw in chapter 1 that the level set method is an Eulerian, partial differential equations approach, that divides the domain into grid points that store values of the level set function $\phi(x, y, t)$. Typically, the values of ϕ are the distances away from the interface. If points on one side of the interface are assigned positive values (of the distance to the interface) and points on the other side negative then ϕ is known as a *signed distance function.* When ϕ is a signed distance function its level sets are evenly spaced, which means that as well as having the benefits associated with other Eulerian approaches, it is straightforward to compute the geometry of the interface.

2.4 The level set equation

Consider a function $\phi(x, y, t) : \mathbb{R}^2 \times \mathbb{R} \rightarrow \mathbb{R}^2 \times \mathbb{R}$. For each value of t the zero level set $\Gamma_t(x, y)$ of ϕ gives the position of a curve at a given time t and is given by the set of points $\{(x, y) : \phi(x, y, t) = 0\}$. In this case the subscript t refers to the time at which the zero level set is given rather than the derivative with respect to t. The evolution of this curve is given by the solution to the initial value problem

$$\phi_t + v|\nabla\phi| = 0 \tag{2.20}$$

given some prescribed function $\phi(x, y, t = 0)$. Here v is a speed function and can depend on many factors such as the curvature of the curve. Equation (2.20) is known as the *level set equation* and is derived more carefully in section 3.4.

2.4.1 Upwind schemes

To solve the level set equation we must discretise ϕ into a grid and find estimates for the temporal and spatial derivatives. Therefore, we let $[0, T]$ be the range of temporal values and discretise this into $N - 1$ intervals of size Δt such that

$t_i = i\Delta t$ with $i = 1, \ldots, M_1$. A similar division is made of the spatial coordinates with $x_j = jh$ with $j = 1, \ldots, M_2$ and for simplicity the same step is used in the y-direction $y_k = kh$ with $k = 1, \ldots, M_3$. We then consider an approximation $\Phi^i_{j,k}$ to the function $\phi(x, y, t)$ at the point $(x, y, t) = (jh, kh, i\Delta t)$.

A first-order accurate forward difference operator is

$$\left.\frac{\partial \phi}{\partial x}\right|_{x=jh} \approx \frac{\Phi((j+1)h, y, t) - \Phi(jh, y, t)}{h}, \tag{2.21}$$

a first-order backward difference operator is

$$\left.\frac{\partial \phi}{\partial x}\right|_{x=jh} \approx \frac{\Phi(jh, y, t) - \Phi((j-1)h, y, t)}{h}, \tag{2.22}$$

and a second-order central difference operator is given by

$$\left.\frac{\partial \phi}{\partial x}\right|_{x=jh} \approx \frac{\Phi((j+1)h, y, t) - \Phi((j-1)h, y, t)}{2h} \tag{2.23}$$

(Morton and Mayers, 1994). We can abbreviate these expressions by $D^{+x}\phi$, $D^{-x}\phi$ and $D^{0x}\phi$ respectively, with similar expressions for differentials with respect to y and t.

Given an initial value for the function ϕ we can use the approximations to the derivatives to construct a numerical method to find the position of the front at the next time step. We let $\Phi^i = \Phi(i\Delta t)$ be the current accepted value of ϕ, where Δt is an increment in time. The update of ϕ is given by Φ^{i+1} at time $(i+1)\Delta t$.

A simple method for the time discretisation is the *forward Euler Method* given by

$$\frac{\Phi^{i+1} - \Phi^i}{\Delta t} + v^i |\nabla \Phi^i| = 0 \tag{2.24}$$

where v^i is the given velocity field at time $t = i\Delta t$. To update ϕ we also require an approximation for the spatial derivatives $|\nabla \phi^i|$, which requires a little more thought than simply evaluating the derivatives (2.21)–(2.23). This is most simply

explained by first considering the one-dimensional version of (2.24),

$$\frac{\Phi^{i+1} - \Phi^i}{\Delta t} + v^i \Phi_x^i = 0, \tag{2.25}$$

where the sign of v^i determines whether the values of ϕ are moving to the right or to the left. If v^i is a constant and $v^i > 0$, the values of ϕ are moving from left to right and therefore $D^{-x}\phi$ should be used to approximate ϕ_x. Alternatively, if $v^i < 0$ then $D^{+x}\phi$ should be used to approximate ϕ_x. It is the *method of characteristics* that tells us which approximation to use for the choice of derivative. Methods that base the choice of approximation upon the sign of v^i are known as *upwind methods.* The example mentioned here is a first-order accurate upwind method so that the errors are $O(h)$. This is a stable method provided that the CFL condition is met (given in definition 7).

2.4.2 Discontinuities

An upwind scheme ensures that information flows in the correct direction. However, there is no guarantee that discontinuities are computed in a physically appropriate manner, so that characteristics flow into shocks. Osher and Sethian (1988) used the connection between Hamilton–Jacobi equations and conservation laws to find a method that can propagate discontinuities which correspond to an *entropy solution.* We now summarise their argument.

With our application of the level set method to parallel folding, we consider the level set equation with $v = 1$, so that $\phi_t + |\nabla\phi| = 0$, known as the *Eikonal equation.* This equation is an example of a wider class of equations called *Hamilton–Jacobi equations*, given by

$$\phi_t + H(\phi_x, \phi_y) = 0 \qquad \text{for } x \in \mathbb{R}^m \times (0, \infty) \tag{2.26}$$

The function H is the *Hamiltonian* which for our purposes is given by

$$H(\phi_x, \phi_y) = \sqrt{\phi_x^2 + \phi_y^2}. \tag{2.27}$$

Now consider the one dimensional version of equation (2.26) and differentiate with respect to x giving

$$0 = \phi_{tx} + H(\phi_x)_x = (\phi_x)_t + H(\phi_x)_x. \tag{2.28}$$

We now substitute $u = \phi_x$ to put the equation into *conservation form*

$$u_t + H(u)_x = 0. \tag{2.29}$$

Here $H(u)$ represents the flux function which we will now call $F(u)$. A well-known example of an equation in conservation form is the *continuity equation*

$$\rho_t + (\rho u)_x = 0, \tag{2.30}$$

for the conservation of mass, where ρ is the density of the material.

Integration of equation (2.29) gives

$$\begin{aligned} 0 &= \int_a^b (u_t + [F(u)]_x)\, \mathrm{d}x = \int_a^b u_t\, \mathrm{d}x + \int_a^b [F(u)]_x\, \mathrm{d}x \\ &= \frac{\mathrm{d}}{\mathrm{d}t} \int_a^b u\, \mathrm{d}x + F(u(b,t)) - F(u(a,t)) \end{aligned}$$

and

$$\frac{\mathrm{d}}{\mathrm{d}t} \int_a^b u\, \mathrm{d}x = F(u(a,t)) - F(u(b,t)). \tag{2.31}$$

This equation does not assume that the solution u is differentiable with respect to x and as such we seek *weak solutions.* Sethian (1985) asserts that the appropriate physical solution is the *entropy solution.* Entropy solutions say that the characteristics should flow into shocks, and the solution can be viewed as first arrival times. For example, in the case of a propagating flame front, the entropy criterion ensures that once a particle burns, it remains burnt. Another interpretation of the physically correct solution is the *vanishing viscosity solution.* This

solution is obtained by adding a regularisation to the Hamilton–Jacobi equation,

$$\phi_t^\epsilon + F(\phi_x^\epsilon) = \epsilon \phi_{xx}^\epsilon \tag{2.32}$$

where ϵ is a positive constant. Taking the limit $\phi^\epsilon \to \phi$ as $\epsilon \to 0$ gives an appropriate weak solution.

More formally, rather than defining the weak solution as a limit of smooth solutions, Crandall and Lions (1983) and Crandall et al. (1984) instead used a maximum principle:

Definition 8. *A bounded uniformly continuous function ϕ is called a viscosity solution of* (2.26) *provided for each $\psi \in C^\infty(\mathbb{R}^m \times (0,\infty))$*

$$\begin{cases} \textit{if } \phi - \psi \textit{ has a local maximum at a point } (x_0, t_0) \in \mathbb{R}^m \times (0,\infty), \\ \textit{then } \psi_t(x_0,t_0) + F(\nabla\psi(x_0,t_0)) \le 0 \end{cases} \tag{2.33}$$

and

$$\begin{cases} \textit{if } \phi - \psi \textit{ has a local minimum at a point } (x_0, t_0) \in \mathbb{R}^m \times (0,\infty), \\ \textit{then } \psi_t(x_0,t_0) + F(\nabla\psi(x_0,t_0)) \ge 0. \end{cases} \tag{2.34}$$

Crandall and Lions (1983) and Crandall et al. (1984) show that a) viscosity solutions admit the classical solution when it exists, b) viscosity solutions are unique and c) the solution produced by taking the limit of the smooth solutions ϕ^ϵ as $\epsilon \to 0$ is the viscosity solution.

We now appear to have two different ideas for the desired weak solution. However, Barles (1985) showed that the entropy condition picks out the viscosity solution so this is not a problem.

2.4.3 Solving Hamilton–Jacobi equations

As a first attempt we can make use of the idea of the solution being the limit of smooth solutions. We recall the regularised equation (2.32) and solve this with the upwind scheme

$$\frac{\Phi_j^{i+1} - \Phi_j^i}{\Delta t} = [\max(0, \Phi_j) D^{-x} \Phi_j^i + \min(0, \Phi_j) D^{+x} \Phi_j^i] + \epsilon D^{-x} D^{+x} \Phi_j^i \quad (2.35)$$

a process known as the method of *artificial viscosity*. This method is stable but has the significant drawback that it excessively smoothes sharp corners. Instead we try another approach and recall the conservation law (2.29). To ensure that discontinuities are projected at the correct speed we must write this equation in a discrete conservation form (the rate of change of conserved quantities is equal to a difference of fluxes) (Osher and Fedkiw, 2003). Typically, conservation form is derived for methods that evolve cell average values in time rather than nodal values. Let x_j be the centre of a grid cell $(x_{j-1/2}, x_{j+1/2})$. We then integrate (2.29) over the cell to obtain

$$\int_{x_{j-1/2}}^{x_{j+1/2}} u_t + F(u)_x \, \mathrm{d}x = \frac{\mathrm{d}}{\mathrm{d}t} \int_{x_{j-1/2}}^{x_{j+1/2}} u \, \mathrm{d}x + F(u_{j+1/2}) - F(u_{j-1/2}) = 0 \quad (2.36)$$

or

$$(\bar{u}_j)_t + F(u_{j+1/2}) - F(u_{j-1/2}) = 0 \quad (2.37)$$

where $\bar{u}_j = \int_{x_{j-1/2}}^{x_{j+1/2}} u \, \mathrm{d}x$. Equation (2.37) is in conservation form, and there exists a *numerical flux function* $\mathcal{F}(u_{j-1}, u_j)$ (or $\mathcal{F}(u_j, u_{j+1})$) which approximates $F(u_{j-1/2})$ (or $F(u_{j+1/2})$). $\mathcal{F}$ is required to be consistent so that $\mathcal{F}(u, u) = F(u)$. The *cell average* is defined as

$$u_{\mathrm{ave},j} = \frac{1}{h} \bar{u}_j. \quad (2.38)$$

Cell averages of u are directly evolved in time by the scheme. However, values of the cell boundary are also required to evaluate the fluxes. If we ignore this

difference and replace $u_{\text{ave},j}$ with u_j then

$$(u_j h)_t + F(u_{j+1/2}) - F(u_{j-1/2}) = O(h^2) \tag{2.39}$$

which is adequate for methods up to second order. For higher order methods Shu and Osher (1988) and Shu and Osher (1989) introduced a different numerical flux function $\mathcal{F}$ (of one variable) by the property that the real flux divergence is a finite difference of numerical fluxes

$$F(u)_x = \frac{\mathcal{F}(x + h/2) - \mathcal{F}(x - h/2)}{h} \tag{2.40}$$

at every point x so that

$$(u_j)_t + \frac{\mathcal{F}(x + h/2) - \mathcal{F}(x - h/2)}{h} = 0 \tag{2.41}$$

To make the link with entropy solutions we first define a *monotone scheme.* The scheme W of the form

$$u_j^{i+1} = W(u_{j-1}^i, u_j^i, u_{j+1}^i) \tag{2.42}$$

is monotone if W is a non-decreasing function of its arguments. Here, as we saw earlier with ϕ, we use the notation $u_j^i = u(jh, i\Delta t)$.

The salient point is that a monotone scheme in conservative form will obey an entropy condition (LeVeque, 1992).

2.4.4 The level set algorithm

Recall the Hamilton–Jacobi formulation of the level set equation $\phi_t + H(\phi_x, \phi_y) = 0$, or in one dimension $\phi_t + H(\phi_x) = 0$, which we have shown leads to the hyperbolic conservation law $u_t + [H(u)]_x = 0$ ($\phi_x = u$). We have also shown that the conservation law can be approximated by

$$\frac{u_j^{i+1} - u_j^i}{\Delta t} = -\frac{\mathcal{F}(u_j^i, u_{j+1}^i) - \mathcal{F}(u_{j-1}^i, u_j^i)}{h}$$

The value of F at the point $(j-1/2)h$ ($F_{j-1/2}$) is approximated by the numerical flux function $\mathcal{F}$ by $F_{j-1/2} \approx \mathcal{F}(u^i_{j-1}, u^i_j)$ and at $(j+1/2)h$ by $F_{j+1/2} \approx \mathcal{F}(u^i_j, u^i_{j+1})$. From the definition of u we can write

$$\phi_t + F(u) = 0. \tag{2.43}$$

To find ϕ^{i+1}_j with an Euler time approximation requires ϕ^i_j and $F(u^i_j)$, which by definition is given by $F(u^i_j) \approx \mathcal{F}(u_{j-1/2}, u_{j+1/2})$. We can now find the cell values for the centre of the cell using forward and backward differences

$$\phi^{i+1}_j = \phi^i_j - \Delta t F(u^i_j) \approx \phi^i_j - \Delta t \mathcal{F}(u_{j-1/2}, u_{j+1/2}) \tag{2.44}$$

and the fact that $\phi_x = u$ combined with the difference formulae, gives

$$\phi^{i+1}_j = \phi^i_j - \Delta t \mathcal{F}\left(\frac{\phi^i_j - \phi^i_{j-1}}{h}, \frac{\phi^i_{j+1} - \phi^i_j}{h}\right) \tag{2.45}$$

In two dimensions we can approximate $\phi_t + H(\phi_x, \phi_y) = 0$ by

$$\phi^{i+1}_{j,k} = \phi^i_{j,k} - \Delta t \mathcal{F}\left(\frac{\phi^i_{j,k} - \phi^i_{j-1,k}}{h}, \frac{\phi^i_{j+1,k} - \phi^i_{j,k}}{h}, \frac{\phi^i_{j,k} - \phi^i_{j,k-1}}{h}, \frac{\phi^i_{j,k+1} - \phi^i_{j,k}}{h}\right). \tag{2.46}$$

Osher and Sethian (1988) present numerical flux function given by the scheme

$$\mathcal{F}_{\mathrm{HJ}}(a_1, a_2, b_1, b_2) = \left[\max(a_1, 0)^2 + \min(a_2, 0)^2 + \max(b_1, 0)^2 + \min(b_2, 0)^2\right]^{\frac{1}{2}} \tag{2.47}$$

for forward and backward difference approximations a_1, a_2, b_1 and b_2. This scheme is upwind and satisfies the entropy condition with relatively little diffusion (Sethian, 1999).

The first order level set method is then

$$\phi^{i+1}_{j,k} = \phi^i_{j,k} - \Delta t \left[\max(v_{j,k}, 0)\nabla^+ + \min(v_{j,k}, 0)\nabla^-\right]^{\frac{1}{2}}, \tag{2.48}$$

where

$$\nabla^+ = \left[\max(D^{-x}_{j,k},0)^2 + \min(D^{+x}_{j,k},0)^2 + \max(D^{-y}_{j,k},0)^2 + \min(D^{+y}_{j,k},0)^2\right]^{\frac{1}{2}} \quad (2.49)$$

$$\nabla^- = \left[\max(D^{+x}_{j,k},0)^2 + \min(D^{-x}_{j,k},0)^2 + \max(D^{+y}_{j,k},0)^2 + \min(D^{-y}_{j,k},0)^2\right]^{\frac{1}{2}} \quad (2.50)$$

Here we have used the notation that $D^{+x}_{j,k} = D^{+x}\phi^i_{j,k}$. Higher order methods are available and for details see Sethian (1999) or Osher and Fedkiw (2003).

2.4.5 Efficient methods

Although the following methods have not been implemented in this thesis, we refer to them in the further work section (section 7.2) as possible improvements to the method presented in chapter 3. For the sake of completeness we therefore include a basic description of two more efficient methods.

Narrow Band Method

An inefficiency of the level set method is that the values of ϕ are stored and updated at all points of the grid, when the only interest (in our application) is in the position of the zero level set. An alternative is to concentrate on a band of cells around the interface, an approach known as the *Narrow Band Method* (Chopp, 1993). In the narrow band method, the only entries to be updated are those in a narrow band around the interface. Once the interface reaches the edge of the band, the signed distance function is re-calculated, the narrow band is re-formed around the updated position of the interface and the problem is solved until the interface hits the edge of the band again and so on. Hence, a balance is struck between saving time by updating only a small number of elements and the cost of re-calculating the signed distance function. The most obvious advantage of the narrow band method is the increased speed, but there are also more subtle benefits. For example, in the case of the standard level set method, with non-constant speed functions, the CFL condition (definition 7) must be applied for

the maximum v over the entire grid. However, with the narrow band technique this restriction is relaxed and the maximum v in the band determines the CFL condition.

The Fast Marching Method

The *Fast Marching Method* refers to an efficient algorithm that is used to solve a variation of the level set equation. This type of method was first presented in a pair of papers- Tsitsiklis (1994) and Tsitsiklis (1995) and was subsequently implemented by the level set community (Sethian, 1996). The fast marching method computes the arrival time $T(x, y)$ of the interface as it passes over each point in the grid. To stop $T(x, y)$ being a multivalued function we impose the condition that the interface can neither change the direction in which it is moving nor remain in the same place, so that the velocity v is either strictly positive or strictly negative.

The equation for the arrival function is simply given by

$$|\nabla T| v = 1, \tag{2.51}$$

subject to the boundary condition that $T = 0$ on the interface. This formulation has two benefits: firstly, it is not subjected to the CFL condition (because there is no time step) and secondly, it can be solved in an efficient and systematic manner. The idea is that grid points can be classified as either being *known, trial* or *far*. The *known* points have values of T that are accepted, *trial* points form a band of points adjacent to the *known* points and the remaining grid points are *far*. The method works by using efficient heap data structures to find the *trial* point with the minimum value of T, which we call T_{min}. T_{min} can then be added to the *known* values and removed from *trial*, because its value can not depend on any point with a larger value of T, due to *upwinding*. This reasoning also means that it is never necessary to revisit an accepted value. Neighbours of T_{min} that are in *far* are moved to *trial*. All *trial* neighbours of T_{min} have their T

values recalculated by solving the following quadratic equation

$$\left[\max(D^{-x}_{j,k}T, -D^{+x}_{j,k}T, 0)^2 + \max(D^{-y}_{j,k}T, -D^{+y}_{j,k}T, 0)^2\right]^{\frac{1}{2}} = \frac{1}{v_{j,k}}. \qquad (2.52)$$

The left hand side of equation (2.52) is a numerical Hamiltonian that in this case is more convenient to the one used in the level set method (Sethian, 1999). The process is then repeated by finding the next value of $T_{\min}$.

The efficiency and construction of the fast marching method means that it is often used in conjunction with the narrow band method to reinitialise the signed distance function.

2.4.6 Interesting applications of the level set method

Level set methods have been used in a vast number of applications including image processing (Malladi and Sethian, 1995), crystal growth (Russo and Smereka, 2000) and optimisation problems (Osher and Santosa, 2001). In fact we are not the first people to apply level set methods in a geological setting: they have been used to model the flow of lava from a volcano (Bourgouin et al., 2006) and also to seismic imaging problems (Cameron et al., 2006).

Crystal growth

We now highlight the application of the level set method to model faceted crystal growth as this construction is linked with the geometry of kink banding. If one takes an idealised geometry of a kink band layer and propagates it in its normal direction, according to the Entropy condition, the salient corners become rounded and a rarefaction fan forms (see figure 2-9(a) and section 3.4.3). In this case the entropy condition does not yield the observed solution (figure 2-9(b)) and a different approach is required. One such procedure is described by Russo and Smereka (2000), in which a tangential velocity is added to the motion. The extra velocity is tangent to the *facets*, the planes that make up the boundary of the crystal, and has the effect of modifying the interface's normal velocity when

it is not aligned along a facet.

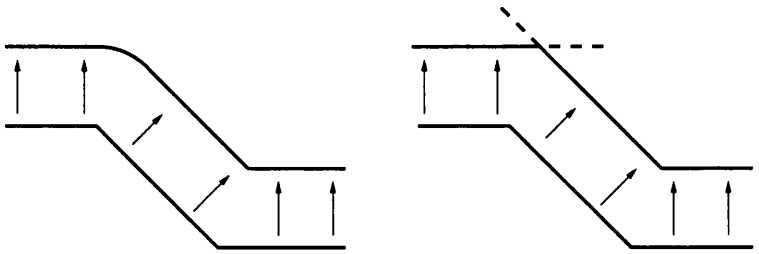

Figure 2-9: The propagation of a kink (a) a rarefaction fan forms according to the Entropy condition (b) the desired geometry.

Whilst this approach is of interest we have not included it in our geological folding model presented in this thesis. This is because the focus of the modelling is on parallel folding rather than kink banding.

2.5 Concluding remarks

The literature review has considered the development of different folding models. The alternative to the elastic models seen in chapter 1 are the viscous models, pioneered by Biot in the 1960's. However, there is enough doubt in the conditions in which rocks buckle for us to consider again the earlier elastic models; especially since the wavelengths given by viscous models can often disagree with those seen in reality.

A difficulty with modelling parallel folding of multilayered rocks is accounting for the fact that neighbouring layers will generally have differing geometries. In the second part of the literature review, we have motivated the idea of propagating a single central reference layer to find the geometry of all the other layers. The method that is best suited for this purpose is the level set method.

Chapter 3

Geometry of parallel folding

3.1 Introduction

Deformation patterns of multilayered materials under compression are strongly influenced by the way that the layers interact and slide over each other, and hence are different from the folding patterns of homogeneous materials. Multilayered folding arises naturally when layered materials are compressed in a direction parallel to the orientation of the layers when they are embedded in a medium which allows them to slide over each other, but not to separate. A very important example of such folding arises in geological systems under tectonic compression, particularly the buckling of layered sedimentary materials into a foundation (matrix). It also arises in the compression of layers of paper (as we shall see in the experiments of chapter 5) and of certain types of composite material. However, in all cases of folding the geometry is strongly governed by the constraints of the multilayered formation. A particularly interesting example of this is the natural formation of singularities. In such circumstances the pattern of the folding arises from a subtle interaction of the *geometrical* constraints imposed by the need for multilayers to fit together in specific patterns and the *mechanical* constraints of bending stiffness of the layers and interlayer friction.

Our main interest in the remainder of this thesis is in *parallel folding* (folds

where the orthogonal thickness remain constant - see section 2.2). This occurs when a finite number of layers, loaded in their plane, deform into a softer surrounding medium (foundation or matrix) while slipping at their interfaces (Edmunds et al., 2006). Parallel folds formed under large overburden pressures would be expected to limit voids between the layers (carrying a large energy penalisation), and we therefore take the process to be one of buckling in the complete absence of voids (Budd et al., 2003; Edmunds et al., 2006).

Recall the photograph of parallel folding shown in figure 1-1. Since the layers fit together without voids, each layer has a slightly different geometry from its neighbour; as a consequence, a singularity can appear on one interface, as seen in the figure. Here the layers appear smooth (almost sinusoidal) at the bottom of the picture, but as we move towards the top they become increasingly constrained by the geometry, until at a particular interface a singularity occurs. Past this singularity the layers take a non-differentiable 'V' shape, which propagates without change as we move further up; this V shape is seen also in kink bands and in chevron folds (see figure 3-1).

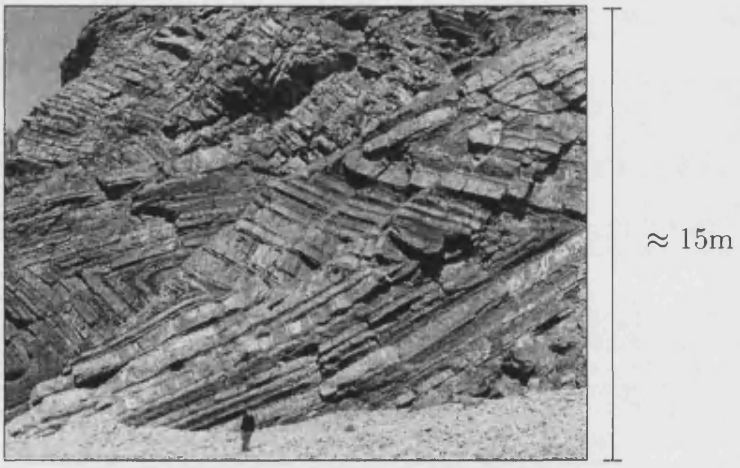

Figure 3-1: Chevron folding of rocks at Millook Haven, North Cornwall

Here we present a method for describing multilayer parallel folding based on the level set approach described in chapter 2. This naturally copes with the *geometry* of smooth parallel folding and also allows a consistent description of the geometry associated with singularity formation and kink banding (section 3.3).

In this chapter we will describe the geometry of multilayer folding, showing that this naturally leads to the formation of singularities. We then describe the level set method for calculating this geometry, and will discuss its performance and errors when singularities are present. Following this, in chapter 4, we will make use of the level set method to construct a potential energy function for the deformed material. In which, we will only look at such an energy functional in the case where no singularities are present as in the latter case additional consideration needs to be made of the energy associated with plastic deformations. From this energy functional we will be able to deduce the profile of the deformed multilayer material.

3.2 Application of the level set method to multilayer folding

Before we develop the theory of our method we provide some examples of propagating a reference layer using the level set method. In each case a spline function has been fitted to a central layer (thick dashed line) and the resulting curve propagated in the normal direction.

Example 1: Geological parallel folding.

The first parallel folding example was shown earlier in the comparison of figures 1-1 & 2-8. We reiterate that all of the important geometrical features of the layers are resolved, including the cusp and singularity formation as we propagate in the upward direction and the simple geometry in the downward direction.

A further geological parallel folding example is given in figure 3-2. Again we see that the geometry of the rock layers is closely matched by propagating a reference layer.

Perhaps a slightly more interesting example of the method applied to geological parallel folding is pictured in figure 3-3, which shows a *parasitic fold* formed

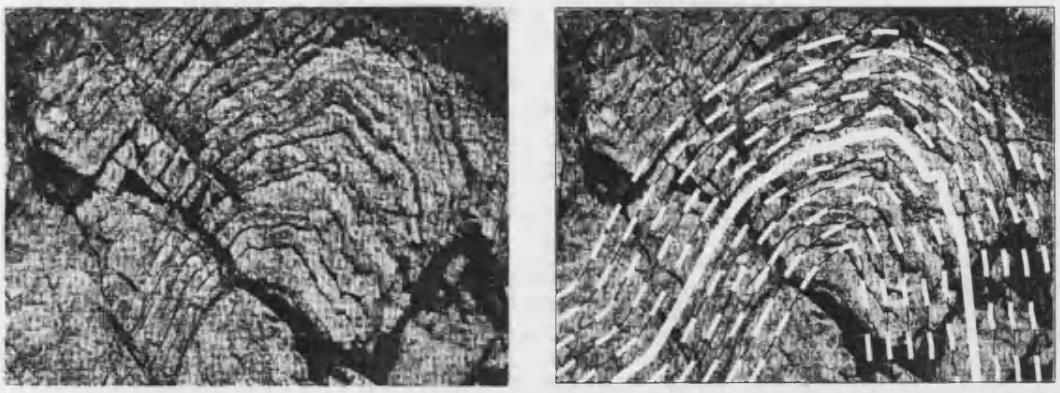

Figure 3-2: Parallel folding of limestone with dimensions 12 m × 9 m. (After Fletcher (1978)). In this case the thick white line is the reference layer.

in the hinge region of the larger-scale multilayer buckle. In this case the geometry of the multilayer buckle is well matched, but the parasitic fold is completely missed by the method. This small-scale fold only develops in the inner layers of the multilayer hinge and hence its geometry is not part of the reference (central) layer. However, we can see from the figure that the onset of the parasitic fold occurs near the point at which the method predicts a singularity. We suppose that the parasitic fold forms as a direct consequence of the singularity; if propagated in its normal direction the geometry would force the material to pass through itself or to lose length (see section 3.3.3).

Example 2: Parallel folding in layers of paper.

A series of experiments showing parallel folding in layers of paper have been undertaken (see chapter 5 for details). Figure 3-4 shows a serial parallel fold produced by a typical experiment. If we zoom in on the folded region of such an experiment and apply the level set procedure then there is excellent agreement as shown in figure 3-5. It is clear that the geometry of the whole multilayer can be determined by the geometry of a single layer.

Example 3: Geological chevron folding.

Finally, the method is applied to an example of geological chevron folding. In this case the method picks out the observed geometry of the rocks in one direction, but not the other. For a reentrant corner the entropy condition keeps

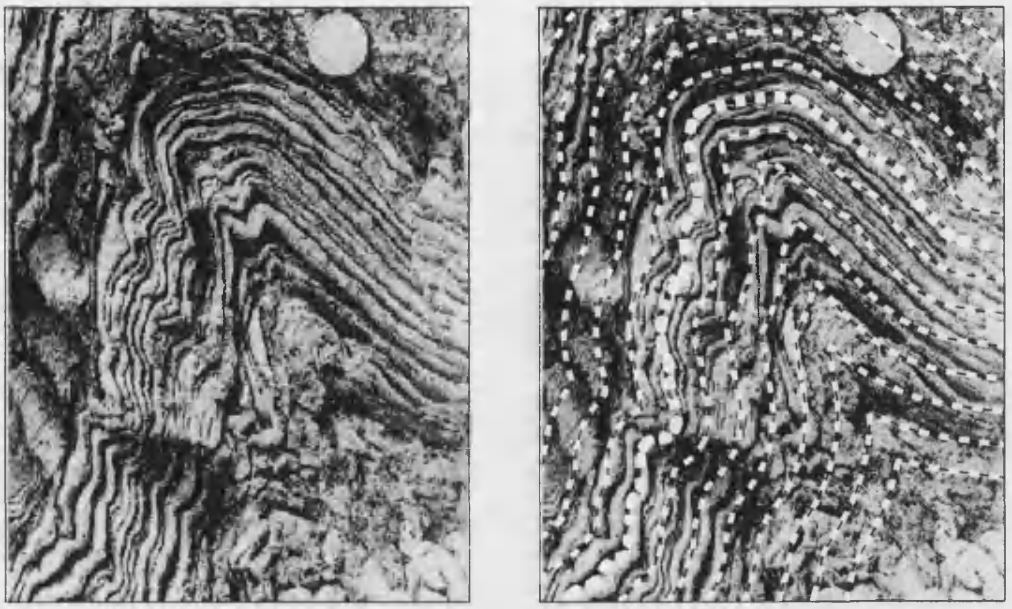

Figure 3-3: Parallel folding featuring a parasitic fold in the hinge region. Trearddur Bay, Anglesey, N. Wales. (After Price and Cosgrove (1990)). Here the thicker dashed line is the reference layer.

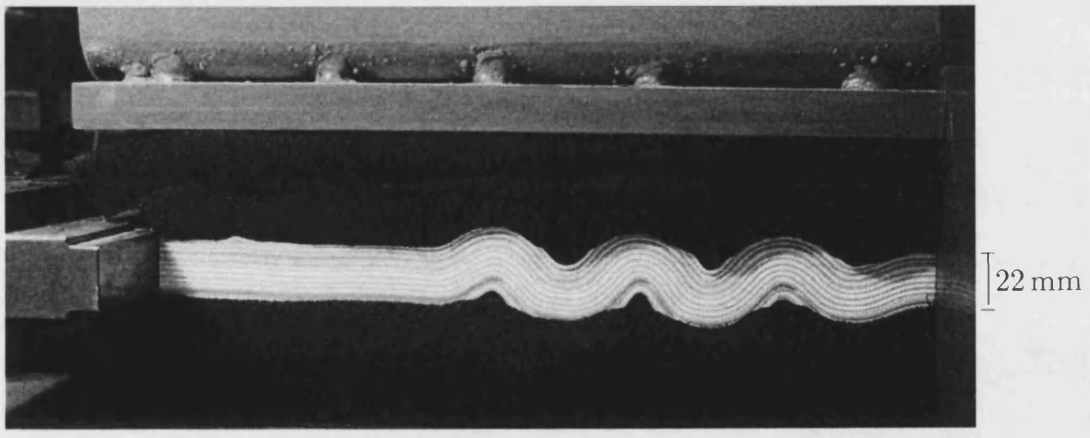

Figure 3-4: Parallel folding of 220 sheets of paper into foam. Here the black lines are for identification.

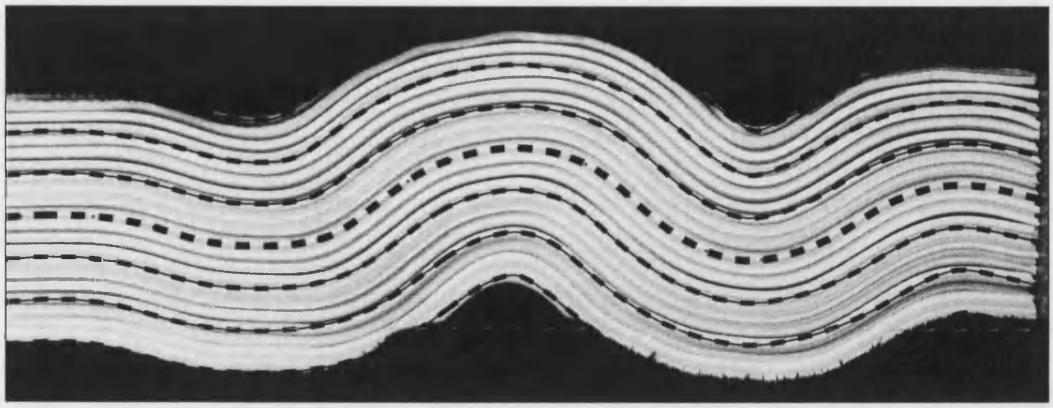

Figure 3-5: Shows good agreement between the experimental output and the level set curves shown as dashed lines. The thicker dashed line is the reference layer.

the corners sharp and the level set method closely approximates the geometry of the multilayer. Conversely, with a salient corner the entropy condition dictates that a rarefaction fan should form, which differs with reality. For a potential way of modelling the geometry in this case see section 2.4.6.

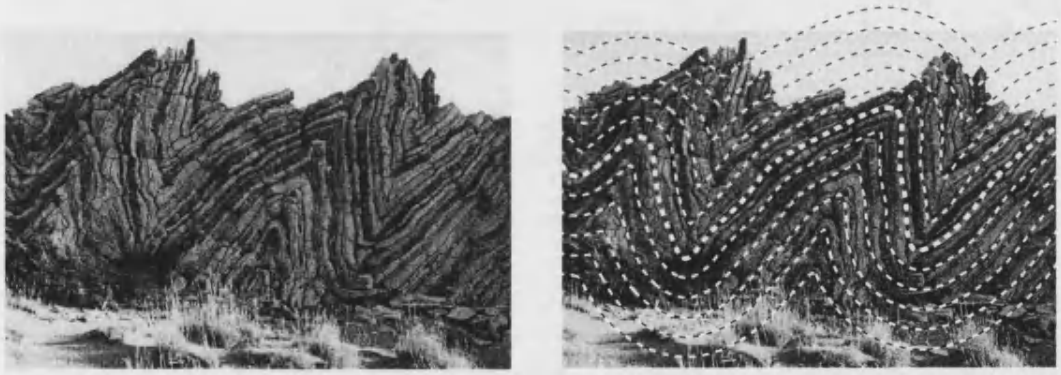

Figure 3-6: Chevron folding near Agios Pavlos, Crete. (After Couteau). The agreement is direction dependent; reentrant corners are closely approximated by the method, salient corners are not.

To apply this (essentially geometrical) method to find the actual form of the deformed material requires information only about the shape of a single reference layer. The level set method then gives the position of all the others and encodes all of the information of the geometry in terms of $\phi(x, y, t)$. To determine the shape of the reference layer requires additional calculations of the

mechanical behaviour of the system. In particular, finding the bending energy of the individual layers, the work done by friction and the work done in compressing the overall foundation into which the rock layers are embedded and this forms the basis of chapter 4. The combined energy terms provide a total potential energy function for the whole system of the deformed layers, which when coupled to the geometrical description of the layers given by the level set method contains a significant (stiffening) nonlinearity. We then look for states which are stationary points of this energy functional. As the energy can be expressed in terms of the single function ϕ this calculation is relatively straightforward.

3.3 The Lagrangian representation of multilayer folding

We now consider the basic process involved in the folding of multilayer materials in general and rocks in particular. We will then use a Lagrangian approach to describe the geometry of the patterns that can be observed. A natural consequence of this approach is the demonstration that singular behaviour arises very naturally in the folding of such materials.

3.3.1 The basic folding process

Sedimentary rocks can be formed under the seabed as loose particles (sediments), layed down layer upon layer, and forced together by the overburden pressure, caused by the material lying above. This process forms horizontal layers, which fold when tectonic plate movement produces an axial load (figure 3-7). In this figure we see identical layers of length L and width Δt, under an overburden pressure q, undergoing an end-shortening due to the compressive load.

Consider a layered material to be characterised by the position of each layer. We can then consider curves Γ_t, indexed by t, which describe the interface between layers. To describe such a layered material let the upper surface of top

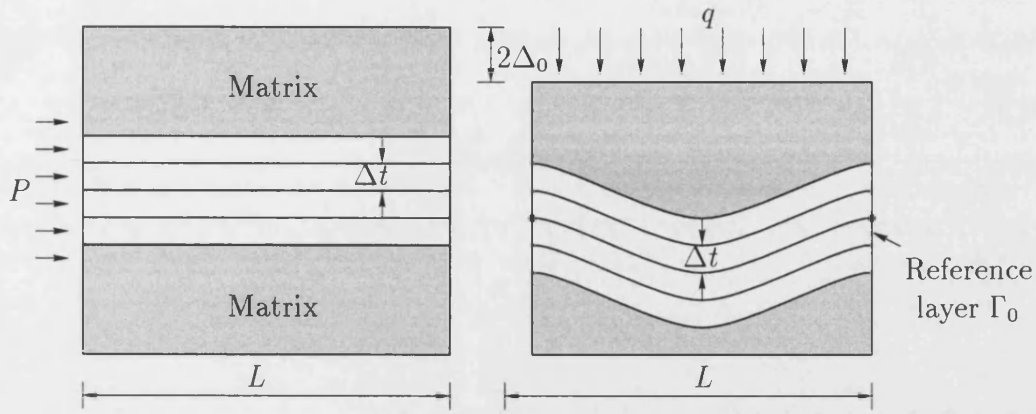

Figure 3-7: The assumed geometry showing the compressive force P and the overburden pressure q. Note that the angle of the layers with the horizontal at the endpoints is assumed to be zero.

layer be described by the curve $\Gamma_{n\Delta t}$ and the lower surface of the bottom layer by the curve $\Gamma_{-n\Delta t}$ with the interfaces between the other layers described by the curves $\Gamma_{i\Delta t}$, $-n < i < n$. In *parallel folding* we consider a situation where the layers are always in contact (so that $\Gamma_{i\Delta t}$ is well defined) and for which the curves $\Gamma_{i\Delta t}$ are separated by a *constant* normal distance Δt. The geometry of a set of curves with parallel folding can then be described by taking a *reference curve* (without loss of generality Γ_0) and propagating this curve in a normal direction a distance $i\Delta t$ to give the curve $\Gamma_{i\Delta t}$. Generally, the shape of $\Gamma_{i\Delta t}$ will differ from Γ_0 (although the chevron folding phenomenon of figure 3-1 gives an example where an identical family of curves can coexist). In particular, an initially smooth curve Γ_0 may give rise to curves $\Gamma_{i\Delta t}$ with singularities and sharp corners, as seen in figure 1-1.

3.3.2 The Lagrangian Representation of parallel folding

We now give a Lagrangian calculation of the process of parallel folding and show that the length of the interface is conserved, provided a) the surface remains smooth (ie. no singularities develop); and b) that the angle of the interface with the horizontal is the same at either end.

To describe the folding process in a Lagrangian frame we describe the set of

curves parametrically via the functions $\Gamma_t : \mathbb{R}^2 \to \mathbb{R}^2$ so that

$$\Gamma_t = \{(x(s,t), y(s,t)) : s \in [0,1]\}.$$

The parallel folding assumption is that the *normal separation* between two curves parameterised by $t = t_1$ and $t = t_2$ is given by $|t_2 - t_1|$ and does not depend on s. This assumption leads to a simple construction of the *entire* set of curves for all t, given a reference curve for $t = 0$. The exact position of $\Gamma_{i\Delta t}$ at time t may be constructed by advancing each point of Γ_0 in its unit normal direction, $\mathbf{n}$, a distance $t = i\Delta t$ (Sethian, 1999) (figure 3-8) where

$$\mathbf{n} = \frac{(-y_s^0, x_s^0)}{\sqrt{(x_s^0)^2 + (y_s^0)^2}}. \tag{3.1}$$

Here the suffix 0 refers to the reference curve.

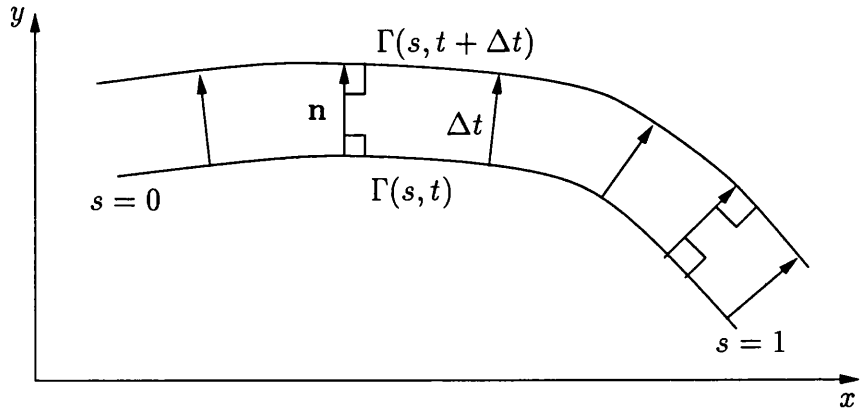

Figure 3-8: A smooth curve propagating with unit speed.

It follows from standard analysis that for each fixed $t = i\Delta t$ the Lagrangian description of Γ_t takes the form (Sethian, 1999)

$$\Gamma_t = \left\{(x(s,t), y(s,t)) = \left(\frac{-y_s^0 t}{((x_s^0)^2 + (y_s^0)^2)^{\frac{1}{2}}} + x^0(s), \frac{x_s^0 t}{((x_s^0)^2 + (y_s^0)^2)^{\frac{1}{2}}} + y^0(s)\right)\right\} \tag{3.2}$$

Equation (3.2) is valid for all $t = i\Delta t$, although the resulting curve may have points of singularity characterised by a lack of a well-defined normal vector.

To find $x_s(s,t)$ and $y_s(s,t)$ we differentiate equation (3.2) with respect to s to obtain:

$$x_s(s,t) = \frac{-((x_s^0)^2 + (y_s^0)^2)^{\frac{1}{2}} y_{ss}^0 t + y_s^0 t(\frac{1}{2}((x_s^0)^2 + (y_s^0)^2)^{-\frac{1}{2}}(2x_s^0 x_{ss}^0 + 2y_s^0 y_{ss}^0))}{(x_s^0)^2 + (y_s^0)^2} + x_s^0 \tag{3.3}$$

and

$$y_s(s,t) = \frac{((x_s^0)^2 + (y_s^0)^2)^{\frac{1}{2}} x_{ss}^0 t - x_s^0 t(\frac{1}{2}((x_s^0)^2 + (y_s^0)^2)^{-\frac{1}{2}}(2x_s^0 x_{ss}^0 + 2y_s^0 y_{ss}^0))}{(x_s^0)^2 + (y_s^0)^2} + y_s^0. \tag{3.4}$$

These expressions can be simplified by considering the curvature κ given by

$$\kappa(s,t) = \frac{y_{ss}x_s - x_{ss}y_s}{(x_s^2 + y_s^2)^{\frac{3}{2}}}, \tag{3.5}$$

so that

$$(x_s(s,t), y_s(s,t)) = (x_s^0, y_s^0)(1 - \kappa(s,0)t) \tag{3.6}$$

where $\kappa(s,0)$ is the curvature of the reference curve at the parameter value s. We make the significant observation that this vector vanishes (and hence we can not define a normal vector) when $t = 1/\kappa(s,0)$ which is the radius of curvature of the reference curve at this point. By moving forward t and then backwards by the same amount, it is immediately clear that

$$(1 - \kappa(s,0)t)(1 + \kappa(s,t)t) = 1$$

so that

$$\kappa(s,t) = \frac{\kappa(s,0)}{1 - \kappa(s,0)t}. \tag{3.7}$$

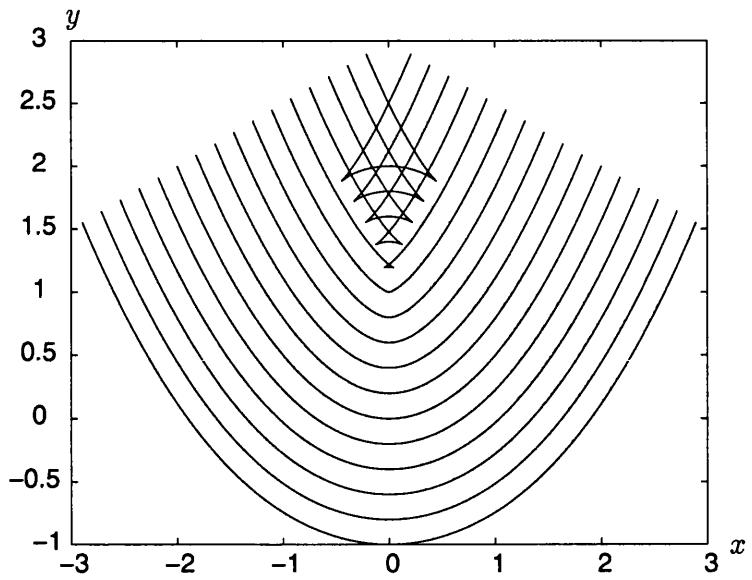

Figure 3-9: Propagation of a parabolic reference curve Γ_0 showing the formation of the swallow-tail singularity.

Note that the curvature $\kappa(s,t)$ becomes infinite at the first value of t, which occurs on the normal through the point on the reference curve with the *smallest radius of curvature*. If $\kappa(s,0)$ is *negative* then the curve Γ_t has a well defined normal for all positive t. However, if $\kappa(s,0)$ is *positive*, then there will be a first value of

$$t = \mathcal{T} = \min(1/\kappa(s,0)),$$

at which the normal vector first vanishes. The value of $\mathcal{T}$ gives the maximum width of the layers before a singularity occurs. For $t > \mathcal{T}$ the curve Γ_t is multi-valued and has a swallow-tail singularity, with points of infinite curvature. This situation is illustrated in figure 3-9 where we take a parabola to be the reference curve.

As the layers are assumed to be incompressible in their local tangent direction, it follows that the arc length of each individual layer must remain constant. This imposes a constraint on the allowable deformations. To consider the effects of this constraint we calculate the arc length. Suppose that $\mathrm{d}l_t$ is the infinitesimal arc length on the curve Γ_t. If the total arc length of Γ_t is l_t, then

$$l_t = \int_{\Gamma_t} \mathrm{d}l_t = \int_{\Gamma_t} \frac{\mathrm{d}l_t}{\mathrm{d}s}\,\mathrm{d}s.$$

Now

$$\frac{\mathrm{d}l_t}{\mathrm{d}s} = \sqrt{x_s^2(s,t) + y_s^2(s,t)} = \sqrt{(1 - t\kappa(s,0))^2}\frac{\mathrm{d}l_0}{\mathrm{d}s} = |1 - t\kappa(s,0)|\frac{\mathrm{d}l_0}{\mathrm{d}s}.$$

Two cases then arise, either $t < \mathcal{T}$ in which case $1 - t\kappa(s,0)$ has a constant sign over the length of Γ_t; or it changes sign at certain points along the curve. If $\theta(s,t)$ is the angle of the curve Γ_t at the point $(x(s,t), y(s,t))$, then $\tan(\theta) = \mathrm{d}y/\mathrm{d}x$ and

$$\kappa = \frac{\mathrm{d}\theta}{\mathrm{d}l} \tag{3.8}$$

Thus, if $t < \mathcal{T}$ we have

$$l_t = \int_{\Gamma_t} \frac{\mathrm{d}l_t}{\mathrm{d}s}\,\mathrm{d}s = \int_{\Gamma_0} (1 - t\kappa(s))\frac{\mathrm{d}l_0}{\mathrm{d}s}\,\mathrm{d}s = l_0 - t\int_{\Gamma_0} \frac{\mathrm{d}\theta_0}{\mathrm{d}s}\,\mathrm{d}s = l_0 - t\left[\theta(s,0)\right]_{s=0}^{s=1}.$$

We arrive at the result:

Theorem 1. *Whilst equation* (3.2) *holds and* $t < \mathcal{T}$ *total arc length of* Γ_t *is given by:*

$$l_t = l_0 - t[\theta(s,0)]_{s=0}^{s=1}. \tag{3.9}$$

Corollary 1. *If* $t < \mathcal{T}$ *and* $[\theta(s,0)]_{s=0}^{s=1} = 0$, *the total arc length of each curve* Γ_t *remains constant.*

If $t > \mathcal{T}$ then the normal ceases to exist, and the direction of $\mathrm{d}l/\mathrm{d}s(t)$ changes sign at certain points so that $|1 - t\kappa(s,0)|$ changes from $1 - t\kappa(s,0)$ to $-1 + t\kappa(s,0)$. The above reasoning breaks down, and there is no guarantee that the total arc length is preserved.

3.3.3 Singularities

If $t > \mathcal{T}$ the curve Γ_t has a singularity resulting in a self-intersecting curve with infinite curvature. We now explore what happens as $t \to \mathcal{T}^-$. To study this

situation we consider what happens when a parabola is propagated forward at a constant speed. We take a reference curve Γ_0 defined for $s \in [0,1]$ by

$$x(s,0) = s - 1/2, \quad \text{and} \quad y(s,0) = \frac{K(s-1/2)^2}{2}$$

where K is a constant. If we set $S = (s - 1/2)$ then the unit normal $\mathbf{n}$ is given by

$$\mathbf{n} = \left(-\frac{KS}{\sqrt{1+K^2S^2}}, \frac{1}{\sqrt{1+K^2S^2}} \right)$$

and hence

$$(x(S,t), y(S,t)) = \left(S - \frac{KSt}{\sqrt{1+K^2S^2}}, \frac{KS^2}{2} + \frac{t}{\sqrt{1+K^2S^2}} \right).$$

A plot of the resulting set of curves was given in figure 3-9, where the self-intersecting nature of the curve is clear. The radius of curvature of the reference curve Γ_0 takes its smallest value of $1/K$ when $S = 0$ and we deduce that the singularity occurs when $t = \mathcal{T} = 1/K$. If $t > 1/K$ then the curve self-intersects when

$$(x(S,t), y(S,t)) = (x(-S,t), y(-S,t)) = (0, Y),$$

which occurs when

$$S = \sqrt{t^2 - 1/K^2} \quad \text{and} \quad Y = \frac{Kt^2}{2} + \frac{1}{2K}.$$

At the point of self-intersection the curve Γ_t has a locally V-shaped form. The gradient of the curve is given by $\mathrm{d}y/\,\mathrm{d}x = y_s/x_s$. Substituting $K^2S^2 = K^2t^2 - 1$ into the expressions for y_s and x_s we have that at the point of self-intersection

$$\frac{\mathrm{d}y}{\mathrm{d}x} = \pm K\sqrt{t^2 - 1/K^2}, \quad \text{if} \quad t > 1/K. \tag{3.10}$$

To examine the form of the curves as we approach the singular point we set

$t = 1/K - \delta$ and let S and $\delta > 0$ be small. To leading order we then have

$$\begin{aligned} x &= \delta K S + \frac{K^2 S^3}{2} + \mathcal{O}(S^5, \delta S^3) \quad \text{and} \\ y &= \frac{1}{K} - \delta + \frac{\delta K^2 S^2}{2} + \frac{3K^3}{8} S^4 + \mathcal{O}(S^6, \delta S^4). \end{aligned}$$

It follows that

$$\begin{aligned} y &= \frac{1}{K} + \frac{3K^{1/3}}{8}(2x)^{4/3} + \mathcal{O}(x^2) \quad \text{if} \quad \delta = 0, \\ y &= \frac{1}{K} - \delta + \frac{x^2}{2\delta} + \mathcal{O}(x^4) \quad \text{if} \quad 0 < \delta \ll 1. \end{aligned}$$

It follows immediately that when $x = 0$ we have

$$\frac{\mathrm{d}^2 y}{\mathrm{d}x^2} = \frac{1}{\delta} \quad \text{if} \quad 0 < \delta \ll 1.$$

This calculation is especially significant in the context of the calculation of the mechanics of buckling that we will consider in chapter 4. In particular, the bending energy associated with a buckled layer is proportional to the integral of the square of the second derivative, which we show in chapter 4 approaches infinity as $\delta \to 0$. As a consequence, the bending energy is a strongly nonlinear function of the displacement of the reference layer, and this has a significant effect on the resulting buckling profiles.

It is difficult to know exactly what happens to the rock layers physically as a singularity is approached and possibly transgressed. However, the assumed geometry forces this to happen and a comparison of figure 1-1 and figure 3-9 shows clear similarities. What is clear, however, is that the rocks do not pass through themselves. Indeed, what seems to occur is that either a secondary fold forms (see figure 3-3) or the rock layers of figure 2-8 (shown as a dashed line) take the geometry of the *non self-intersecting* part of the curve. Hence, to fully realise the possible geometries that a rock layer can have, we are motivated to look at a construction method which is different from the Lagrangian approach (which leads to the self-intersecting curves) and which allows us naturally to resolve, and pass through, the singularity, allowing a natural description of the

non self-intersecting part of the curves when $t > 1$ where appropriate. As we saw in chapter 2, such a procedure is given by the level set method, which relies on an Eulerian representation of the set of layered surfaces and a weak formulation of the equation of propagation of the layers. The *entropy condition* overcomes the problems with self-intersection by 'deleting' the self-intersecting part of the curve, which causes the loss in length.

3.4 The Eulerian Representation of multilayer folding

3.4.1 The level set method

In contrast to the previous description of layer propagation using Lagrangian coordinates, the Eulerian representation aims to find the (x, y) equation of the curves $\Gamma_{i\Delta t}$ in particular thinking of t as a continuous variable and looking at the differential equations governing the propagation of Γ as a function of t.

Accordingly, for a general t we set

$$\Gamma_t = \{(x, y) : y = w(x, t)\}.$$

We suppose further that each set Γ_t occupies a part of a bounded, rectangular domain Ω in $\mathbb{R}^2$ extending from the left boundary of Ω to the right and separating Ω into two regions, Ω^-, the region *'inside'* the boundary and the region above the interface, Ω^+, the region *'outside'* the boundary.

We next assume that Γ_t is a *level set* of a higher dimensional function $\phi(x, y, t)$ so that

$$y = w(x, t) \quad \text{iff} \quad \phi(x, y, t) = 0.$$

The evolution of the function ϕ with t can then be linked to the propagation of the interfaces Γ_t. This is the essence of the level set method (LSM). References to

the level set method, and in particular its application to the calculation of various free surface problems in fluid mechanics, include Osher and Sethian (1988), Osher and Fedkiw (2003) and Sethian (1999).

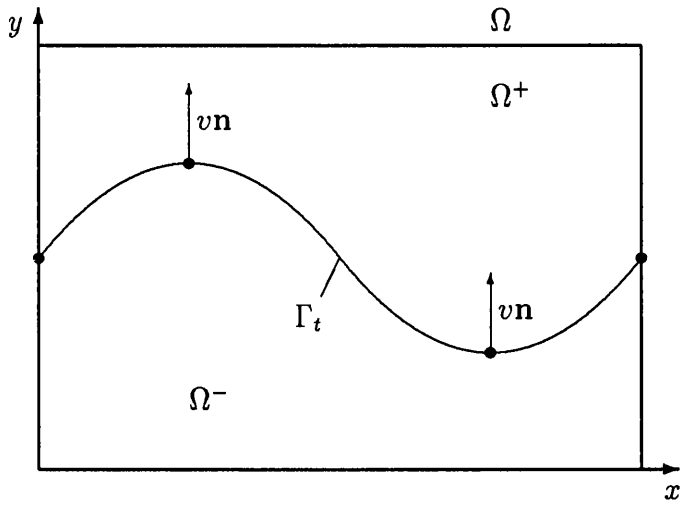

Figure 3-10: The domain Ω.

To apply the level set method, we first find ϕ by solving an appropriate partial differential equation, and then determine its contours.

As an example of the use of the LSM, consider the function

$$\phi(x, y, t) = x^2 + y^2 - (1 + t)^2.$$

Then for fixed t the (x, y) curve satisfying the level set equation

$$\Gamma_t = \{(x, y) : \phi(x, y, t) = 0\}$$

is a circle of radius $1 + t$. The family of such level sets precisely describes the evolution of an initial circle propagating at a constant speed $v = 1$ in a direction normal to each curve. Figure 3-11 shows how the function ϕ above evolves with t.

We now return to the general case and derive the partial differential equation satisfied by the function $\phi(x, y, t)$. Following the formulation of Sethian (1999), let $\mathbf{x}(t) = (x(t), y(t))$ be a point on the curve $\Gamma_t \equiv \{(x, y) : y = w(x, t)\}$. Starting

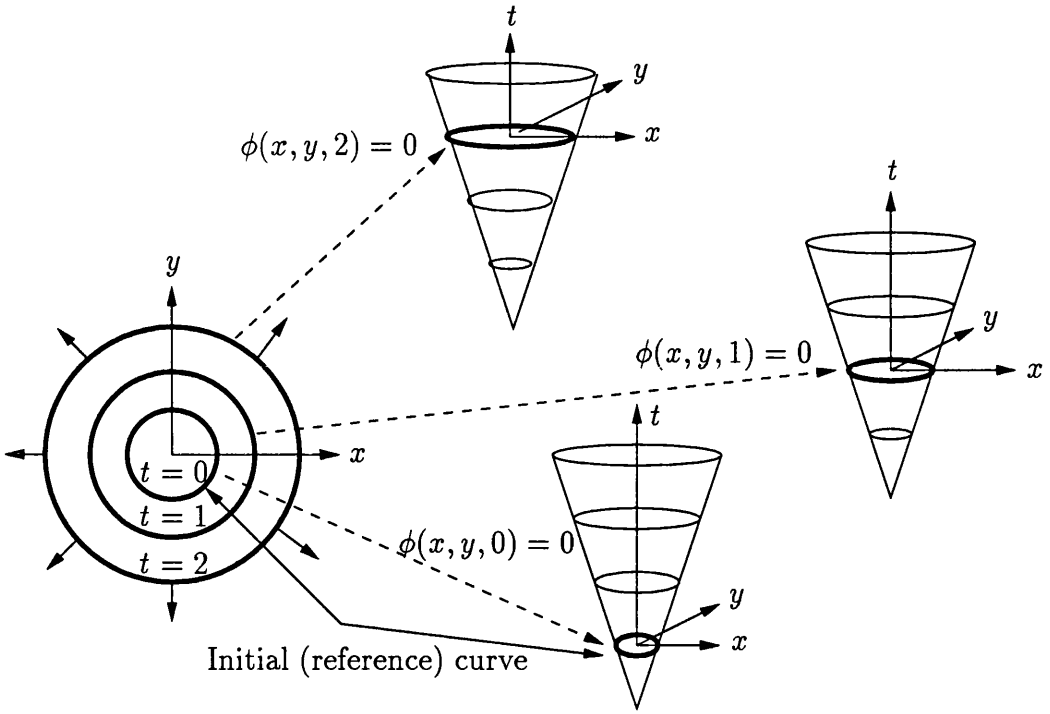

Figure 3-11: The propagation of a circle in the normal direction by considering a higher dimensional function $\phi(x,y,t)$. (After Sethian (1999))

from the identity $\phi(x,y,t)=0$, it follows from the chain rule that,

$$\phi_t + \nabla\phi(\mathbf{x}(t),t)\cdot\mathbf{x}'(t) = 0, \tag{3.11}$$

where $\nabla\phi$ is defined to be (ϕ_x,ϕ_y) and $\mathbf{x}'(t)$ is defined to be (x_t,y_t). If $v(x,y)$ is the speed in the normal direction, then $\mathbf{x}'(t)\cdot\mathbf{n} = v$, where the unit normal $\mathbf{n}$ is given by $\mathbf{n} = \nabla\phi/|\nabla\phi|$. It follows that ϕ satisfies the following hyperbolic partial differential equation of Hamilton-Jacobi type (the *level set equation*).

$$\phi_t + v|\nabla\phi| = 0. \tag{3.12}$$

Solving this equation for $\phi(x,y,t)$ together with a prescribed initial function $\phi(x,y,0)$ determines the curves $\Gamma_t = \{(x,y)\,|\,\phi(x,y,t)=0\}$ and the exterior and interior regions are respectively:

$$\begin{aligned}\Omega_t^+ &= \{(x,y)\,|\,\phi(x,y,t)>0\},\\ \Omega_t^- &= \{(x,y)\,|\,\phi(x,y,t)<0\}.\end{aligned} \tag{3.13}$$

Definition 9. *Signed distance function*

Often the *signed distance function* is a good choice for the level set function ϕ. A *distance function* $d(\mathbf{x})$ of a point $\mathbf{x} \in \Omega$ is defined as

$$d(\mathbf{x}) = \min(|\mathbf{x} - \mathbf{x}_I|) \quad \text{for all} \quad \mathbf{x}_I \in \Gamma_0 \tag{3.14}$$

where Γ_0 is the interface, implying that points on the boundary have distance $d(\mathbf{x_I}) = 0$. Signed distance functions have the additional property that points 'inside' the interface are assigned negative distances and that points 'outside' are assigned positive distances. A signed distance function $\phi(\mathbf{x})$ is then defined as

$$\phi(\mathbf{x}) = \begin{cases} -d(\mathbf{x}) & \text{if } \mathbf{x} \in \Omega^- \\ d(\mathbf{x}) & \text{otherwise.} \end{cases} \tag{3.15}$$

In the level set formulation, the condition for *parallel folding* is that the speed function, $v(x, y)$ should be *constant.* However, we note that it would be straightforward to include other forms for the function v to allow, for example, for situations in which the rocks can compress laterally (Wadee et al., 2004). Other examples of speed functions include the cases where v depends on the curvature κ (which arises in flame front propagation (Rhee et al., 1995)) and where it depends on $|\nabla\phi|$ (which arises in electro-machining). With this formulation the important properties of the geometry of the layers of rock, such as the normal to a layer $\mathbf{n}$ or the curvature κ and the angle between the tangent and the horizontal θ can be easily calculated in terms of ϕ (see lemma 1).

3.4.2 Numerical implementation

Initialisation

Initialisation is the process of finding the initial level set function $\phi(x, y, t = 0)$. To apply the level set method to the parallel folding photograph (figure 2-8) the

following steps were taken:

1. Fit a cubic spline through a central layer with the MATLAB routine `ginput` to trace and record a set of points on the photograph. The routine `spline` was then used to fit a cubic spline though these points.

2. Set up grid by dividing the width and height of the photograph into a set of regularly spaced points.

3. Extend spline to the edge of the grid by checking end points to calculate where on the grid boundary the linearly extrapolated spline crosses. This defines the reference curve Γ_0.

4. Calculate distance function by visiting every grid point and finding the distance to the reference curve.

5. Calculate signed distance function with an application of the MATLAB routine `inpolygon` to the following points: the last point on the reference curve, every corner of the grid encountered as we travel in a clockwise direction around the grid boundary from the last point on the reference curve until the first point on the reference curve is reached and finally every point on the reference curve.

Update

To update the function ϕ and hence to propagate the interface using the level set method we calculate the whole function ϕ using a time-stepping method. Assuming that we have a good approximation to $\phi(x, y, t)$ for some time $t = i\Delta t$ we then use a numerical method to find an approximation to the solution ϕ of (3.12) for the time level $t = (i + 1)\Delta t$. A second numerical method is then used to locate the zero contour of $\phi(x, y, (i + 1)\Delta t)$ to find an approximation to $\Gamma_{(i+1)\Delta t}$. The algorithm we use for implementing this strategy is as described in Osher and Sethian (1988). To implement this we consider an approximation $\Phi^i_{j,k}$ to the function $\phi(x, y, t)$ at the point $(x, y, t) = (jh, kh, i\Delta t)$. Here h and

Δt are small and constant. An explicit discretisation of (3.12) for a constant $\mathbf{v}$ takes the form

$$\Phi_{k,j}^{i+1} = \Phi_{k,j}^{i} - \Delta t \left[\max(v,0)\nabla^{+} + \min(v,0)\nabla^{-}\right] \tag{3.16}$$

where

$$\begin{aligned} \nabla^{+} &= [\max(D_{k,j}^{-x},0)^2 + \min(D_{k,j}^{+x},0)^2 + \\ &\quad \max(D_{k,j}^{-y},0)^2 + \min(D_{k,j}^{+y},0)^2]^{1/2} \end{aligned} \tag{3.17}$$

$$\begin{aligned} \nabla^{-} &= [\max(D_{k,j}^{+x},0)^2 + \min(D_{k,j}^{-x},0)^2 + \\ &\quad \max(D_{k,j}^{+y},0)^2 + \min(D_{k,j}^{-y},0)^2]^{1/2}. \end{aligned} \tag{3.18}$$

In the above the terms $D_{j,k}^{+x}$ are a shorthand for the difference operators as seen earlier in section 2.4.1. Local errors in this scheme are of $\mathcal{O}(h, \Delta t)$. The level set method as implemented is stable provided that the CFL condition is met (Courant et al., 1928). In the rock layer propagation example the CFL condition often dictated that we chose a time step that was smaller than the rock layer thickness. To get a close visual match we plotted every m layers, so that $m\Delta t$ was approximately equal to the layer thickness.

Measurement

The position of the zero level set is only defined implicitly via the function ϕ. The MATLAB `contour` routine can be used to plot the zero level set and the routine `contourc` can be used to find points along this curve.

Errors

There are three sources of error when numerically solving the level set equation (Sethian, 1999). These are directly linked to the three steps outlined above. *Initialisation error* which is error obtained when finding the signed distance

function on a discrete mesh from an initial curve, the *Update error* which is error in finding an approximation to $\phi(x, y, (n+1)\Delta t)$ given $\phi(x, y, n\Delta t)$ and the *Measurement error* which is the error associated with finding the position of the zero level set. Note that in order to calculate Φ^{n+1} we must calculate Φ^n at *all* spatial points, not just those close to the interface (see section 2.4.5).

3.4.3 Singularities found in rock folding

We conclude this section by looking at some examples in which we explore the applications and limitations of the LSM for calculating the geometry of certain problems given a known reference layer Γ_0.

Examples with reentrant corners

Example 1 As a first, quantitative calculation, which has a close link to a rock folding problem, which we will consider further in chapter 4, we consider a reference curve given by

$$\Gamma_0 = \{(x, y) : x = s, y = \cos(2\pi s)\}, \quad 0 \leq s \leq 1.$$

To apply the level set method we take an initial function

$$\phi(x, y, 0) = y - \cos(2\pi x).$$

This is not a *signed distance function*, meaning that gradients are steeper and therefore harder to approximate accurately numerically, but it does give an accurate and easy to implement initial zero level set. We now compute the resulting layers Γ_t and compare these with the solutions predicted by the Lagrangian formulation. Using this, the exact parametric equation of the layer at the time t is given by

$$x = s + \frac{2\pi \sin(2\pi s)t}{\sqrt{1 + 4\pi^2 \sin^2(2\pi s)}}, \quad y = \cos(2\pi s) + \frac{t}{\sqrt{1 + 4\pi^2 \sin^2(2\pi s)}}.$$

The curvature of the reference curve takes its maximum value of $4\pi^2$ at the point $s = 1/2$ and hence a singularity occurs when $t = 1/4\pi^2$, $x = 1/2$, $y = -1+1/4\pi^2$. A close-up of the singularity of the exact (multi-valued) solution arising from the Lagrangian description is plotted in figure 3-12(a).

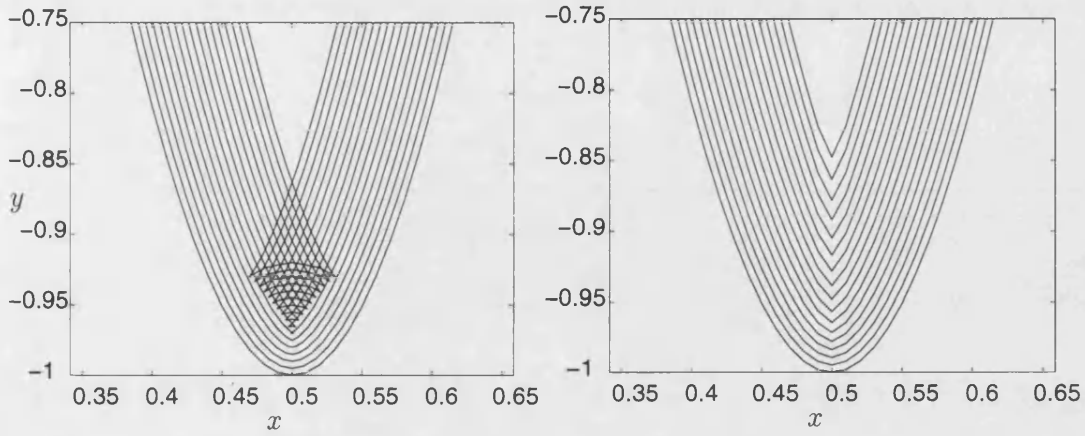

Figure 3-12: Close-up of a propagation of a cosine wave using (a) using the Lagrangian method, showing the self-intersecting curves (b) using the level set method, showing the local V-shaped nature of the curves.

We now compare the Lagrangian solution with that derived by using the level set method. A calculation using the method for $h = 0.01$ and $\Delta t = 0.005$ is presented in figure 3-12(b) (here the corresponding close-up of the singularity is shown).

Observe, that in contrast to the Lagrangian description, the level set method has deleted the self-intersecting part of the curves, and the resulting curves have an apparent gradient discontinuity at the centre. The local V-shaped nature of these curves is very similar to that of the layers in the chevron folding pattern illustrated in figure 3-1. Indeed, if we take Γ_0 to be the V-shaped curve

$$\Gamma_0 = \{(x, y) : x = s, y = |s - 1/2|\},$$

then the resulting calculation of the layers Γ_t using the level set method is given in figure 3-13(a) and a close-up in figure 3-13(b). We see that the level set method has successfully coped with the gradient singularity, reproducing the self-replicating feature of parallel folding in this case where all layers Γ_t have exactly the same shape and the same arc length. We note that in figure 3-13(b)

the corner is slightly smoothed due to the error. This effect can be reduced by refining the mesh.

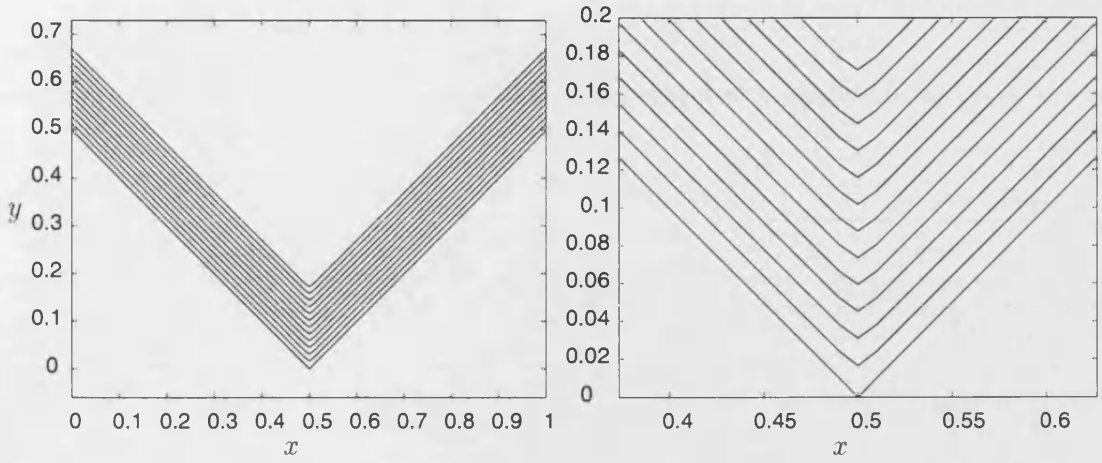

Figure 3-13: (a) Propagation of a V-shaped curve with the level set method (b) Close-up of the propagation of the V-shaped using the level set method, showing the local error at the singularity

As a further measure of the accuracy of the calculation of the propagating cosine reference curve $\Gamma_0 = \{(x, y) : x = s, y = \cos(2\pi s)\}$ $0 \ll s \ll 1$, we plot the total arc length of the resulting curves. The choice of reference curve ensures that $[\theta_t] = 0$. Hence, from theorem 1, the total arc length of the curve Γ_t stays constant up to the point of singularity formation when $t = 1/4\pi^2$. For larger values of t the curve self-intersects and the total arc length of the curve, omitting the self-intersecting part, decreases until a steady state is reached. This arc length can be calculated exactly. If $s = s^*$ is the parameter value on the reference curve for which the normal intersects with the line $x = 1/2$ then

$$t = \frac{(1/2 - s^*)\sqrt{1 + 4\pi^2 \sin^2(2\pi s^*)}}{2\pi \sin(2\pi s^*)}.$$

As the normal to the reference curve is also normal to Γ_t the angle θ is given by $\theta = \tan^{-1}(-2\pi \sin 2\pi s)$. The arc length $l(t)$ is then given by theorem 1 as

$$l(t) = 2\int_{s^*}^{1} \sqrt{1 + 4\pi^2 \sin^2 2\pi s}\, \mathrm{d}s + 2t\theta. \tag{3.19}$$

This is a standard elliptic integral and can be evaluated analytically. Simi-

larly, the arc length of Γ_t can be found numerically by applying quadrature to the sets found by the LSM. The two values are compared in figure 3-14.

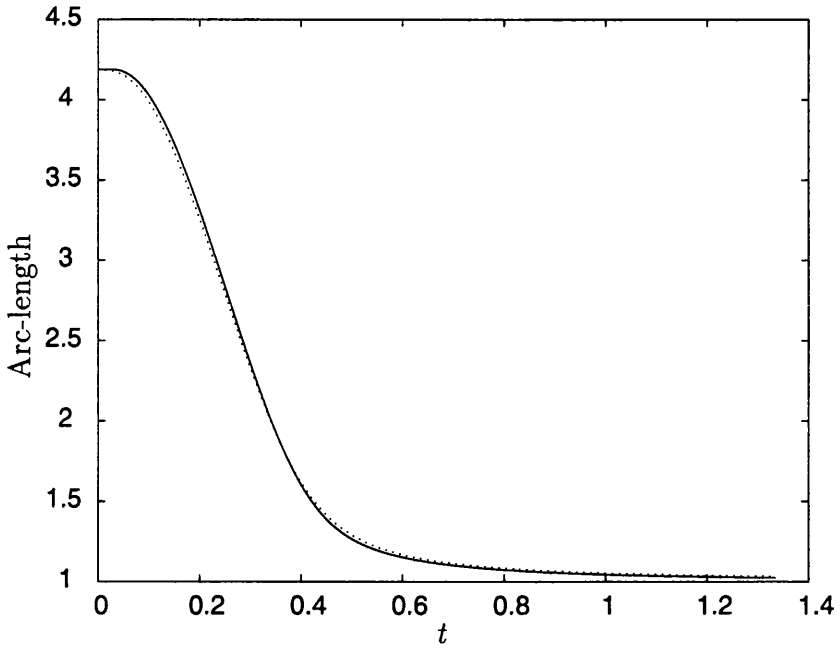

Figure 3-14: Change in arc length with t showing the level set method estimate (dotted) and the quadrature estimate (solid)

Example 2. As a second example of an application of the LSM we look at a physical problem and reconsider the calculation illustrated in figure 2-8. A reference layer Γ_0 was obtained directly from the photograph by sampling the photographed curve at regular points along roughly the middle layer and then fitting a spline through the resulting data. The resulting layers propagated (through the singularity) by solving the level set equation (3.12). Here we took $h \approx 5$ and $\Delta t \approx 2.5$, and chose to plot the zero level set at every 15 time steps (there are 640 pixels in the horizontal direction). The qualitative agreement between the calculations and the observed geometry appears very good, including apparently the representation of the singularity and of the rock layers formed beyond the singularity.

Examples with salient corners

The viscosity solution does not always agree with the observed patterns of folded rock. In the chevron folding examples of figures 3-1 and 3-6 the rock layers fold in a zig-zag and we see both reentrant and salient corners, each of which has a gradient discontinuity. Now consider a reference curve Γ_0 given by an upside-down 'V' with interior angle 2α and propagate this in the direction of increasing t (see figure 3-15). Instead of propagating such a salient corner without change, the entropy condition that is obeyed by the LSM picks out a rarefaction fan of solutions in which the curves Γ_t lose the sharp V-shape and have a circular arc at the peak with arc length $2t\alpha$, consistent with theorem 1 .

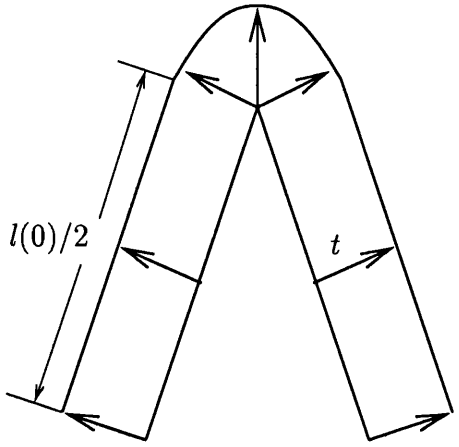

Figure 3-15: A Salient Corner obeys Huygens' Principle, forming a Rarefaction fan.

The LSM has not in this case given a solution consistent with that observed in practice (compare with figure 3-6). To overcome this difficulty with the level set formulation we can follow the procedure outlined in Russo and Smereka (2000) (see section 2.4.6).

Chapter 4

The mechanics of folding

4.1 Introduction

Having determined a procedure for finding the overall geometry of the layered system from a single reference layer Γ_0 we now examine how the form of Γ_0 itself can be calculated by using properties of the function ϕ. This chapter shows how we can incorporate mechanical features into the geometrical description given by the level set method, allowing us to find the shape of the reference curve. The profile of the compressed layered material is determined by the interplay of several mechanisms namely the effect of the applied force, the bending properties of the layers, the work done into the external medium, the effects of the geometry constraints and the frictional forces acting to oppose sliding between the layers. These are best described by calculating the total energy V which is a combination of the bending energy, frictional energy and the work done by the external forces. Crucially, this total energy, V can be calculated in terms of the level set function ϕ, depending on Γ_0. We can then find the profile of the material by finding stationary points of V with respect to (appropriate) variations in Γ_0.

4.2 Calculating the total energy in terms of ϕ

We consider the geometry illustrated in figure 3-7 in which we assume that an initially undeformed multilayer material enclosed within a foundation material is compressed and buckled by an external load. This load is resisted by the stiffness of the layers, the frictional force as the layers slide in contact and the resistance of the matrix in which the layers are embedded.

Recall the two layer model of Budd et al. (2003) presented in section 1.6.2, where the total potential energy was given by

$$V = U_B + U_F - P\mathcal{E} + \chi U_\mu \tag{4.1}$$

and the expressions have the form

$$U_B = EI \int_0^L \left(\frac{\ddot{w}^2}{1 - \dot{w}^2} \right) \mathrm{d}l, \tag{4.2}$$

$$U_F = \frac{1}{2} k \int_0^L w^2 \, \mathrm{d}l, \tag{4.3}$$

$$P\mathcal{E} = P \int_0^L \left(1 - \sqrt{1 - \dot{w}^2} \right) \mathrm{d}l, \tag{4.4}$$

$$U_\mu = \mu q \Delta t \int_0^L \left| \sin^{-1}(\dot{w}) \right| \mathrm{d}l, \tag{4.5}$$

where dots denote differentiation with respect to l.

To extend this two-layer model to a multilayer formulation we assume as before that there are $2n + 1$ layers each of thickness Δt and length L and that $w_{i\Delta t}(x)$, $i = -n \ldots n$ is the vertical deflection of the interface between two successive layers. In the experiments conducted, each of the layers is compressed by the load by *the same horizontal amount* $\mathcal{E}$. The simplest way to ensure this occurs with the level set formulation is to set $\dot{w}(0) = \dot{w}(L) = 0$.

The total energy of the multilayer material can then be expressed as

$$U_B = \frac{Eb\Delta t^3}{24} \sum_{i=-n}^{n} \int_0^L \frac{\ddot{w}_i^2}{1-\dot{w}_i^2} \, \mathrm{d}l, \tag{4.6}$$

$$U_F = \frac{1}{2} k \int_0^L \left(w_n^2 + w_{-n}^2\right) \, \mathrm{d}l \tag{4.7}$$

$$P\mathcal{E} = P \int_0^L \left(1 - \sqrt{1-\dot{w}_0^2}\right) \, \mathrm{d}l \tag{4.8}$$

$$U_\mu = \mu q \Delta t \sum_{i=-n}^{n-1} \int_0^L \left|\sin^{-1}(\dot{w}_i)\right| \, \mathrm{d}l. \tag{4.9}$$

where b is the breadth of the layer. It is straightforward to derive these expressions by following the derivations of the two-layer formulation. We make the following, clarifying remarks:

1. Each individual layer's bending energy makes a contribution to the bending energy. It is very important to observe that the bending energy has a component which varies as the integral of $\ddot{w}_i^2$, implying that all layers do not make an equal contribution to the bending energy. As we have already seen, this term becomes unbounded as we approach a singularity, and the expression (4.6) is not defined at this point. For the present we will assume that no singularity has formed so that this issue does not arise, and will return to consider the singular case.

2. In this expression the external foundation is assumed to obey a Winkler force law, with a linear foundation stiffness k. It is the shape of the top and bottom layers as they push into the foundation that determine the energy stored. Therefore a method that finds the geometry of every layer would be expected to model this term more accurately than a method that has information only of the deflection of the central layer.

3. The expression for the work done by the load remains unchanged from the two-layer case because of the assumption that every layer undergoes the same horizontal end-shortening.

4. Friction is only considered to act between layers of the multilayer; friction

between the foundation and the top and bottom layers is neglected (as is any shearing of the foundation).

We can now combine the geometric description of the layers with the mechanical description in the previous subsection by expressing V in terms of the single function ϕ. Before we reformulate the energy contribution in terms of the level set function ϕ, it is useful to state a lemma that expresses various terms which arise in the energy expression in terms of ϕ.

Lemma 1. *(a) The derivatives of x and y with respect to l are as follows:*

$$\frac{\partial x}{\partial l} = \dot{x} = \frac{\phi_y}{|\nabla \phi|}, \quad \frac{\partial y}{\partial l} = \dot{y} = -\frac{\phi_x}{|\nabla \phi|} \tag{4.10}$$

(b) The curvature κ can be expressed as

$$\kappa = \nabla \cdot \frac{\nabla \phi}{|\nabla \phi|} = \frac{\phi_{xx}\phi_y^2 - 2\phi_y \phi_x \phi_{xy} + \phi_{yy}\phi_x^2}{\left(\phi_x^2 + \phi_y^2\right)^{\frac{3}{2}}}. \tag{4.11}$$

Proof. (a) Let $y = w(x)$ be such that $\phi(x, w(x), t) = 0$. Then,

$$\frac{\mathrm{d}y}{\mathrm{d}x} = -\frac{\phi_x}{\phi_y}. \tag{4.12}$$

Hence

$$\begin{aligned} \dot{x}^2 &= \frac{1}{1+\left[\frac{\mathrm{d}y}{\mathrm{d}x}\right]^2} = \frac{1}{1+\frac{\phi_x^2}{\phi_y^2}} \quad [\text{by}(4.12)] \\ &= \frac{\phi_y^2}{\phi_x^2+\phi_y^2} \\ \Rightarrow \dot{x} &= \frac{\phi_y}{\left(\phi_x^2+\phi_y^2\right)^{\frac{1}{2}}} = \frac{\phi_y}{|\nabla\phi|}, \end{aligned}$$

and similarly

$$\dot{y} = -\frac{\phi_x}{\left(\phi_x^2+\phi_y^2\right)^{\frac{1}{2}}} = -\frac{\phi_x}{|\nabla\phi|}.$$

(b) Now apply the chain rule again to find the second derivative,

$$\frac{\mathrm{d}^2y}{\mathrm{d}x^2} = \frac{-\phi_y^2\phi_{xx}+2\phi_x\phi_y\phi_{xy}-\phi_x^2\phi_{yy}}{\phi_y^3}. \tag{4.13}$$

The result follows by substitution into equation (1.16). □

We now use these expressions to reformulate the various components of the energy contributions (equations (4.6) to (4.9)) in terms $\phi(x,y,t)$ where, to simplify the expression we set

$$\phi^i = \phi(x,y,i\Delta t) \quad \text{where} \quad \phi^i(x, w_{i\Delta t}(x)).$$

Theorem 2. *In the case of a* nonsingular *deformation the energy terms are given by*

$$U_B = \frac{Eb\Delta t^3}{24}\sum_{i=-n}^{n}\iint_\Omega \delta(\phi^i)\left(\nabla\cdot\frac{\nabla\phi^i}{|\nabla\phi^i|}\right)^2|\nabla\phi^i|\,\mathrm{d}y\,\mathrm{d}x, \tag{4.14}$$

$$U_F = \frac{1}{2}k\iint_\Omega \left[\delta(\phi^n)|\nabla\phi^n|y_n^2+\delta(\phi^{-n})|\nabla\phi^{-n}|y_{-n}^2\right]\,\mathrm{d}y\,\mathrm{d}x, \tag{4.15}$$

$$P\mathcal{E} = P\iint_\Omega \delta(\phi^0)\left(|\nabla\phi^0|+\phi_y^0\right)\,\mathrm{d}y\,\mathrm{d}x, \tag{4.16}$$

$$U_\mu = \mu q\Delta t\sum_{i=-n}^{n-1}\iint_\Omega \delta(\phi^i)\left|\sin^{-1}\left(\frac{\phi_x^i}{|\nabla\phi^i|}\right)\right|\,|\nabla\phi_y^i|\,\mathrm{d}y\,\mathrm{d}x. \tag{4.17}$$

The delta function is included in equations (4.14)–(4.17) so that it is the position of the *zero level set*, $\Gamma_{i\Delta t}$, that makes the contributions to the energy and not the part of ϕ defined over the rest of Ω. To determine V from this expression the delta function would have to be numerically approximated and this could potentially cause the evaluation of the integrals to be inaccurate. However, having located the zero level set of ϕ using the contour plotting algorithm and given the form of the function $\phi^i(x,y)$, a more direct approach can be used. To do this we formulate the equations over each zero level set, $\Gamma_{i\Delta t}$ to give the following result

Lemma 2. *Integrating over each zero level set we have*

$$U_B = \frac{Eb\Delta t^3}{24} \sum_{i=-n}^{n} \int_{\Gamma_{i\Delta t}} \left(\nabla \cdot \frac{\nabla \phi^i}{|\nabla \phi^i|} \right)^2 \frac{|\nabla \phi^i|}{\phi^i_y} \, \mathrm{d}x \tag{4.18}$$

$$U_F = \frac{1}{2} k \left(\int_{\Gamma_{n\Delta t}} y_n^2 \frac{|\nabla \phi^n|}{\phi^n_y} \, \mathrm{d}x + \int_{\Gamma_{-n\Delta t}} y_{-n}^2 \frac{|\nabla \phi^{-n}|}{\phi^{-n}_y} \mathrm{d}x \right) \tag{4.19}$$

$$P\mathcal{E} = P \int_{\Gamma_0} \left(1 + \left(\frac{\phi^0_y}{|\nabla \phi^0|} \right) \right) \frac{|\nabla \phi^0|}{\phi^0_y} \, \mathrm{d}x \tag{4.20}$$

$$U_\mu = \mu q \Delta t \sum_{i=-n}^{n-1} \int_{\Gamma_{i\Delta t}} \left| \sin^{-1} \left(\frac{\phi^i_x}{|\nabla \phi^i|} \right) \right| \frac{|\nabla \phi^i|}{\phi^i_y} \, \mathrm{d}x \tag{4.21}$$

Proof. We prove both theorem 2 and lemma 2 by considering each of the contributions to the energy in turn.

The bending energy The total bending energy of the multilayer system is given by equation (4.6). Now, recall the expression for the curvature, κ, given by equation (1.16),

$$\kappa = \ddot{w} \left(1 - \dot{w}^2 \right)^{-\frac{1}{2}} .$$

Therefore, if κ_i is the curvature on the curve $\Gamma_{i\Delta t}$ then equation (4.6) can be written as

$$U_B = \frac{Eb\Delta t^3}{24} \sum_{i=-n}^{n} \int_0^L \kappa_i^2 \, \mathrm{d}l. \tag{4.22}$$

Using the expression (4.11) it follows that the bending energy is given by the expression

$$\begin{aligned} U_B &= \frac{Eb\Delta t^3}{24} \sum_{i=-n}^{n} \int_0^L \left(\nabla \cdot \frac{\nabla \phi^i}{|\nabla \phi^i|} \right)^2 \mathrm{d}l \\ &= \frac{Eb\Delta t^3}{24} \sum_{i=-n}^{n} \int_{\Gamma_{i\Delta t}} \left(\nabla \cdot \frac{\nabla \phi^i}{|\nabla \phi^i|} \right)^2 \frac{|\nabla \phi^i|}{\phi_y^i} \mathrm{d}x. \end{aligned}$$

The foundation energy By definition the vertical displacement w is the same as y such that $\phi(x, y, t) = 0$. So that

$$\frac{1}{2}k \int_0^L (w_n^2 + w_{-n}^2) \, \mathrm{d}l = \frac{1}{2}k \left(\int_{\Gamma_{-n\Delta t}} y_n^2 \frac{|\nabla \phi^{-n}|}{\phi_y^{-n}} \mathrm{d}x + \int_{\Gamma_{n\Delta t}} y_{-n}^2 \frac{|\nabla \phi^n|}{\phi_y^n} \mathrm{d}x \right). \tag{4.23}$$

The work done by the load We have assumed that each layer undergoes the same end-shortening under the axial load P and therefore the work done by the load is the same for one layer as for multiple layers. We arbitrarily choose to measure the end-shortening of the reference layer, $i = 0$

$$\begin{aligned} P\mathcal{E} &= P \int_0^L \left(1 - \sqrt{1 - \dot{w}_0^2} \right) \mathrm{d}l = P \int_0^L (1 - x_l^0) \, \mathrm{d}l \\ &= P \int_0^L \left(1 + \left(\frac{\phi_y^0}{|\nabla \phi^0|} \right) \right) \mathrm{d}l = P \int_{\Gamma_0} \left(1 + \left(\frac{\phi_y^0}{|\nabla \phi^0|} \right) \right) \frac{|\nabla \phi^0|}{\phi_y^0} \mathrm{d}x. \end{aligned}$$

The work done against friction If we substitute (4.10) into (4.9) we obtain

the expression

$$\begin{aligned} U_\mu &= \mu q \Delta t \sum_{i=-n}^{n-1} \int_0^L \left| \sin^{-1}\left(-\frac{\phi_x^i}{|\nabla \phi^i|} \right) \right| \mathrm{d}l \\ &= \mu q \Delta t \sum_{i=-n}^{n-1} \int_{\Gamma_{i\Delta t}} \left| \sin^{-1}\left(\frac{\phi_x^i}{|\nabla \phi^i|} \right) \right| \frac{|\nabla \phi^i|}{\phi_y^i} \mathrm{d}x. \end{aligned}$$

□

4.2.1 The energy close to a singularity

To refine this calculation we briefly consider the form taken by the bending energy close to a singularity where the curve Γ_t develops an infinite curvature when $t = \mathcal{T}$. In this calculation we will assume that the reference layer Γ_0 is a smooth curve, with maximum curvature of $K > 0$ occurring at a minimum point where it has a locally parabolic form. As $t \to \mathcal{T} = 1/K$ the maximum curvature of the curve Γ_t increases, and hence the bending energy also increases. To determine the asymptotic behaviour of the bending energy we will approximate Γ_0 locally by the parabola $y = Kx^2/2$, with $-1 < x < 1$. It then follows from the analysis presented in chapter 3 that if $t = 1/K - \delta$ with $\delta > 0$ small, then the maximum curvature $\hat{\kappa}_t$ of the folded layer is given by

$$\hat{\kappa} = \frac{1}{\delta}.$$

Similarly, if $t = 1/K$ then close to the point $x = 0$ the second derivative of the profile of the singular layer is given by

$$\frac{\mathrm{d}^2 y}{\mathrm{d}x^2} = K^{1/3} A x^{-2/3}, \quad \text{where} \quad A = 2^{1/3}/3.$$

Note that

$$\frac{1}{\delta} = K^{1/3} A x^{-2/3} \quad \text{if} \quad x = \mathcal{L} \equiv A^{3/2} K^{1/2} \delta^{3/2}.$$

The function $\mathrm{d}^2 y/\mathrm{d}x^2$ obtained by a numerical differentiation of the Lagrangian formulation is illustrated in figure 4-1, where we take $K = 1$ and $\delta = 0.01$. In

this figure we compare this second derivative both with the function $K^{1/3}Ax^{-2/3}$ and with the maximum estimate of $1/\delta$.

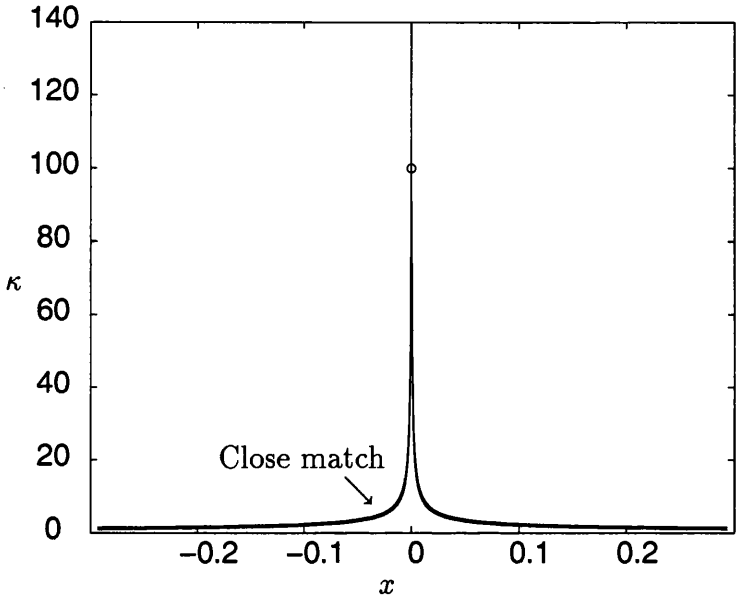

Figure 4-1: The numerically computed curvature, compared with the asymptotic estimate of $K^{1/3}Ax^{-2/3}$ (when $K = 1$) and the maximum estimate of $1/\delta$. There is an excellent match between the asymptotic estimate and the numerically computed curvature as indicated by the arrow.

When δ is small, it is clear from this figure that we can estimate the function $\mathrm{d}^2y/\mathrm{d}x^2$ close to the point $x = 0$ by

$$\frac{\mathrm{d}^2y}{\mathrm{d}x^2} \approx \frac{1}{\delta} \quad \text{if} \quad |x| < \mathcal{L}, \quad \mathrm{d}^2y/\mathrm{d}x^2 \approx K^{1/3}Ax^{-2/3} \quad \text{if} \quad |x| > \mathcal{L}.$$

This estimate allows us to make an asymptotic estimate for the bending energy in terms of δ. As the dominant contribution to the bending energy occurs close to the singular region at $x = 0$ where $\mathrm{d}y/\mathrm{d}x$ is small, we may closely approximate the curvature by the second derivative so that in the limit as $\delta \to 0$

$$\int \kappa^2 \,\mathrm{d}x = \int (\mathrm{d}^2y/\mathrm{d}x^2)^2 \,\mathrm{d}x \approx \frac{8K^{1/2}A^{3/2}}{\sqrt{\delta}}.$$

Hence we have the asymptotic estimate that as t approaches $1/K$ there is a

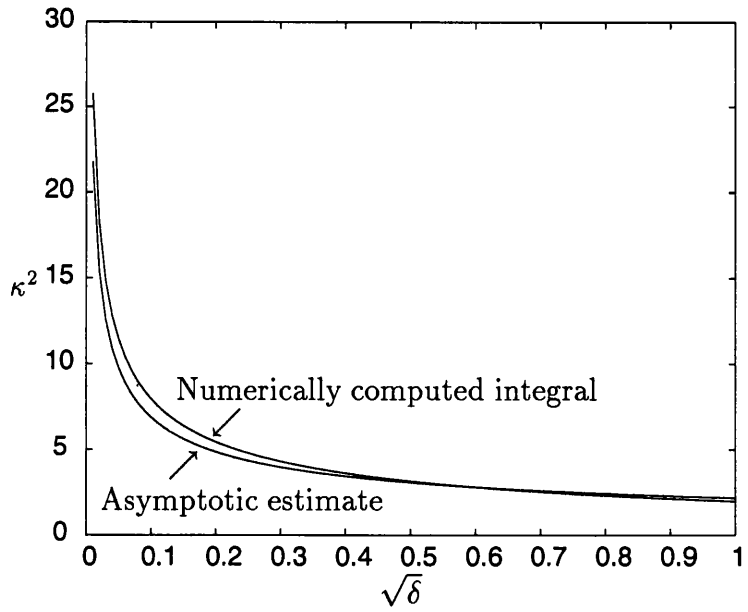

Figure 4-2: The numerically computed integral of $(\mathrm{d}^2y/\,\mathrm{d}x^2)^2$ plotted as a function of δ compared with the asymptotic estimate $8K^{1/2}A^{3/2}/\sqrt{\delta}$, with $K = 1$.

In figure 4-2 we compare a numerically computed integral of the bending energy with the asymptotic estimate and see good agreement.

4.2.2 Multilayer deformation for a particular reference layer profile

To determine the configuration of the multilayer material we must determine the stationary values of the energy functional over all possible configurations of the reference layer Γ_0. This is difficult in general as Γ_0 can take many possible forms, leading to non-unique solutions. A study of some of these for a two-layer material, obtained by approximating Γ_0 by cubic-splines is described in (Hunt et al., 2006). To make progress in the multilayer problem, we will, for the present, restrict the class of solutions to those for which the reference deflection Γ_0 has a sinusoidal profile. Of course this is a restrictive class of solutions, but an inspection of figure 2-8 shows this to be not unreasonable for certain configurations. A fundamental difference between this calculation and earlier approaches is that we only make the assumption that the *reference* layer is a sinusoid, but allow other layers to take different profiles. In other calculations

(see chapter 2) it has been assumed that *all* of the layers have a sinusoid form. This has led to significant underestimates of the total bending energy. Hence, for this calculation, we make the approximation (see Edmunds et al. (2006)) that Γ_0 is given in terms of the arc length l by

$$\Gamma_0 = \left\{(x,y) : y = w_0(l) = Q\cos\left(\frac{\pi l}{L}\right)\right\}, \tag{4.25}$$

and proceed to calculate the other layer profiles using the LSM. For convenience we restrict the calculation to the half-wavelength of total arc length L given by taking $0 \leq l < L$. This profile has a local minimum with maximum curvature K given by

$$K = \frac{Q\pi^2}{L^2}.$$

To find the wavelength L we minimise the critical load in the usual way (see section 1.5.1) to find

$$L = \pi\left(\frac{EI(2n+1)}{k}\right)^{\frac{1}{4}} \tag{4.26}$$

and that the value of P is to be determined. For a given value of Q the horizontal shortening of the layers is given by

$$\mathcal{E} = L - \int_0^L \sqrt{1-\dot{w}_0^2}\,\mathrm{d}l. \tag{4.27}$$

To determine P numerically we calculate the level set function ϕ, evaluate the energy using the formulae in lemma 1, and then find for which values of Q this is stationary. To calculate ϕ a computational grid is set up over a rectangle by dividing the horizontal region $[0, L-\mathcal{E}]$ into $M_1 - 1$ equal intervals of size h such that $x_j = jh, \quad j = 1, \cdots, M_1$. A similar division is made of the vertical region into M_2 regions of width h so that $y_k = kh$. The value of h is chosen to be consistent with the CFL condition, given that the time-step is determined by the layer thickness Δt. In practice it is often convenient to calculate the level sets at more refined intervals than the layers themselves, so we may take a time-step Δ for calculating ϕ given by $\Delta = \Delta t/m$ where m is a suitable integer. The level

set problem is then initialised by taking

$$\phi^0_{kj} = y_k - Q\cos\left(\frac{\pi l_j}{L}\right) \quad \text{with} \quad x_j - \int_0^{l_j} \sqrt{1 - w^2_{0,l}}\,\mathrm{d}l = 0. \tag{4.28}$$

The approximate values of ϕ are then determined at time intervals of Δ by using the methods outlined in section 3.4 and the level sets Γ found by using the MATLAB `contourc` function. The integrals (4.18)–(4.21) are evaluated using a 16 point Gaussian Quadrature rule at every m time steps (corresponding to each layer), and finally, the variation of the total energy V with respect to small changes in Q is found using central differences.

The linear dependence of the total energy on the (fixed) load P allows us to find P as a function of the single variable Q without solving nonlinear equations. In particular, setting $\partial V/\partial Q = 0$ we have simply

$$P = \frac{\partial U_B/\partial Q + \partial U_F/\partial Q + \chi \partial U_\mu/\partial Q}{\partial \mathcal{E}/\partial Q}. \tag{4.29}$$

4.2.3 Summary of approach

The aim of the process is to find a P for a Q that we are free to choose. To find P we consider the energy function V given in terms of the level set function ϕ. However, the reference layer, and hence the initial position of the zero level set, is determined simply by Q. We then use the level set method to propagate this reference layer to find the position of the other layers (each one is given by the zero level set at time $i\Delta t$). The contribution to the energy of each layer is found by first locating the zero level set with `contourc` and then evaluating the integrals (4.18)–(4.21). These contributions are then summed to find the total potential energy.

It is $\partial V/\partial Q$ that we wish to find and not V, so the above process is followed with small changes in Q to approximate $\partial V/\partial Q$ using central differences. Finally,

P follows from equation (4.29).

A plot of the resulting $(\mathcal{E}, P)$ curve in the case of a material with 220 layers of width 0.1 mm and with $L = 35.9$ mm is given in figure 4-3. Here we have taken $M = 180$ which corresponds to $h \approx 0.22$.

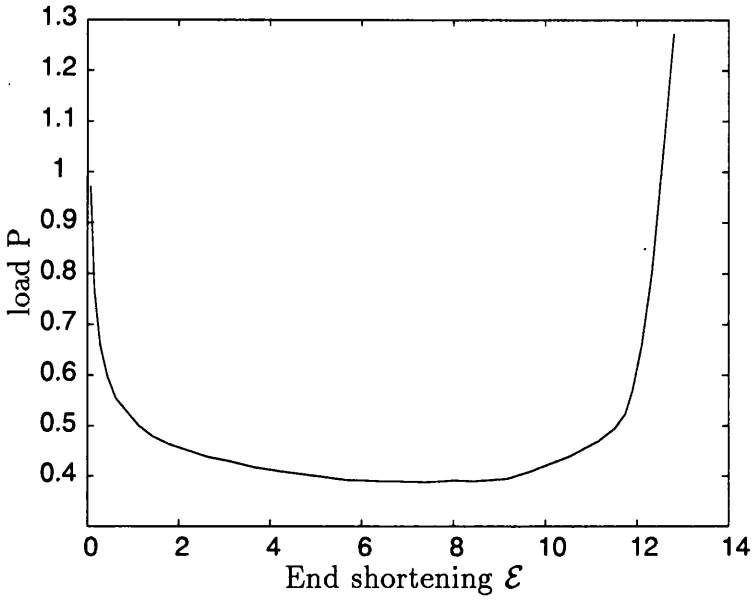

Figure 4-3: A plot of axial load against end-shortening, showing that the bending energy re-stiffens the system.

Using the previous theory we can understand the qualitative form of this figure. If Q is small then each of the terms U_B, U_F and $\mathcal{E}$ are locally quadratic functions of Q and hence their derivatives vary linearly with Q. However, U_μ is a locally linear function of Q and its derivative is constant. Thus as $Q \to 0$ the load

$$P \sim \frac{\chi \partial U_\mu / \partial Q}{\partial \mathcal{E} / \partial Q} \sim \frac{1}{Q} \to \infty$$

(Budd et al., 2003). In contrast, as Q increases further, so the deflection of the layers furthest from the reference layer becomes more nearly singular. As the maximum curvature of the reference layer is given by $K = Q(\pi/L)^2$ and the half thickness t of the total multilayer is given by $t = n\Delta t$ it follows from the

previous subsection, that the bending energy varies as

$$U_B \sim \frac{B}{\sqrt{\frac{L^2}{\pi^2 Q} - n\Delta t}}.$$

In particular, if

$$Q_S = \frac{L^2}{\pi^2 n \Delta t}$$

the bending energy U_B becomes unbounded as $Q \to Q_S$ and there is a constant C so that

$$U_B \approx \frac{C}{\sqrt{Q_S - Q}}.$$

Hence, as the end-shortening only varies slowly with Q as $Q \to Q_S$ we conclude from (4.29) that as $Q \to Q_S$

$$P \sim \frac{1}{(Q_S - Q)^{3/2}}.$$

As we have just described, figure 4-3 shows that the level set method captures the expected behaviour of the system. However, with this mesh size the load does not increase as quickly as would be expected. The reason for this is the difficulty of accurately approximating the second derivative near a corner. An obvious solution to this problem is to refine the mesh, however, we choose not to for two reasons: The first is the increase in computational effort required to solve the equations with refined meshes. The second is that in parallel folding experiments a singularity is not reached and therefore there will be no self-intersection of the curves.

Instead, we choose to make use of equation (3.7) for the evolution of the curvature, allowing us to calculate the bending energy. This is the approach that has been used in the comparison with experiment in chapter 6. We stress that all other terms are calculated with the level set method and that since we have already demonstrated that the level set method gives the correct behaviour, there is no additional value in persevering with the method.

Mechanically, the formation of the singularity in the material is equivalent

to a dramatic re-stiffening of the whole system, seen also in other folding configurations such as kink banding (Wadee et al., 2004). Of course we do not see an infinite load in practice, and for the rock formations considered in this thesis we would expect to see some sort of fracturing or plastic behaviour in this limit, or alternatively the formation of multiple or parasitic folds (see figure 3-3).

4.3 Concluding remarks

Chapters 3 and 4 have shown the potential of the level set method when modelling multilayer problems. We began by showing that the geometry of parallel folding can be approximated by propagating a reference layer in its normal direction. As a direct consequence of the geometry singularities can appear in the outer layers. We have characterised the curvature (and hence the bending energy) as a singularity is approached. The geometrical description of the layers was then coupled with an energy based mechanical model. In chapter 5 we describe a set of experiments that are designed so that direct comparison can be made to validate the theoretical model. The output of the model enables us to compare the wavelength and load against end shortening plots.

Presently, the mechanical model is for parallel folding, although it is anticipated that it can be adapted to model other folding scenarios.

Chapter 5

Experiments

To provide benchmarks against which to test the models, it is often useful to compare against simpler but readily quantifiable systems that can be tested experimentally, such as constrained and compressed layers of paper.

A set of 20 experiments on different examples of layered samples were conducted in the Department of Civil and Environmental Engineering at Imperial College London under the guidance of Dr. Ahmer Wadee. The rig was the same that Wadee et al. (2004) and Edmunds et al. (2006) used in their experiments. Stacks of $m = 2n + 1$ half sheets of A4 paper (105 mm x 297 mm), alternating ten white with ten coloured, were placed between soft foam foundations top and bottom, as shown in the schematic of figure 5-1.

A vertical *overburden pressure* q per unit length was introduced via a rigid screw device, and a longitudinal axial load P was then applied at a constant (slow) rate from the left via a second motorised load applicator. The applicator face had height 20.2 mm for experiments with thin samples (120 or 220 sheets) and 50 mm for the thicker ones (320 or 420 sheets). Both lateral and axial loads were measured using 100 kN load cells as indicated, and displacement transducers recorded the corresponding movements. Readings were taken at 1 second intervals and recorded by a data logger using the DALITE software package.

This set of experiments is subjected to the same load and displacement con-

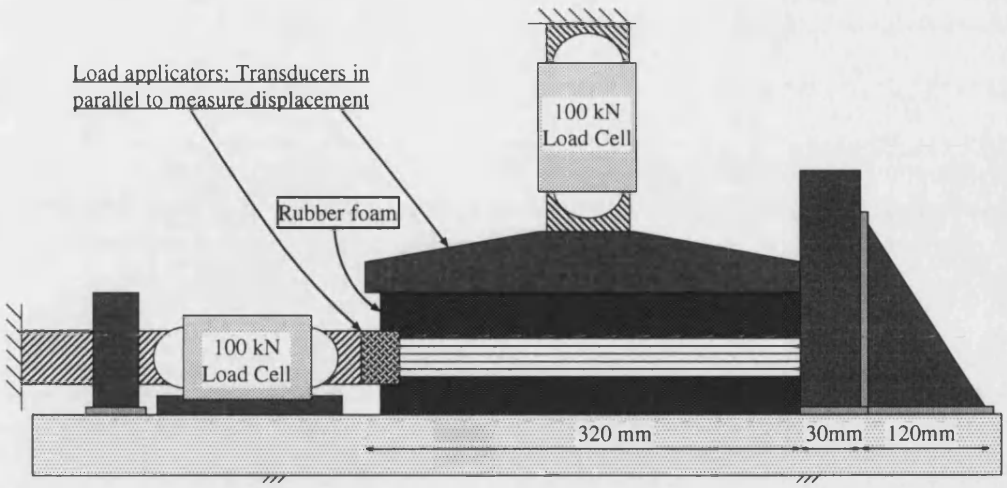

Figure 5-1: Schematic of experimental rig. (After Edmunds et al. (2006))

straints as in Edmunds et al. (2006), namely that the rate of axial loading must be slow enough to at least quasi-static ($\approx 3-4\times10^{-5}\,\mathrm{ms}^{-1}$) and the overburden pressures must be moderate otherwise kink bands could form instead of parallel folds ($\approx 0.5-2.3\,\mathrm{kN}$). Moreover, the foam should be thick enough to stop the rigid (outside) boundaries affecting the buckling process. Ramberg (1961), in a similar set of experiments suggests that this should at least be the same order as the wavelength of the buckle. In view of the uncertainty in the earlier experiments over the stiffening effect of the foundation, and to accommodate thicker multilayer samples, foundations top and bottom of twice the thickness of those reported in Edmunds et al. (2006) were used (approximately 50 mm top and bottom in the present case).

5.1 Some observations

The main characteristics of the experiments can be summarised as follows:

1. In 9 of the 20 experiments *delamination* (often referred to as *internal buckling* by geologists) took place. This can occur when the plunger does not apply load to all the layers (for example when the multilayer is thicker than the plunger height) and only the 'internal' layers buckle (see figure 5-2).

We presume that the effect of internal buckling is to increase the effective foundation stiffness and although the remaining observations also hold for these experiments, we view this as an additional complication and choose to disregard these experiments in the discussion of chapter 6.

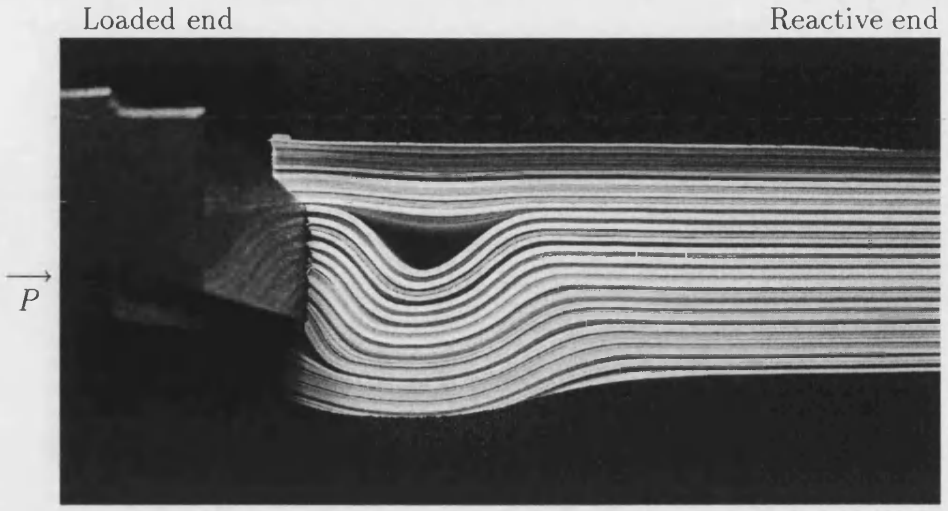

Figure 5-2: Delamination (internal buckling) of 420 sheets of paper. Also indicated is the loaded end on the left and the reactive end on the right. All the following photographs have the loaded end on the left.

2. Initial buckling typically occurred as a single hump at either the loaded (plunger) or the unloaded (reactive) end of the rig. It seemed to initiate with about equal likelihood at either end (there were 6 at the loaded end and 5 at the unloaded end).

3. After the initial instability there were significant differences in the post-buckling behaviour. A fold forming at the loaded end tended to deform locally without spreading along the length, see figure 5-3a, while one forming at the reactive end would initiate a sequence of so-called serial folds (Hunt et al., 2006), as seen in figure 5-4a.

4. Load to corresponding deflection plots for these two instabilities showed considerably greater relative drop in load when buckling initiates at the loaded, rather than the reactive end, as seen when comparing figure 5-3b with figure 5-4b.

5. In one case, after an initial instability at the reactive end, rather than a serial sequence forming, the next hump formed at the loaded end. This is shown in figure 5-5.

Much of this phenomenology seems to be a result of axial friction between the layered sample and the foundation (or shearing in the foundation itself, which would have much the same effect). Before buckling, the load is clearly transmitted through the sample without significant reduction, as evidenced by point 2) above. However, after the initial hump forms, this is no longer the case. Remembering that load is measured at the point where it is applied, if the buckle initiates at the reactive end the load cell will record a combination of load at the hump, and friction from the foundation; thus the output of figure 5-4b shows evidence of a stick-slip sequence. If the initial instability and consequent drop in load themselves are taken as being much the same wherever the buckle forms, point 4) above confirms this frictional effect. Moreover, point 5) can supply an estimate of its magnitude.

Although friction between layers is accounted for, friction between the layers and foundation has yet to be included in the mechanical model. If such friction is similarly felt over the length of the initial fold, so that the load at the loaded end of the hump is greater than that on the reactive side, this could also account for the fact that serial buckling only seems to propagate backwards, as described in point 3) above.

It is interesting to note that in contrast to figure 5-3 the output of figure 5-4 is more irregular, but the deflection pattern more ordered. This again is considered to be the effect of friction. The locking up process of figure 5-3 appears to transfer the axial load directly into the foundation, instead of along the sample. This is underlined by the fact that the axial and lateral load curves of figure 5-3(b) are nearly parallel. The same holds for all samples which buckled initially at the loaded end.

(a)

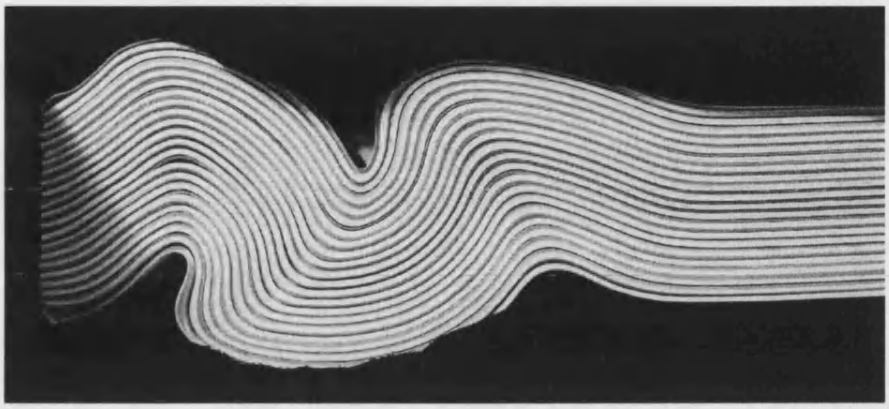

(b)

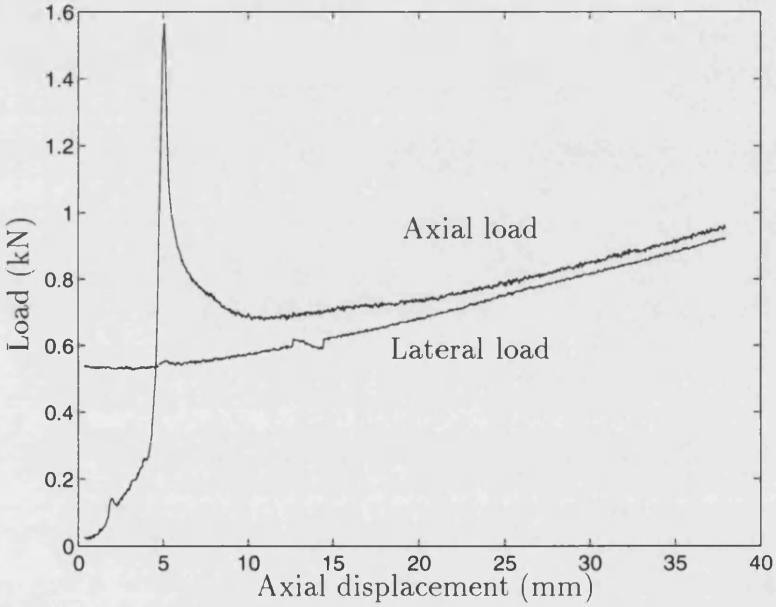

Figure 5-3: Experiment 10. First fold forming at the loaded end. (a) Pattern of deformation. (b) Axial and lateral loads, plotted against axial end shortening. Note that after the buckle has formed both axial and lateral loads both increase as axial displacement increases.

(a)

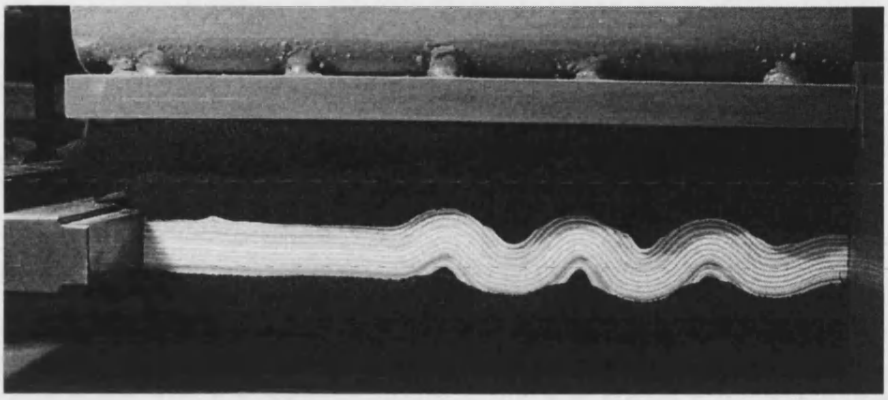

(b)

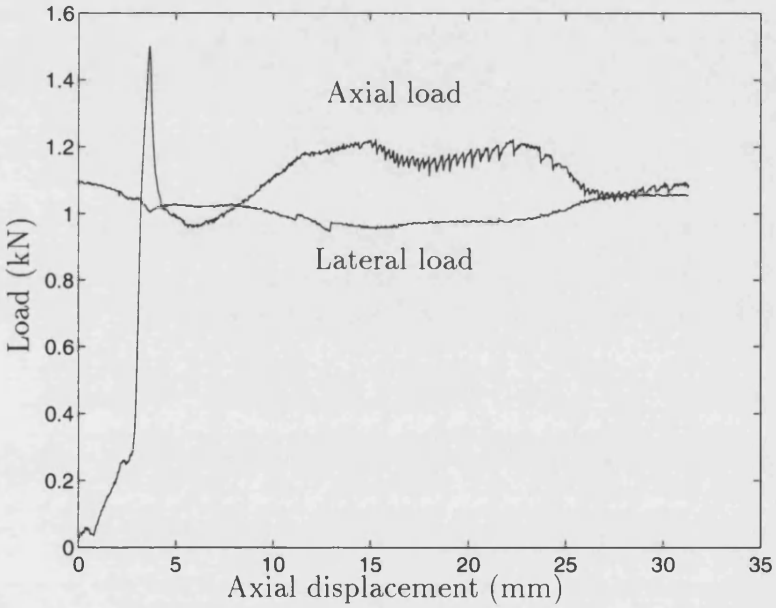

Figure 5-4: Experiment 4. First fold forming at the reactive end. (a) Pattern of deformation. Here we see cellular buckles form at the reactive end. (b) Axial and lateral loads, plotted against axial end shortening. Note the snaking behaviour of axial load and the near constant lateral load.

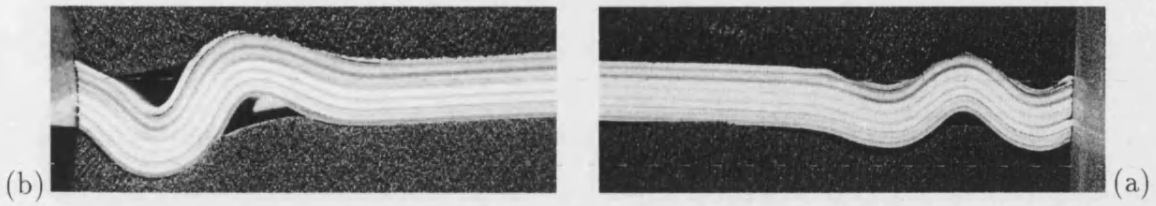

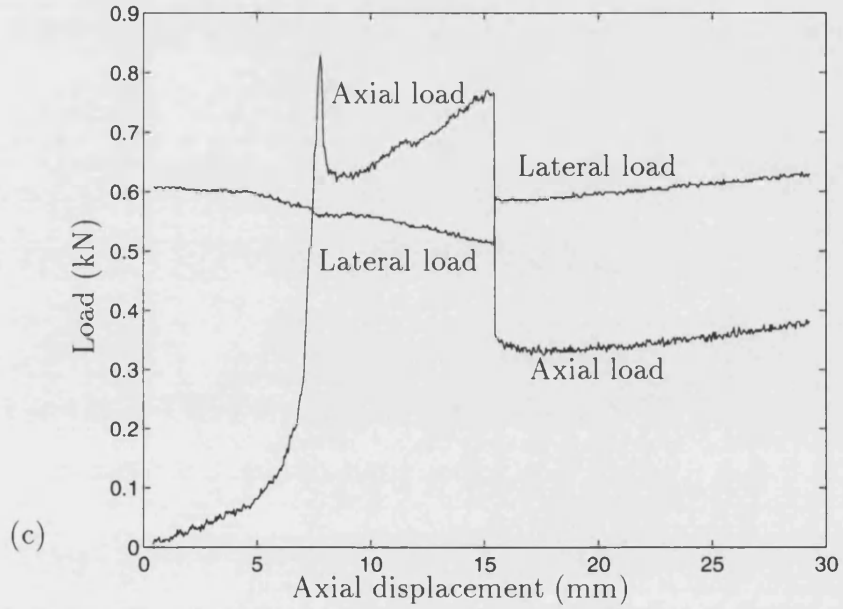

Figure 5-5: Experiment 1. Fold forms first at reactive end (a), and secondly at loaded end (b). (c) Axial and lateral loads, plotted against axial end shortening. Note the sudden drop in axial load and the slight increase in lateral load that occurs when the second fold forms at the loaded end.

5.2 Typical loading scenarios

Given the experimental observations, we have classified the experiments into three buckling scenarios, which we will now describe in turn.

Scenario 1: Thick sample buckles at the loaded end.

Figure 5-6 shows a typical fold developing at the loaded end of the rig. Initially a single localised hump forms, the central layer of which can be approximated by a sine wave. The formation of the second hump seems to 'balance' the system, and although eventually we would expect further humps to form, they do not with significant amounts of end shortening.

We would expect the theory to agree well with these experiments up until the point when multiple humps are formed. When two humps grow simultaneously we would expect to double the end shortening for a particular load.

Scenario 2: Thin sample buckling at either end.

The sequence of figure 5-7 is typical of a thin sample buckling from the loaded end. The first figure in the sequence shows the initial deformation that is significantly different to the thicker sample. The mode shape in this case is asymmetrical with the material to the right of the fold lower than the left. The buckle also appears to be much more like a kink band than the initial deformation of a thicker sample (compare with figure 5-6). At this point we reiterate the point made in section 1.6.2 that the mode shapes $w(s) = \sin(\pi s/L)$ and $w(s) = \cos(\pi s/L)$ give equivalent results; however, $w(s) = \cos(\pi s/L)$ is chosen because friction is acting in the same direction along the buckle and computation is simplified (see section 1.6.2). Therefore, it is the smoother shape of figure 5-6 that is more likely to agree with theory.

As we continue through the sequence the amplitude of the buckle does not significantly change. Instead, the fold hinge closes-up until the material comes

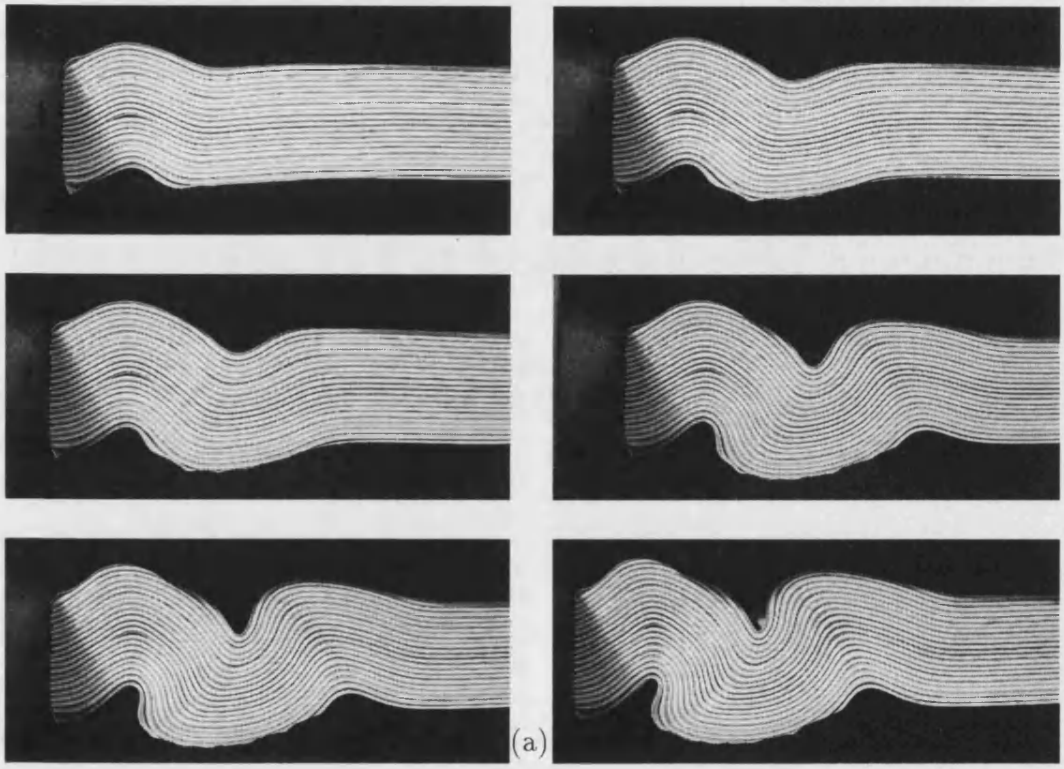

Figure 5-6: Experiment 10. The buckling sequence of 420 layers from the loaded end. The corresponding load against end shortening graph is shown earlier in figure 5-3(b).

into self-contact, by which time the second fold is well developed. This behaviour seems to be elasto-plastic and is not presently in the model.

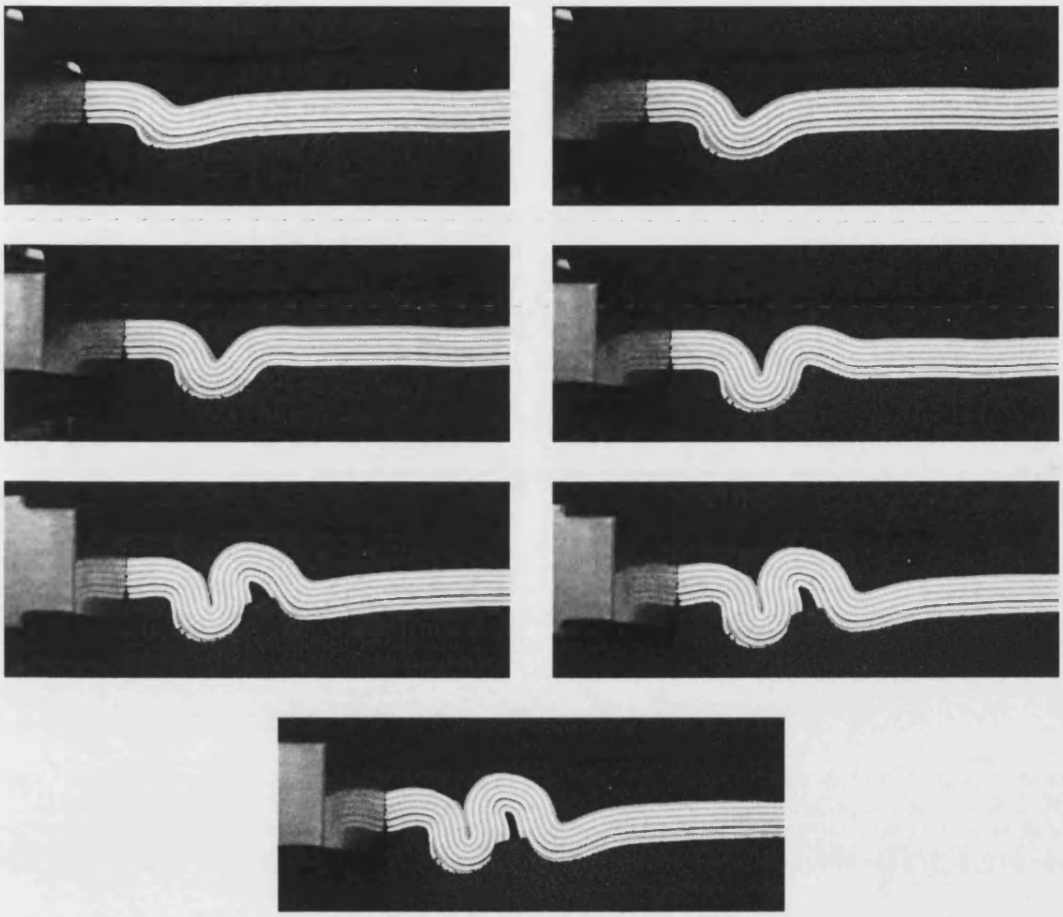

Figure 5-7: Experiment 3. The buckling sequence of a thin sample with 120 layers. The buckle forms at the loaded end.

For completeness we include the corresponding graph of load against end-shortening (see figure 5-8).

Scenario 3: Multilayer (cellular) buckles at the reactive end.

In the sequence of figure 5-9 we can see a serial fold developing along the multilayer. Here the amplitude of a hump undergoes a period of growth until it 'locks up' when the energy makes it preferable for the next hump to form. Typically,

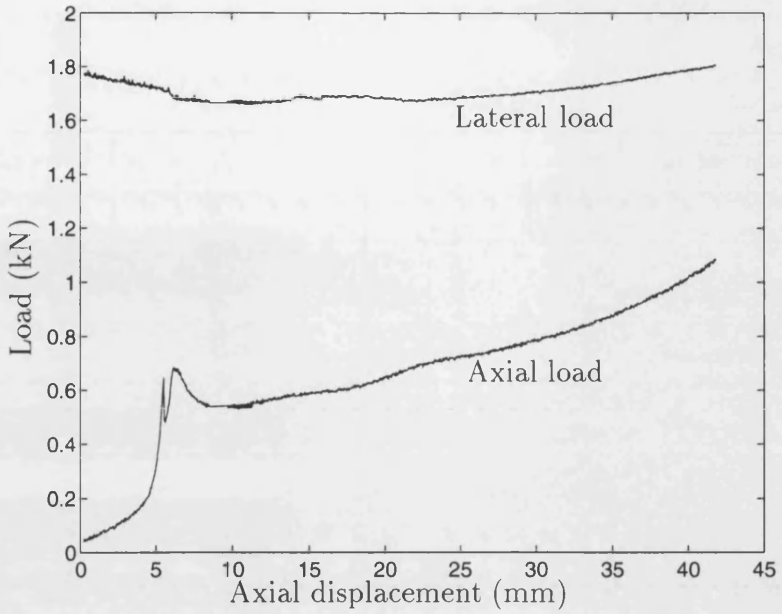

Figure 5-8: Experiment 3. A typical graph of axial and lateral loads plotted against axial end-shortening when a thin sample buckles.

the next hump in the sequence begins to form before the current hump has fully formed. This behaviour is predicted by Hunt et al. (2006).

If it was not for the friction mentioned in section 5.1 we would expect the model to match well with these experiments. However, given our hypothesis we would then expect the theoretical results to predict lower load levels than those seen experimentally.

Again for completeness we add the corresponding load against end-shortening plot 5-10. We note the similarities between this figure and the earlier one of figure 5-4(b), both exhibiting the snaking behaviour.

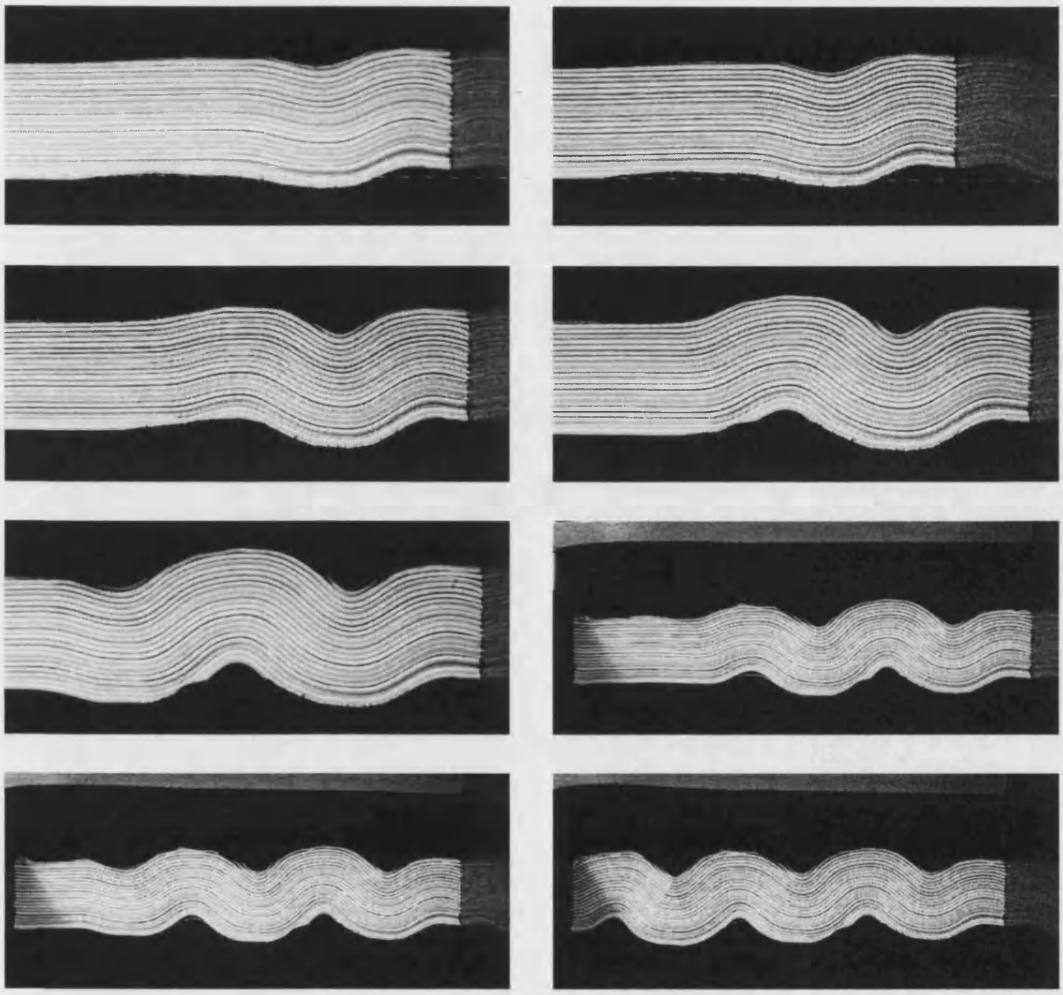

Figure 5-9: Experiment 9. The cellular buckling sequence showing the formation of a serial fold of a thick sample at the reactive end.

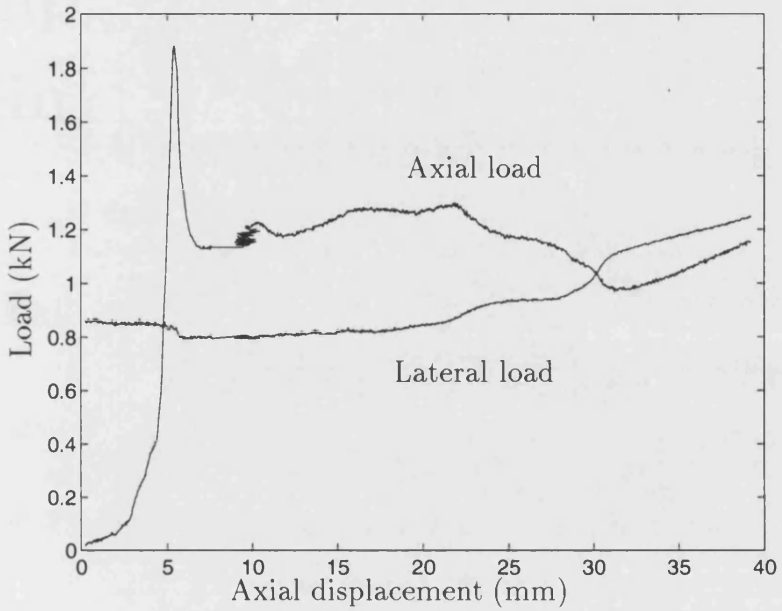

Figure 5-10: Experiment 9. Axial load and lateral load against axial end-shortening

Chapter 6

Comparison of the parallel folding model with experiments

6.1 Introduction

The first part of this chapter describes how we estimate the material properties that are required as inputs for the model. In the second part we compare the theoretical wavelengths and minimum axial load values using the model given in chapter 4 to the experiments described in chapter 5 and find that in some circumstances there is good agreement. Where the agreement is questionable, explanations are sought.

6.2 Comparison with experiments

To compare theory with experiment we require independent estimates of E, q, μ and k, obtained in the following manner.

6.2.1 Young's modulus and second moment of area

Wadee et al. (2004) and Edmunds et al. (2006) used the initial gradient of the $P - \mathcal{E}$ graph to estimate the in-line spring stiffness of the paper k_{layers} (stiffness of foundation is a number of orders of magnitude lower and can be neglected). Then the effective Young's modulus is simply

$$E = \frac{k_{\text{layers}} a}{Tb}, \tag{6.1}$$

where b and a are the breadth and length of the layers respectively and T is the total thickness of the sample.

Table 6.1 gives the average Young's modulus and the overburden pressure per unit length that we obtained using this process and compares our findings with those presented by Wadee et al. (2004) and Edmunds et al. (2006). It is clear that as the overburden drops, so does the effective stiffness of the paper. We suspect that at lower values of q we are not really measuring E due to micro-effects. Hence, we revert to the literature and use a value of 5 kN/mm^2 for all calculations of the bending energy, appropriate for paper with a basis weight of 80 g/m^2 as used here (Alava and Niskanen, 2006). This figure agrees well with compression tests performed with high loads (see table 6.1).

Paper	$\overline{q}$ (kN/mm)	$\overline{E}$ (kN/mm^2)
Wadee et al. (2004)	0.1	4.28
Edmunds et al. (2006)	0.01	1.45
Present thesis	0.004	0.18

Table 6.1: Average Young's modulus $\overline{E}$ and the average overburden pressure $\overline{q}$ based on three sets of experiments performed on layers of paper.

The second moment of area for a single layer is given by

$$I = \frac{b\Delta t^3}{12}. \tag{6.2}$$

6.2.2 Overburden pressure and coefficient of friction

The overburden force per unit length q (often referred to as the *overburden pressure*), of the system is given by the lateral load at the first instability divided by the length of a layer a.

To find the coefficient of friction, μ, a stack of paper is inclined through an angle γ. The critical angle at which the paper begins to slip, γ^*, then determines μ (Wadee, 1999a),

$$\mu = \tan \gamma^* \tag{6.3}$$

Since we were using the same grade and finish of paper as Wadee (1999a), we have assumed a coefficient of $\mu = 0.57$ for our experiments.

6.2.3 Foundation stiffness

A typical feature of energy based models is the difficulty that occurs when trying to estimate the *effective* stiffness of the foundation. This arises due to interactions between foundations lying above and below the multilayer and also the fact that there is a pre-compression in the form of the overburden pressure.

To find an estimate for the foundation stiffness k we performed a set of three compression tests on the foam (in both loading and unloading). Figure 6-1 shows the lateral load against lateral displacement plots of these experiments along with the linear approximation that yields our chosen value for the stiffness.

In the experiments the foam and the multilayer are subjected to a pre-compression. When the layers deflect the total energy is found by subtracting the energy released from one side of the foundation from the energy stored by the other side. If the top surface deflects by an amount δ_1 into the foundation and the bottom surface releases by an amount δ_2 then,

$$U_F = U_{F+} - U_{F-} = \frac{k_{\text{fit}}}{2}(\delta_1^2 + \delta_2^2) \tag{6.4}$$

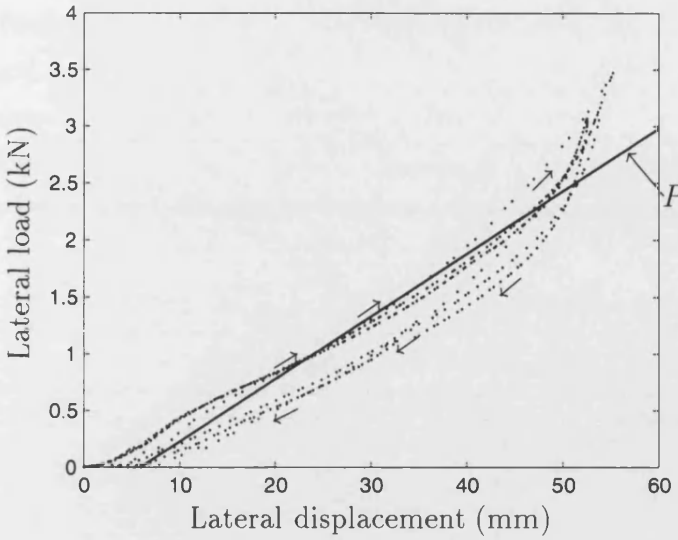

$P_L = 0.055043\Delta_L - 0.32203.$
This corresponds to
$k \approx 7.4\,\mathrm{kN/mm^2}$

Figure 6-1: Lateral compression and decompression tests performed on the foam subsequently used in the parallel folding experiments. The dots were recorded during the experiments and the solid line is a linear fit. It is apparent that there is some hysteresis in the system (the arrows indicate the direction of the loading). Note that the lateral load at the point of instability was between 0.5 kN and 1.8 kN, a region where we have overestimated the foundation stiffness.

If one follows the reasoning of Edmunds et al. (2006) it is necessary to divide the coefficient of the fitted curve k_{fit} by the length a to get the stiffness per unit length of the foundation and also to multiply by 4 to account for two effects. The first is that the compression tests were on four layers compared to two in the paper experiments and the second is because in the foundation tests the foam layers were in series but act in parallel in the paper experiments (see later in figure 6-2 for a simple model of the deflection into the foundation).

$$k = \frac{4k_{\text{fit}}}{a} \tag{6.5}$$

6.2.4 Cubic foundations

As mentioned in the literature review, it is thought that materials made of foam undergo a nonlinear displacement when they are compressed. By considering a cellular description of the foam, idealised nonlinear Winkler models can be de-

rived (Hunt and Wadee, 1998). Edmunds et al. (2006) followed such an approach and considered a foundation model with linear and cubic terms. Since the same pieces of foam were used in both the experiments of Edmunds et al. (2006) and the ones presented in this thesis we feel that it is necessary to justify our use of a linear foundation model:

1. An inspection of figure 6-1 shows that a straight line closely approximates the data over the majority of the values. For the higher values there appears to be a different gradient, suggesting the possibility of a bilinear response, rather than a cubic response.

2. Edmunds et al. (2006) conducted their set of experiments with a higher level of lateral load, which would have put the point of instability further into the stiffened region. Also with single layers of foam, cubic stiffening would occur earlier.

3. The justification for dropping the quadratic term is that in the stiffened region, the foam is dominated by the cubic term. Furthermore, if only the points close to the point of instability are considered then, over such a small range, a linear and cubic term closely fit the data. However, there is no physical reason for choosing such a polynomial and with a small range many different polynomials could be made to fit well.

We will show that the quadratic term has no effect on the energy stored by the foundation. However, its inclusion or omission would have an effect on the linear and cubic terms. For argument's sake, assume the lateral load P_L gives a response that is initially linearly elastic, followed by a quadratic softening nonlinearity and a cubic restiffening nonlinearity. Thus

$$P_L = k_1\Delta_L - k_2\Delta_L^2 + k_3\Delta_L^3 \tag{6.6}$$

where $k_1 > k_2 > k_3 > 0$ and Δ_L is the lateral displacement.

We assume that this cellular model is valid over all deflections seen in the parallel folding experiments, including at the load when the first instability occurs. Now we account for the differences between the parallel folding experiments and

the compression test on the foam. When the foam is used as a foundation in the parallel folding experiments it is first subjected to an overburden pressure. With the level of overburden pressure applied in the experiments it means that any deflections of the paper into the foundation occur in the stiffened region of the foam's loading cycle. We set the point when the first instability occurs equal to (P_L^*, Δ_L^*) and shift the origin to this point so that

$$P_L - P_L^* = k_1(\Delta_L - \Delta_L^*) - k_2(\Delta_L - \Delta_L^*)^2 + k_3(\Delta_L - \Delta_L^*)^3. \tag{6.7}$$

This procedure provides the coefficients for the nonlinear stiffness of the foundation. Importantly the cubic coefficient remains unchanged during this process. However, for $\Delta_L^* \neq 0$ the quadratic coefficient does change. We now show that due to symmetry the quadratic term has no effect on the total energy stored in the foundation. To see this, we simplify the situation and assume that the parallel experiments consist of two springs and that under lateral loading P_L (figure 6-2(a)) the springs have each compressed a distance Δ_0 (figure 6-2(b)). Now let P be an axial load that causes the layers to move into one side of the foundation. Without loss of generality assume that the top layer deflects into the foundation an amount δ_1 and the bottom releases an amount δ_2 (figure 6-2(c)).

When under extra compression δ_1, the first spring gives a positive energy contribution U_{F+}, which is calculated as

$$U_{F+} = \int_{\Delta_0}^{\Delta_0+\delta_1} \left(k_1\Delta - k_2\Delta^2 + k_3\Delta^3\right) \mathrm{d}\Delta. \tag{6.8}$$

As seen in figure 6-3, in the process of rescaling the origin to the point of the first instability we also set $\Delta_0 = \Delta_L^* = 0$ and hence

$$U_{F+} = \int_0^{\delta_1} \left(k_1\Delta - k_2\Delta^2 + k_3\Delta^3\right) \mathrm{d}\Delta = \frac{k_1}{2}\delta_1^2 - \frac{k_2}{3}\delta_1^3 + \frac{k_3}{4}\delta_1^4. \tag{6.9}$$

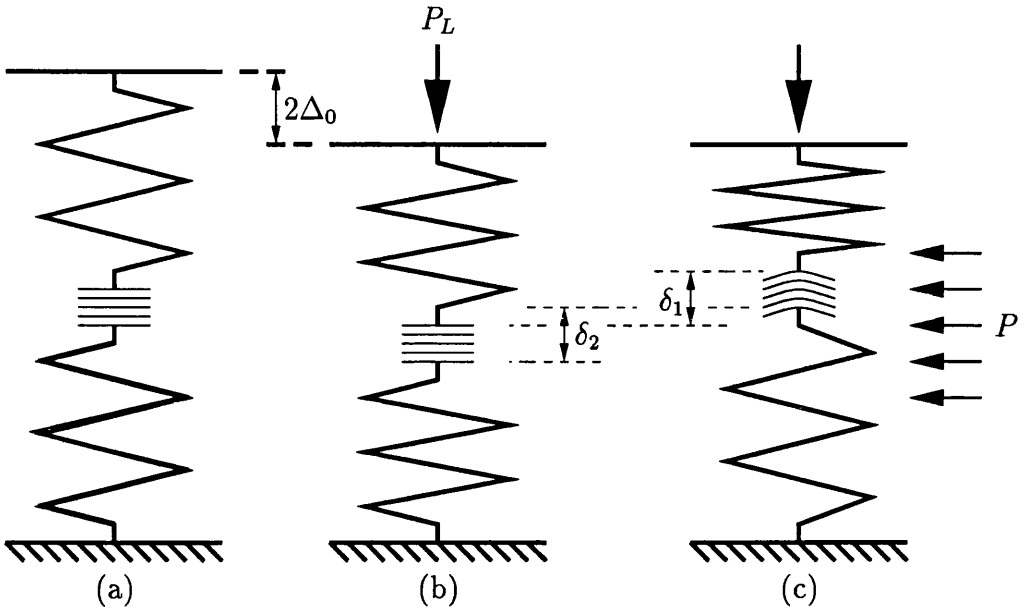

Figure 6-2: The interaction of two springs acting either side of the layers when: (a) unstressed (b) the pre-compression is added causing displacement Δ_0 in each spring and (c) deflection in the sample causes one spring to compress by δ_1 and the other to decompress by δ_2.

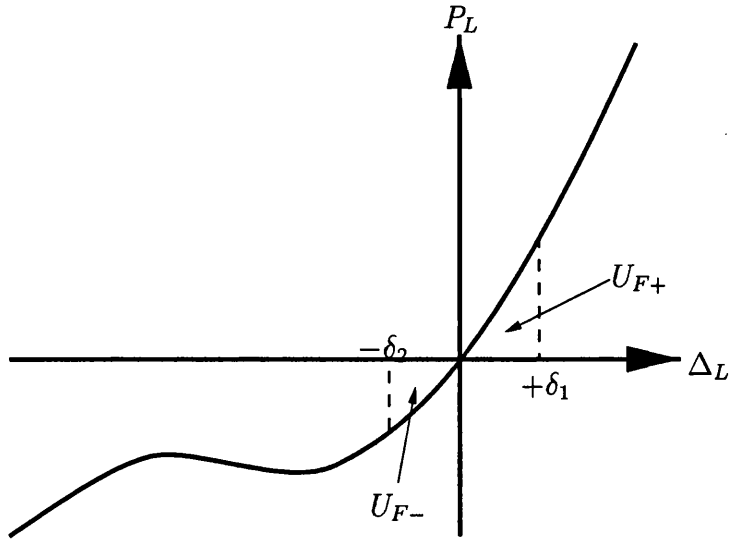

Figure 6-3: Schematic of the $P_L - \Delta_L$ plot of an idealised nonlinear Winkler foundation when increasing and releasing the pre-compression. The figure has been re-scaled such that the origin is at a typical load level of a first instability.

The negative energy contribution U_{F-}, due to the second spring releasing δ_2 of its pre-compression is given by

$$U_{F-} = \int_{-\delta_2}^{0} \left(k_1\Delta - k_2\Delta^2 + k_3\Delta^3\right) \mathrm{d}\Delta = -\frac{k_1}{2}\delta_2^2 - \frac{k_2}{3}\delta_2^3 - \frac{k_3}{4}\delta_2^4. \qquad (6.10)$$

The total energy is found by subtracting the negative energy contribution from the positive contribution

$$U_F = U_{F+} - U_{F-} = \frac{k_1}{2}(\delta_1^2 + \delta_2^2) - \frac{k_2}{3}(\delta_1^3 - \delta_2^3) + \frac{k_3}{4}(\delta_1^4 + \delta_2^4) \qquad (6.11)$$

It is clear that if $\delta_1 \approx \delta_2$ the middle term of equation (6.11) is negligible.

Owing to the symmetry, the even powered terms do not make a contribution to the energy and we are left with linear and cubic coefficients. When this procedure was applied to our compression tests we found a cubic coefficient of 3.49×10^{-7} (kN/mm^4), which is too small to account for the restabilising of the load (for moderate Q).

Summary of our approach

We hoped that a linear fit over all the values would be sufficient to provide accurate results. Fitting over all the values enables the model to be more accurate for large deflections at the expense of a loss of accuracy at the point of instability (if we had just considered that range). Furthermore including points from loading and unloading could be seen as averaging out the effect of hysteresis, which is an unmodelled effect.

In the next section we compare the 11 experiments with theory for $k = 7.4$ kN/mm^2 and find that the wavelength is often underestimated and the minimum load overestimated. We know that the foundation stiffness at the point of instability determines the wavelength, although we did not know how sensitive it would be to the value of k or that there would be a strong correlation between its value and the minimum load.

Therefore we took two approaches. The first was to simply take a linear fit over the range of loads that are seen at the point of instability. This yields a lower stiffness of 5.9×10^{-4} kN/mm^2 (see figure 6-4).

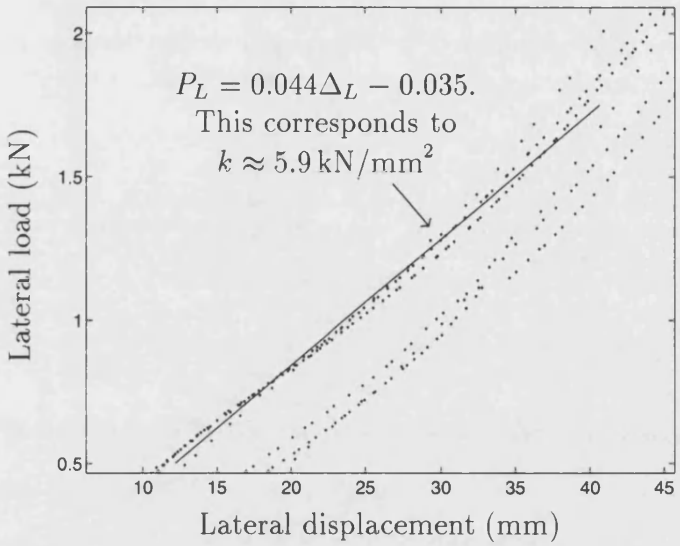

Figure 6-4: A linear fit of the response of the foundation under compression over the range of lateral loads seen at the initial instability

The second approach was to see the range of values that the stiffness could take. We sampled the curve with ten points and found a range of values for k with 5.0×10^{-4} kN/mm^2 $\leq k \leq 3.1 \times 10^{-3}$ kN/mm^2. We argue that by taking the lowest value in this range we can 'reverse engineer' the value of the stiffness to get a close match with the wavelength. Rather unsurprisingly we will see later that the lower value of $k = 5 \times 10^{-4}$ kN/mm^2 yields a closer match in both the wavelength and the minimum load.

6.2.5 Wavelength and minimum load comparisons

In table 6.2 we present the material constants that are common to all 11 experiments.

Theoretical wavelengths are calculated with equation (4.26) and are presented in table 6.3 along with experimental values that were obtained from measurement

Quantity	Value
a (mm)	297
b (mm)	105
Δt (mm)	0.1
E (kN/mm^2)	5
I (mm^4)	0.00875
k (kN/mm^2)	7.4×10^{-4}

Table 6.2: Experimental quantities.

of photographs of the folds. Also in table 6.3 are the comparisons between the minimum load values P_{min}.

Expt	Experiment					Theory		% Error	
	m	T (mm)	q (kN/mm)	L (mm)	P_{min} (kN)	L (mm)	P_{min} (kN)	L	P_{min}
1	120	12	.0019	22.3	0.62	28.8	–	29.1	–
2	120	12	.0037	25.4	0.45	28.8	–	13.4	–
3	120	12	.0057	28.2	0.53	28.8	–	2.1	–
4	220	22	.0034	33.2	0.96	33.5	0.48	0.9	-50
5	220	22	.0078	42.2	0.95	33.5	0.58	-20.6	-39
6	320	32	.0031	40.0	1.16	36.8	0.85	-8.0	-27
7	320	32	.0059	46.4	1.44	36.8	0.97	-20.7	-33
8	320	32	.0019	44.0	0.56	36.8	0.79	-16.4	41
9	420	42	.0028	45.1	1.13	39.4	1.25	-12.6	11
10	420	42	.0018	47.5	0.68	39.4	1.18	-17.1	74
11	420	42	.0058	45.1	1.35	39.4	1.48	-12.6	10

Table 6.3: Comparison of theoretical and experimental wavelengths and the percentage error. Also shown are the theoretical and experimental values of the minimum load.

In the majority of the experiments there is a good agreement between the theoretical and the experimental wavelengths as seen by the relatively low values of the percentage error. There appears to be a thickness effect that we are missing as we are slightly overestimating the wavelength for thin samples and underestimating for thick samples.

We will now discuss the minimum load estimates in terms of the three folding scenarios of chapter 5.

Scenario 1: Thick sample buckling at the loaded end

This is the group of experiments that we expect the theory to match well with the experiments. The experiments included in this group are numbers 8, 10 and 11. Experiment 11 closely matches with the experiment and the $(P, \mathcal{E})$ plot shows the restabilisation due to the bending energy (figure 6-5).

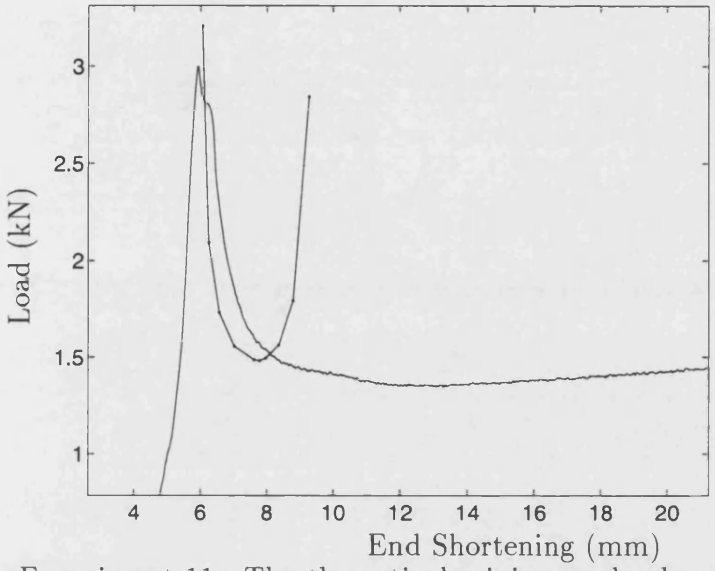

Figure 6-5: Experiment 11. The theoretical minimum closely matches the experimental minimum.

Conversely, at the chosen value of $k = 7.4 \times 10^{-4}$ the theory for experiments 8 and 10 vastly overestimates the experimental minimum load. To address this we substitute the lower bound for the foundation stiffness of $k = 5 \times 10^{-4}$ kN/mm^2. As seen in the discussion of section 6.2.4 it is not surprising that this value produces better results: the main effect is that the energy stored by the foundation decreases. A more subtle effect of the lower stiffness is that the wavelength increases, which increases the amplitude of the fold before a singularity appears and allows the load to drop further. The resulting comparison is presented in table 6.4.

The resulting load against end-shortening plots are shown in figure 6-6.

Expt	Experiment					Theory		% Error	
	m	T (mm)	q (kN/mm)	L (mm)	$P_{\min}$ (kN)	L (mm)	$P_{\min}$ (kN)	L	$P_{\min}$
8	320	32	.0019	44.0	0.56	40.6	0.58	-7.7	3.6
10	420	42	.0018	47.5	0.68	43.5	0.87	-8.4	27.9

Table 6.4: Comparison between theory and experiment when the lower bound is used for the foundation stiffness (c.f. table 6.3).

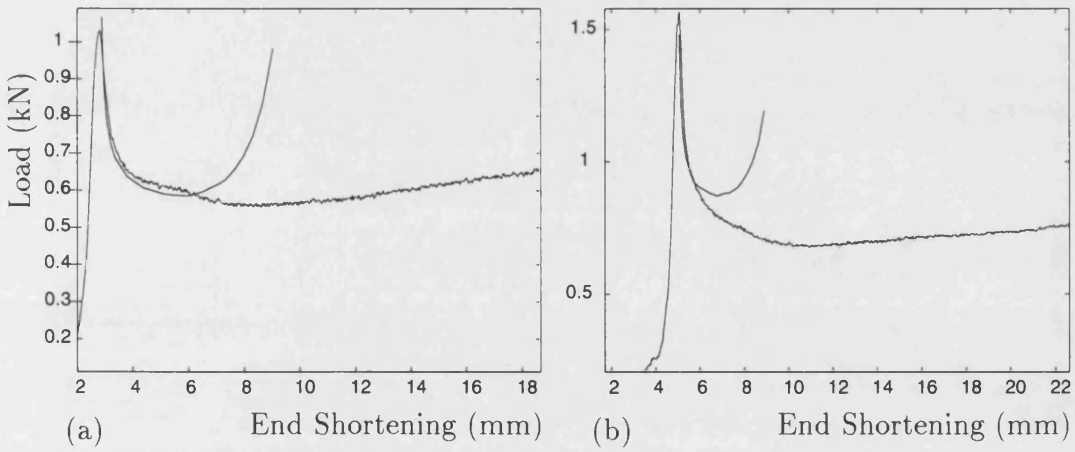

(a) (b)

Figure 6-6: Theory is more closely matched with experiment when a lower bound is used for the foundation stiffness. (a) Experiment 8 & (b) Experiment 10.

Scenario 2: Thin sample buckling at either end

This group contains experiments 1–5. Experiments 1–3 significantly underestimate the load. For these experiments the theoretical load does not restabilise as shown in figure 6-7(a). This is because the amplitude required to reach a singularity is larger than the material can deflect to, whilst maintaining a sinusoidal reference layer (for large values of $|Q|$ (4.27) admits complex solutions). Experiments 4 & 5 are an improvement, and a minimum is obtained; however, the comparison with the theory is poor (see figure 6-7(b)). Given the poor agreement and the observation of the loading sequence in chapter 5 it is likely that a different mechanism is governing the folding of thin samples.

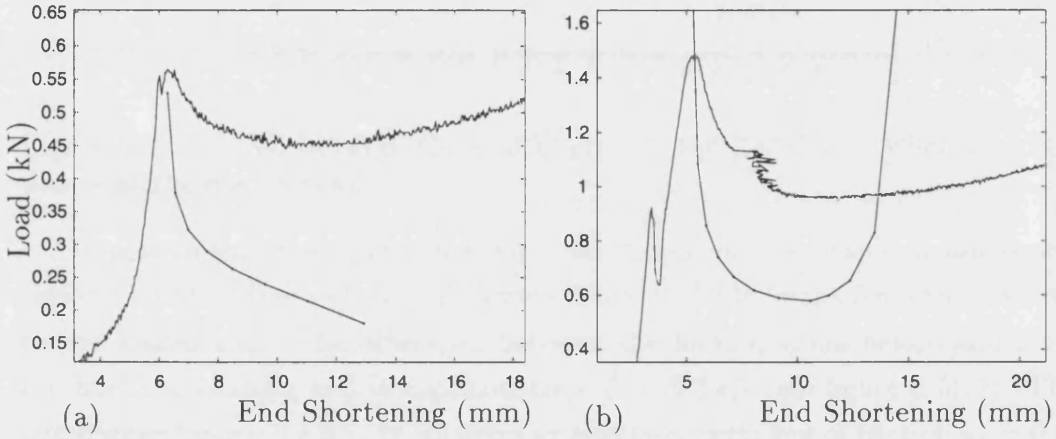

Figure 6-7: Theory does not match well with experiment for thin samples. (a) Experiment 2 (b) Experiment 5

Scenario 3: Thick sample buckling at the reactive end

The remaining experiments, 6, 7 & 9 all buckled at the reactive end. In this scenario we expected the theoretical load to underestimate the experimental load, which is the case in experiments 6 & 7. To account for the friction between the boundary layers and the foundation (see figure 6-8) we must add a term to the total energy formulation

$$V = U_B + U_F - P\mathcal{E} + \chi U_\mu + P_L \mu_1 \mathcal{E} \tag{6.12}$$

where μ_1 is the *effective* coefficient of friction between the foundation and the layers. The coefficient is effective because the height of the load applicator was not always the same as the multilayer thickness and therefore some shearing of the foundation might be encountered.

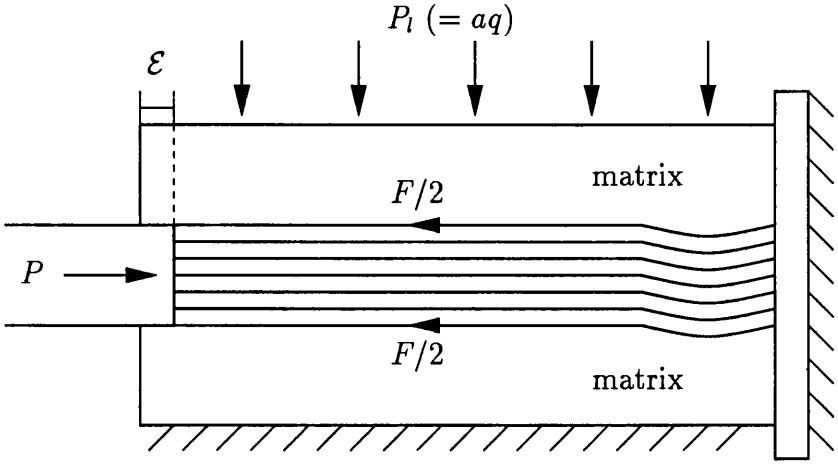

Figure 6-8: Friction between the multilayer and the foundation when buckling occurs at the reactive end

To make a tentative approximation to the coefficient we consider again experiment 1 and the drop in load that occurs when buckling swaps from the reactive to the loaded end. The difference between the local minima before and after the buckling changes end is approximately $F = 0.3\,\text{kN}$ (see figure 5-5(c)). The overburden force is 0.5 kN, which gives an effective coefficient of friction $\mu_1 = 0.6$.

To improve the comparison between the theoretical and experimental wavelengths we follow the reasoning of scenario 1 and choose a foundation stiffness of $k = 5 \times 10^{-4}\ \text{kN/mm}^2$. Note that we have assumed that the frictional force is only felt once the multilayer is buckled and therefore does not change the wavelength (see the observations and discussion in chapter 5).

Adding the frictional force between the foundation and the layers then produces the results given in table 6.5.

We can see that the agreement between the minimum load values is improved for experiments 6 & 7 when the additional friction is included. It is also apparent that the difficulty in predicting the foundation stiffness still persists in the experiments buckling at the reactive end. When the lowest experimentally ob-

Expt	Experiment					Theory		% Error	
	m	T (mm)	q (kN/mm)	L (mm)	$P_{\min}$ (kN)	L (mm)	$P_{\min}$ (kN)	L	$P_{\min}$
6	320	32	.0031	40.0	1.16	40.6	1.19	1.5	3
7	320	32	.0059	46.4	1.44	40.6	1.85	-12.5	28
9	420	42	.0028	45.1	1.13	43.5	1.45	-3.5	28

Table 6.5: Comparison between theory and experiment when additional friction between the layers and the foundation is included and the lower bound is used for the foundation stiffness (c.f. table 6.3).

served value is used for the stiffness, both the wavelength and the minimum load values are improved. Furthermore, by fully reverse engineering the stiffness so that the theoretical and experimental wavelengths match, we would expect the minimum load values to match more closely. However, the foundation stiffnesses would then be lower than those seen experimentally in the compression tests.

For experiment 9, the agreement of the minimum load values is not as good when the additional friction is included. However, the agreement is still not unreasonable and the percentage error is the same as that for experiment 7. Clearly an improvement could be gained by reverse engineering the foundation stiffness, as outlined in the previous paragraph.

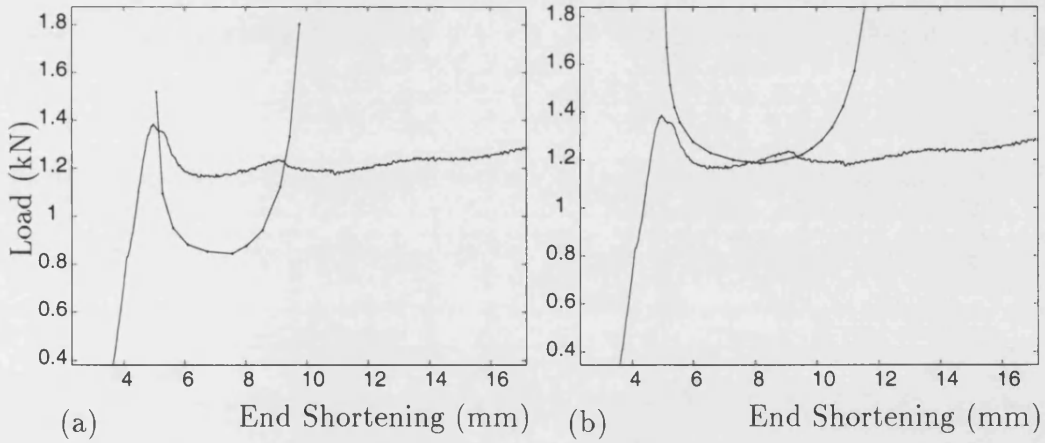

Figure 6-9: Experiment 6. (a) When the multilayer buckles at the reactive end, the theoretical load underestimates the experimental load. (b) The situation is improved when friction between the multilayer and the foundation is included and the foundation stiffness is lowered.

6.3 Chapter summary

As a final comment, it is worth noting that although we started with 20 experiments, once the experiments where delamination of the multilayer occurred were removed, we were left with only 11. By observing the experiments we noticed differences that we had not anticipated. These differences made it necessary to classify the experiments into three scenarios, which meant having as few as three experiments in a group to test our hypotheses. So having set out only to validate our model against the experiments, we also learnt a great deal from the experiments themselves. We nevertheless found that when the sample is sufficiently thick, the parallel folding model agrees well with the experimental results. However, the diminished amount of data has meant that the comparison with the model should be viewed as a pilot study and as such, any conclusions will need to be confirmed with further research, possible directions of which are provided in the following chapter.

Chapter 7

Conclusion

7.1 Concluding remarks

The work presented in this thesis has shown how the level set method can be used to describe the geometry of multilayer folding in rocks and in paper. The literature review argued that simple elastic models have a role to play in modelling multilayer folding, although previous elastic models had not accurately described the geometry of the whole of the multilayer. To describe the geometry of layers that are in contact along their length, we pick a reference layer and propagate it in its normal direction. Unlike earlier models (for example Edmunds et al. (2006)) this describes the geometry of subsequent layers without approximation.

Eulerian methods are able to describe both smooth and kinked layers and of these methods the level set method is accurate and easy to implement. In section 3.2 the method is applied with a constant velocity to photographs of different multilayer folds and the geometry of parallel folds matches closely with the outcome of the method. In contrast, the geometry of chevron folds require a different weak solution to describe the propagation of a salient corner.

The model is then developed and compared to a set of experiments on paper and the key findings are as follows:

- Singularity formation in parallel folding is purely due to the geometry of the layers as they pack together.
- A reference curve propagated in its normal direction will conserve its arc length; provided (a) that the curve remains sufficiently smooth and (b) the angle of the end points with the horizontal is the same at both ends. This does however imply slip between layers.
- By considering the Lagrangian representation we have characterized the curvature and therefore the bending energy as it approaches a singularity.
- A mechanical model has been formulated in terms of the level set description of the geometry.
- To validate the method we performed a set of experiments to produce parallel folds in layers of paper. The observations of these experiments show the importance of friction and its role in determining the post-buckling behaviour; for the range of parameters considered, if buckling initiated at the loaded end the fold remained localized and did not propagate along the multilayer; conversely if it initiated at the reactive end, serial folding propagates back through the multilayer. If tectonic loading is applied in a similar manner to the way it is applied in the paper experiments (to one end of the rocks) this information could aid geologists in understanding serial folding (Vita–Finzi, 2005). These observations led to a classification of three different folding scenarios (section 5.2).
- For thick samples of paper buckling at the loaded end there was good agreement between theory and experiment. In particular, the nonlinear bending energy seemed to account for the restabilising of the load, determining the minimum value.

These findings have shown the value of using modern mathematical techniques to describe multilayer problems. The application of the level set method has yielded a greater understanding of the impact that singularities have in rock folding. It has also meant that fewer approximations are required to describe the geometry of the multilayer than previous methods. However, there is still

a need for further experimental work and although we have demonstrated that there is much to be gained from simple experiments conducted on layers of paper it would be advantageous to consider materials more closely resembling rock. Whilst providing some answers to multilayer folding problems this work has unearthed new questions and further avenues of research for the future.

7.2 Further work

The level set approach has enabled us to describe the role that the bending energy has in restabilising a parallel fold. It would be simple to build more efficient methods to do this by employing fast marching and narrow band schemes as outlined by Sethian (1999). This would speed up the computation time of the method so that grids with more points could be considered.

A big advantage of the level set method is its ability to propagate non-smooth solutions. Therefore this method has the potential to describe both parallel folding and kink banding in a single formulation. Modelling the geometry of kink banding with the level set method would not give us any more insight into this phenomenon as the assumption is that all layers are the same. Instead, a level set based model of kink banding could enable us to investigate the transition between parallel folding and kink banding.

In order to investigate the transition between parallel folding and kink banding with the level set method, there are a number of problems that must be addressed. The first is that as we have already stated, the level set method does not give directly the weak solution that describes kink banding. An approach to model this situation could be to apply the faceted crystal growth ideas to kink banding (Russo and Smereka, 2000). The second, is that at present the method inputs a reference curve that must be known before the other layer geometries are found. Therefore another procedure must be used to first find the shape of the reference layer, based on the loads and the material properties. The weak solution used to propagate this layer would then somehow be linked to the geometry of the layer.

Further complications that could be considered in the future include the parasitic folding that we saw in chapter 3, the formation of voids and the possibility of faulting.

The simple experiments on layers of paper have helped us to understand the mechanisms of multilayer folding. Our observations of the experiments, and the process of comparing them with theory have led to questions to which we have provided explanations. To test these ideas it would be interesting to conduct another set of experiments, where the following alterations could be investigated:

- To minimise the effect that the friction has on the axial load and to amplify the bending energy there are a number of options available to us. Firstly, we could lubricate the layers with graphite to decrease the friction between them (although it might be rather time consuming). Secondly, to increase the bending energy, thicker sheets of paper (or card) could be used.

- The slow rate of loading together with vibrations caused by the motorised loading mechanism, apparently leads to *shakedown* such that the directional effect of the friction is lost. Evidence for this is found in the fact that the initial buckle formed with equal likelihood at the loaded or reactive end. It is also suggested that this would have no time to operate over the rapid loading process. Varying the loading rates could give new information about the presence or otherwise of this shakedown phenomenon.

- In order to test the theory that the load is lower at the reactive end than the loaded end it would be interesting to replace the fixed plate with a load cell. However, the load cell would require a little axial movement, which could impact on shakedown.

- To test if there is an intermediate state between parallel folding and kink banding a greater range of lateral loads could be used. However, with the current rig this is limited by the fact that the greater the lateral load is the greater the lateral displacement is, which can position the multilayer below the load applicator and leads to internal buckling. This can be overcome in part by adding metal plates of differing thickness below the multilayer,

however, a rig redesign would be beneficial to allow a greater range of loads and multilayer thicknesses.

References

M. Alava and K. Niskanen. The physics of paper. *Rep. Prog. Phys.*, **69**, 669–723, 2006.

G. Barles. Remarks on a flame propagation model. Technical Report 464, INRIA, 1985.

M. A. Biot. Bending of an infinite beam on an elastic foundation. *ASME J. Appl. Mech.*, **4**, A1–A7, 1937.

M. A. Biot. Folding instability of a layered viscoelastic medium under compression. *Proc. R. Soc. Lond. A*, **242**, 444–454, 1957.

M. A. Biot. Theory of folding of stratified viscoelastic media and its implications in tectonics and orogenesis. *Geol. Soc. Am. Bull*, **72**, 1595–1620, 1961.

M. A. Biot. *Mechanics of Incremental Deformations.* Wiley, New York, 1965.

P. Blay, J. W. Cosgrove, and J. M. Summers. An experimental investigation of the development of structures in multilayers under the influence of gravity. *J. Geol. Soc. Lond.*, **133**, 329–342, 1977.

J. A. Boon, C. J. Budd, and G. W. Hunt. Level set methods for the displacement of layered materials. *Proceedings of the Royal Society London A*, **463**, 1447–1466, 2007a.

J. A. Boon, C. J. Budd, and G. W. Hunt. Level set model for parallel folding of multilayered structures: comparisons with experiment. *J. Mech. Phys. Solids*, 2007b. In preparation.

L. Bourgouin, H. B. Mühlhaus, A. J. Hale, and A. Arsac. Towards realistic simulations of lava dome growth using the level set method. *Acta Geotechnica*, **1**, 225–236, 2006.

C. J. Budd, R. Edmunds, and G. W. Hunt. A nonlinear model for parallel folding with friction. *Proc. R. Lond. A*, **459**, 2097–2119, June 2003.

C. J. Budd, G. W. Hunt, and M. A. Peletier. Self-similar fold evolution under prescribed end-shortening. *Math. Geol.*, **31**, 989–1005, 1999.

C. J. Budd and M. A. Peletier. Approximate self-similarity in models of geological folding. *SIAM Appl. Math.*, **60**(3), 990–1016, 2000.

M. K. Cameron, S. Fomel, and J. A. Sethian. Seismic velocity estimation using time migration velocities. *Inverse Problems*, 2006. submitted.

W. M. Chapple. A mathematical theory of finite-amplitude rock-folding. *Bull. Geol. Soc. Amer.*, **79**, 47–68, 1968.

D. L. Chopp. Computing minimal surfaces via level set curvature flow. *Journal of Computational Physics*, **106**, 77–91, 1993.

R. Courant, K. Friedrichs, and H. Lewy. Uber die patiellen differenzengleichungen der mathematischen physik. *Mathematische Annalen*, **100**(1), 32–74, 1928.

P. Couteau. Agios pavlos. Postcard, K. Mantzios, Athens.

M. G. Crandall, L. C. Evans, and P. L. Lions. Some properties of viscosity solutions of Hamilton–Jacobi equations. *Tran. AMS*, **282**, 487–502, 1984.

M. G. Crandall and P. L. Lions. Viscosity solutions of Hamilton–Jacobi equations. *Tran. AMS*, **277**, 1–42, 1983.

J. B. Currie, H. W. Patnode, and R. P. Trump. Development of folds in sedimentary strata. *Geol. Soc. Am. Bull.*, **73**, 655–674, 1962.

L. U. de Sitter. *Structural Geology.* McGraw–Hill, New York, 1964.

A. Dervieux and F. Thomasset. A finite element method for the simulation of Rayleigh–Taylor instability. *Lecture notes in mathematics*, **771**, 145–159, 1979.

A. Dervieux and F. Thomasset. Multifluid incompressible flows by a finite element method. *Lecture notes in physics*, **11**, 158–163, 1981.

R. Edmunds. *Parallel folding with friction.* PhD thesis, Univ. of Bath, 2005.

R. Edmunds, G. W. Hunt, and M. A. Wadee. Parallel folding in multilayered structures. *J. Mech. Phys. Solids*, **54**, 384–400, 2006.

D. Enright, R. Fedkiw, J. Ferziger, and I. Mitchell. A hybrid particle level set method for improved interface capturing. *J. Comp. Phys.*, **183**, 83–116, 2002.

L. Euler. *Methodus inveniendi lineas curvas maximi minimive proprietate graduentes.* 1744. Appendix: De cuvis elasticis.

C. J. N. Fletcher. *Structures in folded rocks.* Ministry of Overseas Development, United Kingdom, 1978.

Y. B. Fu and Y. T. Zhang. Continuum-mechanical modelling of kink-band formation in fibre-reinforced composites. *Int. J. Solids Struct.*, **43**, 3306–3323, 2006.

S. Goldstein. The stability of a strut under thrust, when buckling is resisted by a force proportional to the displacement. *Cambridge Philos. Soc. Proc.*, **23**, 120–129, 1926.

B. E. Hobbs, W. D. Means, and P. F. Williams. *An Outline of Structural Geology.* Wiley, Brisbane, 1976.

G. W. Hunt, R. Edmunds, C. J. Budd, and J. W. Cosgrove. Serial parallel folding with friction: a primitive model using cubic B-splines. *J. Struct. Geol.*, **28**, 444–455, 2006.

G. W. Hunt, H. B. Mühlhaus, and A. I. M. Whiting. Folding processes and solitary waves in structural geology. *Phil. Trans. R. Soc. Lond. A*, **355**, 2197–2213, 1997.

G. W. Hunt, M. A. Peletier, and M. A. Wadee. The Maxwell stability criterion in pseudo-energy models of kink banding. *Journal of Structural Geology*, **22**, 669–681, 2000.

G. W. Hunt and M. A. Wadee. Localization and mode interaction in sandwich structures. *Proc. R. Soc. Lond., A*, **454**, 1197–1216, 1998.

G. W. Hunt, M. A. Wadee, and M. A. Peletier. Friction models of kink banding in compressed layered structures. pages 249–256. Proceedings of the 5th International Workshop on Bifurcation and Localization in Geomechanics (IWBL99), Lisse: Swets & Zeitlinger, 2001.

A. M. Johnson. *Styles of folding.* Elsevier, Amsterdam, 1977.

A. M. Johnson and E. Honea. A theory of concentric, kink and sinusoidal folding and of monoclinical flexuring of compressible, elastic multilayers. II. Initial stress and nonlinear equations of equilibrium. *Tectonophysics*, **25**, 261–280, 1975.

P. H. Kuenen and L. U. de Sitter. Experimental investigation into the mechanisms of folding. *Leidsche Geol. Med.*, **XII**, 219–239, 1938.

R. J. LeVeque. *Numerical methods for conservation laws.* Birhäuser Verlag, Boston, 1992.

R. Malladi and J. A. Sethian. Image processing via level set curvature flow. *Proc. Natl. Acad. of Sci.*, **92**, 7046–7050, 1995.

F. A. McClintock and J. B. Walsh. Friction in Griffiths cracks in rock under pressure. *Proc. 4th U.S. National Congr. on Appl. Mech.*, pages 1015–1021, 1962.

K. W. Morton and D. F. Mayers. *Numerical solution of partial differential equations: an introduction.* CUP, Cambridge, 1994.

W. Noh and P. Woodward. A simple line interface calculation (slic). pages 330–340. Proceedings of the 5th International Conference on Fluid Dynamics, Springer, 1976.

S. Osher and R. Fedkiw. *Level Set Methods and Dynamic Implicit Surfaces.* Springer-Verlag, New York, 1st edition, 2003.

S. Osher and J. A. Sethian. Fronts propagating with curvature-dependent speed: Algorithms based on Hamilton–Jacobi formulations. *J. Comp. Phys.*, **79**, 12–49, 1988.

S. J. Osher and F. Santosa. Level set methods for optimization problems involving geometry and constraints 1. Frequencies of a two-density inhomogeneous drum. *J. Comp. Phys.*, **171**, 272–288, 2001.

N. J. Price. Laws of rock behaviour in the Earth's crust. In W. H. Sommerton, editor, *Rock mechanics-theory and practice*, pages 3–23. Proceedings of 11th Symposium of Rock Mechanics. A. I. M. M., 1970.

N. J. Price. Rates of deformation. *J. Geol. Soc. Lond.*, **131**, 553–575, 1975.

N. J. Price and J. W. Cosgrove. *Analysis of Geological Structures.* Cambridge University Press, Cambridge, UK, 1st edition, 1990.

H. Ramberg. Contact strain and folding instability of a multilayered body under compression. *Geol. Rundsch.*, **51**, 405–439, 1961.

H. Ramberg and E. Strömgård. Experimental tests of modern buckling theory applied on multilayered media. *Tectonophysics*, **11**, 261–272, 1971.

J. G. Ramsey. *Folding and fracturing of rocks.* McGraw Hill, New York, 1967.

C. Rhee, L. Talbot, and J. A. Sethian. Dynamical study of a premixed v flame. *J. Fluid Mech.*, **300**, 87–115, 1995.

J. W. Rudnicki and J. R. Rice. Conditions for the localization of deformation in pressure-sensitive dilatant materials. *Mech. Phys. Solids*, **23**, 371–394, 1975.

G. Russo and P. Smereka. A level-set method for the evolution of faceted crystals. *SIAM J. Sci. Comp.*, **21**(6), 2073–2095, 2000.

D. W. Schmid and Y. Y. Podladchikov. Fold amplification rates and dominant wavelength selection in multilayer stacks. *Phil. Mag.*, **86**, 3409–3423, 2006.

J. Sethian. A fast marching level set method for monotonically advancing fronts. *Proc. Nat. Acad. Sci.*, **93**, 1591–1595, 1996.

J. A. Sethian. Curvature and the evolution of fronts. *Communication of Mathematical Physics*, **101**(4), 487–499, 1985.

J. A. Sethian. *Level Set Methods and Fast Marching Methods: Evolving interfaces in Computational Geometry, Fluid Mechanics, Computer Vision, and Materials Science.* Cambridge University Press, Cambridge, UK, 2nd edition, 1999.

C. W. Shu and S. Osher. Efficient implementation of essentially nonoscillatory shock capturing schemes. *J. Comp. Phys.*, **77**, 439–471, 1988.

C. W. Shu and S. Osher. Efficient implementation of essentially nonoscillatory shock capturing schemes II. *J. Comp. Phys.*, **83**, 32–78, 1989.

W. Shyy, H. S. Udaykumar, M. M. Rao, and R. W. Smith. *Computational fluid dynamics with moving boundaries.* Taylor & Francis, Philadelphia, 1996.

R. B. Smith. Unified theory of the onset of folding, boudinage, and mullion structure. *Bull. Geol. Soc. Amer.*, **86**, 1601–1609, 1975.

R. B. Smith. Formation of folds, boudinage, and mullions in non-Newtonian materials. *Bull. Geol. Soc. Amer.*, **88**, 312–320, 1977.

M. Smoluchowski. Uber ein gewisse stabilitatsproblem. *Akad. Wiss. Krakau. Math. Kl.*, pages 3–20, 1909.

J. M. T. Thompson and G. W. Hunt. *A general theory of elastic stability.* Wiley, London, 1973.

J. M. T. Thompson and G. W. Hunt. *Elastic Instability Phenomena.* Wiley, London, 1984.

S. P. Timoshenko and J. M. Gere. *Theory of Elastic Stability.* McGraw–Hill, New York, 2nd edition, 1963.

J. Tsitsiklis. Efficient algorithms for globally optimal trajectories. volume **2**, pages 1368–1373. Proceedings of the 33rd Conference on Decision and Control, IEEE, Lake Buena Vista, Florida, 1994.

J. Tsitsiklis. Efficient algorithms for globally optimal trajectories. *IEEE Transactions on Automatic Control*, **40**, 1528–1538, 1995.

C. R. Van Hise. Principles of North American pre-Cambrian geology. *US Geol. Surv.16th Ann. Report*, pages 571–843, 1894.

C. Vita–Finzi. Serial deformation. *Proc. Geol. Assoc.*, **116**, 293–300, 2005.

M. A. Wadee. Experimental evaluation of interactive buckle localization in compression sandwich panels. *J. Sandw. Struct. Mater.*, **1**(3), 230–254, 1999a.

M. A. Wadee, G. W. Hunt, and M. A. Peletier. Kink band instability in layered structures. *J. Mech. Phys. Solids*, **52**(5), 1071–1091, 2004.

M. K. Wadee. The elastic strut on an elastic foundation: A model localized buckling problem. In A. R. Champneys, G. W. Hunt, and J. M. T. Thompson, editors, *Localization and solitary waves in solid mechanics*, volume **12** of *Advanced series in nonlinear dynamics*, pages 31–53. World Scientific, London, 1999b.

C. Wensrich. Slip-stick motion in harmonic oscillator chains subject to Coulomb friction. *Tribology International*, **39**, 490–495, 2005.